UC Berkeley
UC Berkeley Electronic Theses and Dissertations

Title

Multiscale Modeling of Polymers: Fracture Simulations, Constitutive Modeling and Crystallization Analysis

Permalink

https://escholarship.org/uc/item/759142fn

Author

Tamur, Caglar

Publication Date

2024

Peer reviewed|Thesis/dissertation

eScholarship.org Powered by the California Digital Library
University of California

Multiscale Modeling of Polymers: Fracture Simulations, Constitutive Modeling and Crystallization Analysis

By

Caglar Tamur

A dissertation submitted in partial satisfaction of the

requirements for the degree of

Doctor of Philosophy

in

Engineering - Civil and Environmental

in the

Graduate Division

of the

University of California, Berkeley

Committee in charge:

Professor Shaofan Li, Chair
Professor Khalid M. Mosalam
Professor Jon Wilkening

Spring 2024

Multiscale Modeling of Polymers: Fracture Simulations, Constitutive Modeling and Crystallization Analysis

Copyright 2024
by
Caglar Tamur

Abstract

Multiscale Modeling of Polymers: Fracture Simulations, Constitutive Modeling and Crystallization Analysis

by

Caglar Tamur

Doctor of Philosophy in Engineering - Civil and Environmental

University of California, Berkeley

Professor Shaofan Li, Chair

The dissertation investigates the complex behavior of polymers through computational mechanics, employing numerical techniques that include peridynamics (PD), finite element methods (FEM), molecular dynamics (MD), and deep learning. Our aim is to develop a deeper understanding of the relationship between the polymer microstructure and the resultant mechanical properties, in the context of fracture mechanics, large deformation problems, and additive manufacturing.

In the second chapter, we introduce a numerical framework to simulate the fracture response of elastomeric materials. The approach utilizes the bond-based peridynamics formulation, which is a nonlocal and meshfree alternative to the continuum-based methods. We introduced a novel bond potential into the framework, based on the non-Gaussian chain statistics theory, which treats the material as a complex network of randomly jointed chains with extensible links. The resultant formulation is capable of capturing the fracture and large deformation process of elastomeric materials, as demonstrated in several numerical examples and comparisons with the experimental data.

The remaining chapters focus on the semicrystalline polymers that are used in additive manufacturing. In the third chapter, we have developed a constitutive law for crystalline polymers, based on molecular dynamics and machine learning. We have collected data from the MD simulations of Polyamide12 (PA12), which is used to train deep neural networks to capture the mechanical response of the material. We demonstrated that this novel approach can accurately provide a three-dimensional molecular-level anisotropic constitutive relation that can be used in macroscale mechanics methods such as the FEM. The final chapter consists of an analysis of the crystallization of polymers during the additive manufacturing process. By incorporating crystallization and melting models for PA12, we performed a heat transfer analysis using FEM to predict changes in crystallinity during the manufacturing process, which can help achieve the desired mechanical properties in the final product.

To my beloved parents, Handan and Erman Tamur.

Contents

List of Figures

List of Tables

Acknowledgments

I am extremely grateful to my research advisor, Professor Shaofan Li, who always supported and motivated me throughout my graduate studies. Since my first day at Berkeley, I have greatly benefited from his expertise in computational mechanics and research guidance as well as his kindness and wisdom in all aspects of life. Professor Li truly cared for his students and helped us in any way possible. I am fortunate to have the opportunity to work with him and I would like to thank him for the everlasting influence he has on my research.

It was my privilege to study with Professor Khalid M. Mosalam, who taught me the fundamentals of the finite element method. I truly enjoyed his lectures at my first year at Berkeley, which sparked my interest in computational mechanics and motivated me to pursue research in the field.

I would like to extend my sincere thanks to Professor Jon Wilkening, who taught me everything I know about numerical analysis. His lectures on numerical methods for ODEs and PDEs were truly enlightening, which brought mathematical rigor and practical aspects together. Professor Wilkening is one of the kindest and most humble instructors I met at Berkeley and I greatly enjoyed learning from him.

I would like to thank Professors Claudia Ostertag, Paulo Monteiro, Raja Sengupta, and Reza Alam, with whom I worked as a graduate student instructor. Under their mentorship, I gained invaluable experience, and their teaching philosophy continues to guide me.

I was fortunate to be accompanied by great lab mates at Berkeley, including Xuan Hu, Dana Bishara, Qi Zheng, and Chengyao Liang. I especially thank Xuan for the great discussions we had about our research on fracture mechanics and meshfree methods and his willingness to help me all the time.

I extend my deepest gratitude to my partner, Dolunay Öniz, for all her love, support, and encouragement throughout this journey, all of which have been fundamental to my success.

Finally, I wish to acknowledge the Fulbright Scholarship, which provided financial support for my graduate studies, and I would like to thank the Turkish Fulbright Commission.

Chapter 1

Introduction

Polymers, long-chain molecules composed of repeating structural units, are central to a wide range of engineering applications, from automotive components to biomedical devices. In the field of computational mechanics, the study of polymers involves using numerical methods and simulations to predict and analyze their behavior under various conditions. The mechanical properties of polymers are significantly influenced by their microstructure, particularly their molecular structure, interactions between chains, and the degree of crystallinity.

The mechanical response of these materials are inherently complex, involving non-linear elasticity, time-dependent phenomenon, and temperature-dependent behaviors such as plasticity and glass transition. There are computational methods that allow for virtual testing or simulation of polymers under various conditions without the need for extensive physical prototyping. Common techniques include the Finite Element Method (FEM), Molecular Dynamics (MD), and multiscale methods. FEM can help predict deformation and stress distributions at a polymer-based component at the macroscale level, making it an indispensable tool for practical engineering applications. For a more fundamental understanding, MD simulations can provide insight into the atomistic level interactions and dynamics within polymers. MD is particularly useful for exploring how molecular-level changes affect the physical properties of polymers, such as elasticity, strength, and thermal properties. Bridging the gap between molecular structure and macroscopic properties, multiscale modeling involves linking MD and FEA to provide a comprehensive view of polymer behaviors.

A class of polymers which can undergo large deformations under relatively small stresses is known as *elastomers*, which are rubber-like materials. Elastomers can sustain large stretches without undergoing significant permanent deformation, making them suitable materials for use in a wide range of engineering applications, including seismic isolators, vehicle tires, and medical devices. Additive manufacturing (AM) technology, also known as 3D printing, commonly utilizes elastomer-based materials to manufacture customized designs for biomedical devices and wearable electronics [29]. More recently, 3D printed self-healing and shape-memory elastomers have been introduced, which opens even more pathways for customized engineering applications [48]. With these recent advances, it has become increasingly important to accurately model and simulate elastomers.

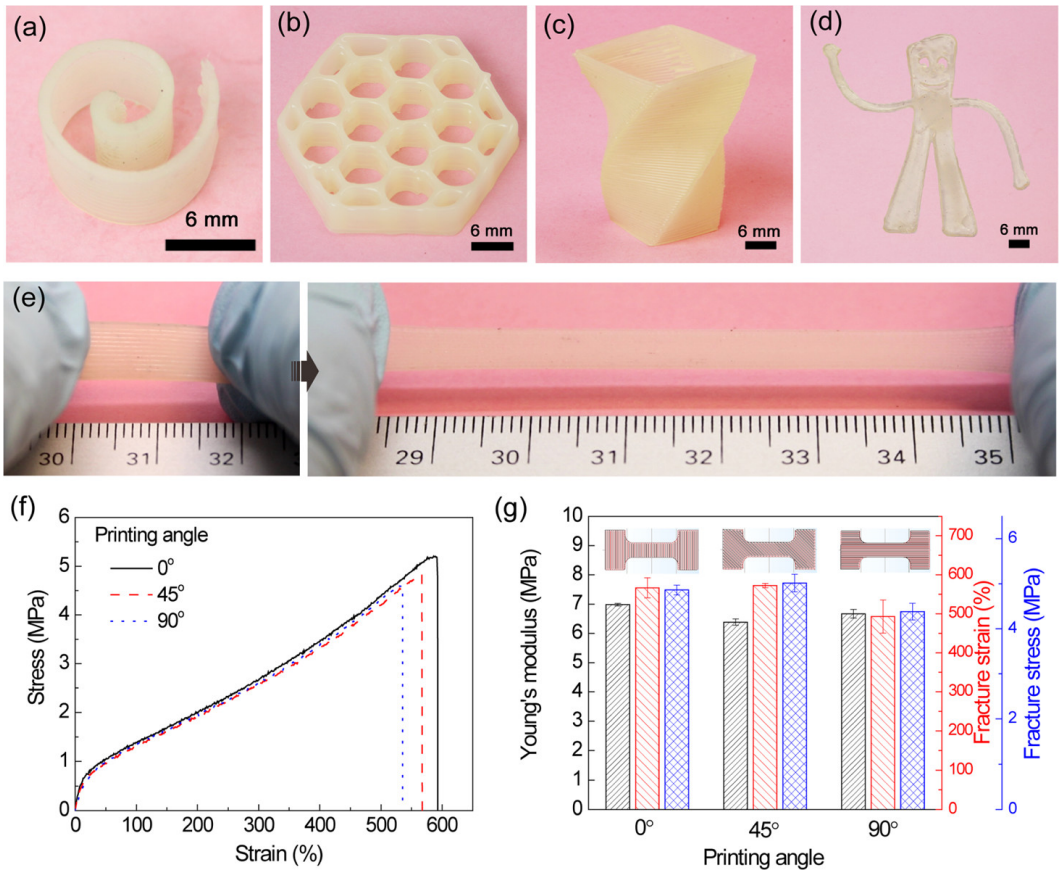

Figure 1.1: Novel 3D printing of a thermoplastic elastomer. (a)-(d) Different architectures. (e) Stretching of the printed geometry in (a) up to 300 % strain. (f) Stress-strain response with different printing angles. (g) Mechanical properties with respect to the printing angle. Reprinted with permission from [48]. Copyright 2018 American Chemical Society.

Elastomers, or "elastic-polymers", consist of long and randomly oriented molecules or chains. These molecules form a microstructure commonly referred to as random chain networks. The chains might be cross-linked, resulting in shape-retaining materials, and there are also thermoplastic variants of elastomers. The elastomer variants have unique mechanical and thermal properties and are chosen according to the application. Traditionally, in continuum mechanics-based approaches, elastomers are modeled as *hyperelastic solids*, which governs the large deformation elastic behavior of the material. These models are derived from a strain energy density functional that quantifies the energy stored in the material due to the deformation, which depends only on the current state of the deformation and not on the path or history of the deformation. In the next section, we present the fundamentals of hyperelastic solids to provide a historical background for our current work on polymers.

1.1 Fundamentals of Hyperelastic Solids

Here we present the fundamentals of hyperelastic solids, starting with the basic kinematic assumptions and briefly discussing the common constitutive relations used for elastomers and polymers. More details about the kinematics and balance laws can be found in any standard text on continuum mechanics, and for a detailed discussion of hyperelastic constitutive models for elastomers readers are referred to the review paper by Dal [20].

We consider an elastic solid $\mathcal{B}$ that occupies the space $\mathbb{R}^3$ with the material coordinates $\boldsymbol{X}$. The deformation map $\varphi : \mathcal{B} \to \mathbb{R}^3$ is defined as

$$\boldsymbol{x} = \varphi(\boldsymbol{X}) \tag{1.1}$$

where $\boldsymbol{x}$ are the spatial coordinates. Corresponding displacement field is defined as

$$\boldsymbol{u} = \boldsymbol{x} - \boldsymbol{X} \tag{1.2}$$

which is required to be continuous since we require the body to be without cracks or other discontinuities.

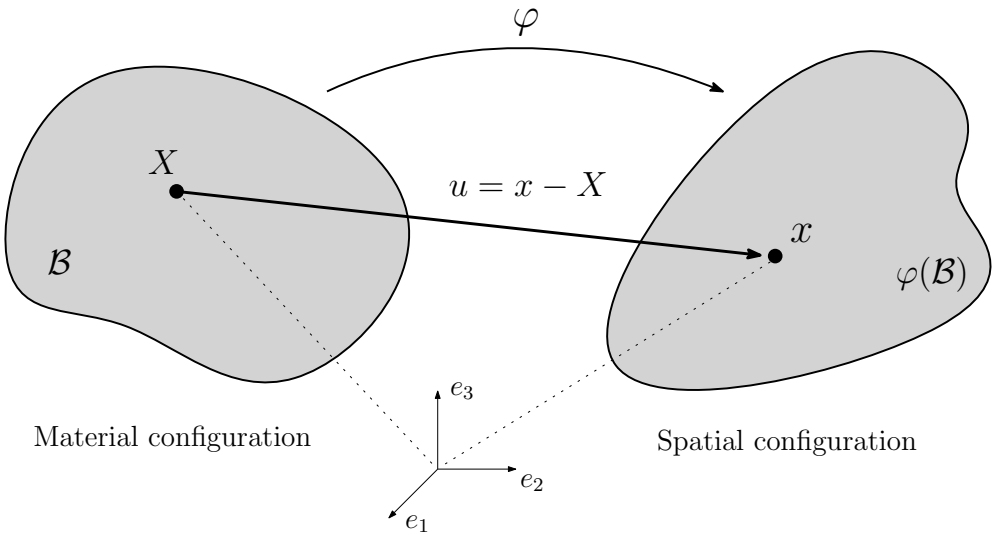

Figure 1.2: Material and spatial configurations

The *deformation gradient* $\boldsymbol{F}$ is defined as the two-point tensor that maps the differential vector $d\boldsymbol{X}$ in the material configuration to the spatial configuration $d\boldsymbol{x}$, and is given by the material derivative of the deformation map:

$$\boldsymbol{F} = \frac{\partial \varphi}{\partial \boldsymbol{X}} \qquad d\boldsymbol{x} = \boldsymbol{F} d\boldsymbol{X} \tag{1.3}$$

Another quantity of interest is known as the *Jacobian* of the deformation, which transforms an infinitesimal volume element in the material configuration to spatial coordinates, and is defined as the determinant of the deformation gradient.

$$J = \det \boldsymbol{F} \qquad dv = JdV \tag{1.4}$$

In large deformation formulations, the constitutive relations are typically expressed using the principal stretches or invariants to preserve the objectivity and frame indifference. For these purposes, *right Cauchy-Green tensor* is defined as

$$\boldsymbol{C} = \boldsymbol{F}^{\mathrm{T}}\boldsymbol{F} \tag{1.5}$$

The eigenvalue decomposition of the right Cauchy-Green tensors gives us the expression

$$\boldsymbol{C} = \sum_{A=1}^{3} \lambda_A^2 \boldsymbol{N}_A \otimes \boldsymbol{N}_A \tag{1.6}$$

where $\lambda_A > 0$ are the principal stretches in the Lagrangian principal directions $\boldsymbol{N}_A$ that defined at the material point $\boldsymbol{X}$.

The principal invariants of the right-Cauchy green tensor are

$$I_1(\boldsymbol{C}) = \mathrm{tr}[\boldsymbol{C}] \tag{1.7}$$

$$I_2(\boldsymbol{C}) = \frac{1}{2}\left(\mathrm{tr}[\boldsymbol{C}]^2 - \mathrm{tr}[\boldsymbol{C}^2]\right) \tag{1.8}$$

$$I_3(\boldsymbol{C}) = \det \boldsymbol{C} \tag{1.9}$$

Using the fact that $\boldsymbol{C}$ is diagonal in principal basis as described in (1.6), we obtain the expressions for the principal invariants as follows.

$$I_1(\boldsymbol{C}) = \lambda_1^2 + \lambda_2^2 + \lambda_3^2 \tag{1.10}$$

$$I_2(\boldsymbol{C}) = \lambda_1^2\lambda_2^2 + \lambda_1^2\lambda_3^2 + \lambda_2^2\lambda_3^2 \tag{1.11}$$

$$I_3(\boldsymbol{C}) = \lambda_1^2\lambda_2^2\lambda_3^2 \tag{1.12}$$

A solid is said to be *hyperelastic* if there is no dissipation in the material. The behavior of the hyperelastic material is described by a strain energy density function $W(\boldsymbol{F})$, which is a function of the deformation gradient only. Alternatively, we can express the strain energy density as a function of the right Cauchy-Green tensor $\bar{W}(\boldsymbol{C})$. Using the zero dissipation argument, we can show that a material is hyperelastic iff the first Piola-Kirchhoff stress tensor $\boldsymbol{P}$ is given by

$$\boldsymbol{P} = \frac{\partial W(\boldsymbol{F})}{\partial \boldsymbol{F}} \tag{1.13}$$

Alternatively, using standard relations, we can show that the second Piola-Kirchhoff stress $\boldsymbol{S}$ of a hyperelastic solid is

$$\boldsymbol{S} = 2\frac{\partial \bar{W}(\boldsymbol{C})}{\partial \boldsymbol{C}} \tag{1.14}$$

For an isotropic hyperelastic material in finite deformation, the strain energy density can be expressed as a function of the principal stretches or the principal invariants.

$$W = \hat{W}(\lambda_1, \lambda_2, \lambda_3) \qquad \text{or} \qquad W = \tilde{W}(I_1, I_2, I_3) \tag{1.15}$$

Considering the invariant formulations, we see that $\boldsymbol{S}$ reads as

$$\boldsymbol{S} = 2\left[\frac{\partial W}{\partial I_1}\frac{\partial I_1}{\partial \boldsymbol{C}} + \frac{\partial W}{\partial I_2}\frac{\partial I_2}{\partial \boldsymbol{C}} + \frac{\partial W}{\partial I_3}\frac{\partial I_3}{\partial \boldsymbol{C}}\right] \tag{1.16}$$

Using derivatives of the invariants, we can show that the second Piola-Kirchhoff stress for isotropic hyperelastic solids becomes

$$\boldsymbol{S} = 2\left(\frac{\partial W}{\partial I_1} + I_1\frac{\partial W}{\partial I_2}\right) - 2\frac{\partial W}{\partial I_2}\boldsymbol{C} - p\boldsymbol{C}^{-1} \tag{1.17}$$

where $p = -J\ \partial W/\partial J$ is referred as the pressure term.

Elastomers or rubber-like materials are typically incompressible, that is, their volume does not change when deformed. Recalling the definition of the Jacobian in (1.4), we can see that $J = 1$ for incompressible materials and the third invariant of the right Cauchy-Green tensor becomes unity, $I_3 = 1$. Therefore, the strain energy density of an elastomer is commonly expressed as $W = W(I_1, I_2)$

The strain energy density of elastomers can take different forms, and historically, many successful attempts have been made to describe their constitutive behaviors. We can view these different constitutive laws in two main categories; phenomenological models and micromechanics driven models. Phenomenological models can be further classified into principal stretch-based, principal invariant-based, and hybrid models [20]. Micromechanical models are typically derived using the non-Gaussian statistical mechanics formulations of Kuhn-Grün [49] to describe the behavior of randomly jointed single chains, commonly referred to as chain network models. The following are some famous examples of strain energy densities used to model elastomers.

Neo-Hookean model [77]:

$$W(I_1) = \frac{\mu}{2}(I_1 - 3) \tag{1.18}$$

where μ is the shear modulus of the material. Based on Treolar's work on polymer networks [94] and proposed by Rivlin, the neo-Hookean is an invariant based, one parameter model which is typically accurate in the small strain regimen. It is the simplest of hyperelasticity

and can be thought as a special case of other elastomer models. Compressible version of the neo-Hookean model can be expressed as,

$$W(I_1, J) = \frac{1}{2}\mu[I_1 - 3] - \mu \ln J + U(J) \tag{1.19}$$

where $U(J)$ defines the volumetric response of the material. There are many variations for the volumetric term in the literature, for example $U(J) = \frac{\lambda}{2}(J-1)^2$ or $U(J) = \frac{\lambda}{2}(\ln J)^2$, where λ is the Lamé modulus.

Mooney-Rivlin model [66, 77]:

$$W(I_1, I_2) = C_1(I_1 - 3) + C_2(I_2 - 3) \tag{1.20}$$

where C_1 and C_2 are two empirical material constants that can be determined by experiments. Proposed by Mooney and later simplified by Rivlin, the Mooney-Rivlin is a two parameter invariant based formulation. It has compressible variations, for instance

$$W(I_1, I_2, J) = C_1(I_1 - 3) + C_2(I_2 - 3) - C_1 \ln J + U(J) \tag{1.21}$$

where $U(J)$ is the volumetric term of choice.

Gent model [22]:

$$W(I_1) = -\frac{\mu}{2} J_m \ln\left(1 - \frac{I_1 - 3}{J_m}\right) \tag{1.22}$$

where J_m is a material parameter defining the limiting value of the chain stretch. The I_1 is constrained in the range $3 \leq I_1 < J_m + 3$. Alan Gent proposed this two parameter invariant-based model to represent the large deformation phenomena, up to the chain extensibility limit. It reduces to the neo-Hookean model as $J_m \to \infty$. Possible compressible versions can be found in [33], one example being:

$$W(I_1, I_2, I_3) = -\frac{\mu}{2} J_m \ln\left(1 - \frac{I_1 - 3}{J_m}\right) - \mu \ln J \tag{1.23}$$

Ogden model [74]:

$$W(\lambda_1, \lambda_2, \lambda_3) = \sum_{i=1}^{N} \frac{2\mu_i}{\alpha_i} \left(\lambda_1^{\alpha_i} + \lambda_2^{\alpha_i} + \lambda_3^{\alpha_i} - 3\right) \tag{1.24}$$

where N, μ_i and α_i are material constants. A typical choice would be $N = 3$, which leads to 6 independent empirical material parameters. Contrary to the previously discussed models, Ogden model is a principal stretch-based approach which is suitable for isotropic and incompressible rubber-like materials.

Three-chain model [100]:

$$W(\lambda_1,\lambda_2,\lambda_3) = \frac{Nk\theta}{3}\sqrt{n}\Bigg[\lambda_1\beta_1 + \sqrt{n}\ln\left(\frac{\beta_1}{\sinh\beta_1}\right) + \lambda_2\beta_2 + \sqrt{n}\ln\left(\frac{\beta_2}{\sinh\beta_2}\right) + \lambda_3\beta_3 + \sqrt{n}\ln\left(\frac{\beta_3}{\sinh\beta_3}\right)\Bigg] \tag{1.25}$$

where

$$\beta_i = \mathcal{L}^{-1}\left(\frac{\lambda_i}{\sqrt{n}}\right) \qquad \text{and} \qquad \mathcal{L}(\beta) = \coth\beta - \frac{1}{\beta} \tag{1.26}$$

The three-chain model is a micromechanics-inspired model, where the elastomer is treated as a network of random chains with rigid links. The unit cell has three chains aligned in the principal directions, and the chains deform affinely. It is based on non-Gaussian chain statistics [49, 95], also called Langevin statistics. N is the chain density, k is the Boltzmann's constant, θ is the absolute temperature, and n is the number of links per chain.

Arruda-Boyce eight-chain model [3]:

$$W(\lambda_1,\lambda_2,\lambda_3) = Nk\theta\sqrt{n}\left[\beta_{chain}\lambda_{chain} + \sqrt{n}\ln\left(\frac{\beta_{chain}}{\sinh\beta_{chan}}\right)\right] \tag{1.27}$$

where λ_{chain} is the stretch of each chain, given as

$$\lambda_{chain} = \sqrt{\frac{\lambda_1^2+\lambda_2^2+\lambda_3^2}{3}} = \sqrt{\frac{I_1}{3}} \tag{1.28}$$

An improvement to the three-chain model, the Arruda-Boyce model considers a cubic unit cell with eight chains. The chains are connected to the edges and linked at the centroid of the cube. The cube obeys an affine transformation in which the edges remain aligned with the principal directions during the deformation and the resulting incompressibility condition can be expressed as $\lambda_1\lambda_2\lambda_3 = 3$. From (1.28), we can see that the strain energy density is only a function of the first invariant, i.e. $W(\lambda_1,\lambda_2,\lambda_3) = W(I_1)$. The parameters in the model are the same as explained for the three-chain model, utilizing Langevin statistics. The reader is referred to the review paper by Arruda and Boyce [13] for more details and comparisons about chain network-based hyperelastic models.

1.2 Dissertation Overview

Fracture Simulations of Elastomers

In Chapter 2, we present the development of a bond-based peridynamics model to study the fracture of polymer networks under finite deformation. Our approach is based on the Kuhn-Grün model of randomly jointed polymers with extensible chains, which allows polymer rupture through the chain scission mechanism. We introduced a novel mesoscale bond potential that intrinsically incorporates the Arruda-Boyce model into a non-local continuum framework with the purpose of modeling the mechanical response of general elastomeric materials and their fracture process. The proposed material model involves macroscale parameters that can be linked to the continuum level hyperelastic models, as well as microscale constants that can be determined from the first principals.

We have demonstrated through a series of numerical examples, both two-dimensional and three-dimensional, that the proposed model is robust and efficient in modeling crack growth in polymeric materials. The model is carefully validated with experimental data and numerical results obtained on the basis of existing continuum mechanics polymer models. We have shown that the proposed peridynamic model is accurate and stable in various configurations and loading modes, such as Mode-I and Mode-II crack opening. Compared with existing continuum models and fracture modeling methods, our present technique has the advantages of being theoretically simple, rigorous, and computationally fast. The numerical results show that the nonlocal model can easily capture the fracture process in elastomeric materials without complex ad hoc modeling parameters under finite deformation and has the potential to become a convenient simulation tool for modeling the polymer failure process in the design and optimization of polymeric materials. This chapter is based on the author's previous publication [90].

Constitutive Modeling and Crystallinity Prediction for Additive Manufacturing

The remaining chapters focus on semicrystalline polymers that are commonly used in additive manufacturing. Predicting material properties of 3D printed polymer products is a challenge due to the highly localized and complex manufacturing process. The microstructure of such products is fundamentally different from that obtained by using conventional manufacturing methods. Traditional modeling approaches often fail to accurately predict the mechanical behavior of polymers due to their complex microsturcture, especially near failure points. Higher accuracy might be achieved considering multiscale MD and FEM simulations. Concurrent MD simulations at each FEM timestep is not computationally feasible considering the time cost of complex polymer MD simulations.

To bridge the gap between atomistic and macro length scales, in Chapter 3, we have developed a machine learning and MD-based approach to model the constitutive laws of crystalline polymers. We built deep neural networks to predict the mechanical response of

the crystalline form of Polyamide12 (PA12) based on data collected from molecular dynamics simulations. The main goal here is to develop an atomistically informed constitutive relation which can be supplied to multiscale FEM simulations to replace traditional hyperelastic constitutive laws. Using the ML approach, we can predict the stress-strain relations of PA12 once the macroscale deformation gradient is provided as input to the neural networks. We have shown that this is an efficient and accurate approach, which can provide a three-dimensional molecular-level anisotropic stress-strain relation of PA12 for any macroscale mechanics model, such as finite element modeling at arbitrary quadrature points. This chapter is based on the author's previous publication [91].

In Chapter 4, we present an FEM simulation approach in predicting the crystallinity evolution of semicrystalline polymers used in additive manufacturing. The degree of crystallinity strongly affects the mechanical properties of polymers, such as ductility, ultimate strength, and thermal properties. Thus, it is crucial to understand how the process parameters affect the crystallization. We integrated the Nakamura and Hoffman-Lauritzen theories to model the nonisothermal crystallization kinetics of PA12. During the additive manufacturing process, the melt material might affect the crystallinity of the previous layers, so a statistical melting model is introduced. The crystallization-melting models were then incorporated into an uncoupled transient heat analysis, to simulate the additive manufacturing process. This is done by utilizing the user-defined UMATHT subroutine in the FEM software Abaqus, which allows one to define the thermal constitutive relation of the material. Our work allows for a precise prediction of the changes in crystallinity during the printing process, which is crucial for achieving desired mechanical properties in the final product.

Chapter 2

Nonlocal Fracture Simulations of Elastomeric Materials

2.1 Introduction

Polymeric materials, due to their versatile properties and relatively low cost, have found many applications in almost every part of our daily life, from plastics used as packaging materials to various polymers in industrial applications, such as materials used in airplanes, bridges, automobiles, ships, sports equipment, 3D printed products, polymeric concrete, polymer solar cells, bottles, and containers in pharmaceutical industries, among other objects [81, 15]. From the perspectives of science, technology, and engineering, polymers are studied in many fields such as soft matter, biomaterials, polymer chemistry, polymer physics, engineering, and so on. However, modeling the mechanical properties of polymeric materials has been a great challenge, especially how to correctly simulate their failure mechanism and failure process. This is because the failure of polymeric materials is a special physical process of condensed solid-state materials, which involves breaking of the polymer chains and rearrangements of complex chain networks inside the polymeric materials. Thus, this process is not only under large or finite deformations but is also intrinsically nonlocal, because the crossover length scale of the coiled polymer chains ranges from 10 nm to 10 μm.

Statistical mechanics treatment of rubber elasticity is a classical topic in polymer science, and there have been many attempts to describe the constitutive laws (see [12]). Historically, statistical theory started with Gaussian models and later extended to finite deformation by introducing non-Gaussian techniques. Among these theories, perhaps the most well known to the applied mechanics community is the Arruda-Boyce model [3], which was built on the work of Kuhn and Grün [49], who derived the configurational entropy of an extended single rubber chain via Langevin statistics. More recently, Anand and his group extended the basic Kuhn-Grün model by adding a bond potential term that accounts for the stretching of the atomic bonds in the polymer chains, aka the Kuhn segments. By allowing these Kuhn segments to rupture, they modeled the fracture response of the elastomeric material

via the phase-field model [59, 60, 71]. In particular, by recognizing the nonlocal nature of polymer fracture mechanics, Narayan and Anand proposed a strain-gradient damage theory to describe the deformation and failure of amorphous polymers [71], which is only a part of the general polymeric materials.

Peridynamics is a nonlocal theory of mechanics that is developed as an alternative to classical continuum mechanics [84, 86, 27]. The material is represented as a collection of discrete particles that interact with each other within a finite distance. These interactions are described by nonlocal integral equations, which ultimately constitute the governing equations of the theory. Peridynamics has been applied to a wide range of problems and has proved to be useful especially in modeling discontinuous material behavior, such as crack propagation and other types of material failure. There are two types of peridynamic methods: bond-based peridynamics [84, 27] and state-based peridynamics [86, 8]. State-based peridynamics is essentially a meshfree method that uses the correspondence principle to establish material constitutive relations, whereas the bond-based peridynamics is a nonlocal continuum mechanics model that utilizes mesoscale bond deformation kinematics and force state to establish a nonlocal continuum or fracture mechanics model [85, 26, 106].

Attempts of peridynamics modeling of polymers have so far been limited to state-based peridynamics modeling. Madenci's group, e.g. [7, 78], developed peridynamics correspondence models, which utilize existing continuum hyperelastic consititutive relations in the peridynamics framework to model polymeric materials. Specifically, they used neo-hookean material model in the state-based peridynamics to study finite deformation elastic response and rupture of polymers [7]. In another study, they adopted the Kuhn-Grün based phase field method of Anand's group [61, 89] into the state-based peridynamic framework [78]. Utilizing the advantages of peridynamics, the aforementioned methods are quite powerful but they are essentially meshfree modeling of nonlinear continuum materials, and they are not examining the mesoscale microstructure of polymerical materials, which is a key technical ingredient of peridynamics. Therefore, these studies are not fundamentally different from phase field fracture models.

To the best of our knowledge, to date, no bond-based peridynamics or nonlocal polymeric material model has been reported in the literature. One of the objectives of this study is to develop a digital version of the Arruda-Boyce model or a nonlocal polymer continuum mechanics model that can directly simulate the fracture and failure of polymeric materials without invoking other numerical treatments, such as the introduction of a phase field.

In this work, utilizing the ability of peridynamics to model nonlocal deformation and failure, as well as its ability to simulate fracture, we developed a bond-based peridynamics model for elastomeric materials. The organization of the chapter is as follows. We start by a brief introduction of bond-based peridynamics where we outline the nonlocal kinematics and balance laws, and present a formulation for nonlocal stress. Next, we introduce a mesocale potential and its related peridynamic constitutive relations for elastomer chain networks. To validate the proposed material model, we present a series of numerical simulations in both two-dimensional and three-dimensional spaces.

2.2 Fundamentals of Bond-Based Peridynamics

Peridynamics (PD) is a theoretical and computational framework for modeling the mechanical behavior of materials. The theory was proposed by Silling [84] as an alternative to classical continuum mechanics. Materials are modeled as a collection of discrete particles, which interact over a finite distance, resulting in the nonlocality of the theory. The interactions are described using nonlocal integral equations, which give rise to the governing equations of PD. Unlike the classical continuum-based approaches, such as the Finite Element Method (FEM), PD does not require the strong continuity of the displacement field, hence allowing a direct simulation framework for materials and structures with discontinuities. The method proved especially useful in modeling problems in fracture mechanics, such as brittle and ductile crack growth and failures. Peridynamics has two types of formulations, state-based and bond-based PD.

The bond-based PD is the original formulation by Silling, which models the interactions between particles as elastic springs or bonds. The bonds can withstand deformation up to a prescribed limit, and they fail beyond that, resulting in the failure of the material. The original theory considers a simple constitutive law called the Prototype Microelastic Brittle (PMB) model [84], but has recently been extended to include more complex material behavior by the introduction of the cohesive peridynamics framework [27]. Main drawback of the bond-based approach is that it is only able to model materials with constant Poisson's ratios, $\nu = 1/3$ in 2D plane stress formulation and $\nu = 1/4$ for 3D or plane stress conditions.

The state-based PD is introduced to describe more general constitutive modeling [86]. Introducing the concepts of deformation states and force states, this allowed the modeling of materials with general Poisson's rations and the connection to classical continuum constitutive relations. The key difference between the bond-based approach is that, in the state-based PD, the bond force between two particles depends on the deformation of a collection of particles within their vicinity, whereas in the bond-based PD the bond force is only the function of the relative deformation of the particles. The state-based PD is essentially a meshfree approach that defines material behaviors through the correspondence principle, while bond-based PD employs mesoscale bond deformation to create a model for nonlocal continuum and fracture mechanics. The following section briefly describes the fundamentals of bond-based PD in relation to the current work.

Kinematics and Balance Laws

In bond-based peridynamics, the material is represented as a set of discrete particles, known as *material points*. For a given pair of points in the reference configuration $\mathcal{B}$, we denote their coordinates by $\boldsymbol{X}$ and $\boldsymbol{X'}$. We define the vector that connects them as the *reference bond*, denoted as $\boldsymbol{\xi} = \boldsymbol{X'} - \boldsymbol{X}$, shown in Fig.2.1. The interactions between the particles are considered to occur in a finite region, called the *peridynamics horizon*. The horizon is typically chosen as a disk in 2D or a sphere in 3D, with the horizon radius δ, depicted in Fig.2.1.

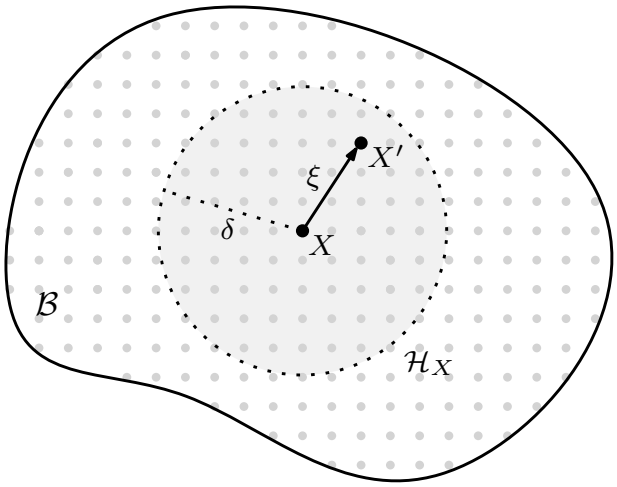

Figure 2.1: Material points and the peridynamic horizon

As the material deforms, the material points $\boldsymbol{X}$ and $\boldsymbol{X'}$ move to the new positions $\boldsymbol{x}$ and $\boldsymbol{x'}$, respectively. The movement from their reference positions is captured by the displacement vectors,

$$\boldsymbol{u} = \boldsymbol{x} - \boldsymbol{X} \tag{2.1}$$

$$\boldsymbol{u'} = \boldsymbol{x'} - \boldsymbol{X'} \tag{2.2}$$

The *bond deformation* $\boldsymbol{\eta}$, which reflects the change in position of material points relative to each other, and the *deformed bond vector* $\boldsymbol{\zeta}$ showing the altered spatial relationship between the points after deformation defined respectively as

$$\boldsymbol{\eta} = \boldsymbol{u'} - \boldsymbol{u} \tag{2.3}$$

$$\boldsymbol{\zeta} = \boldsymbol{\xi} + \boldsymbol{\eta} \tag{2.4}$$

The kinematics of bond-based PD in the reference body $\mathcal{B}$ and the deformed body $\mathcal{B}_t$ is depicted in Fig.2.2. As a point of departure from the classical continuum theory, the displacement map does not need to be continuous or differentiable. Moreover, there is no need for a concept of strain in the nonlocal theory. On the other hand, it is useful to define the concept of *bond stretch* λ, which would be useful in defining the constitutive relations as follows.

$$\lambda = \frac{|\boldsymbol{\xi} + \boldsymbol{\eta}|}{|\boldsymbol{\xi}|} \tag{2.5}$$

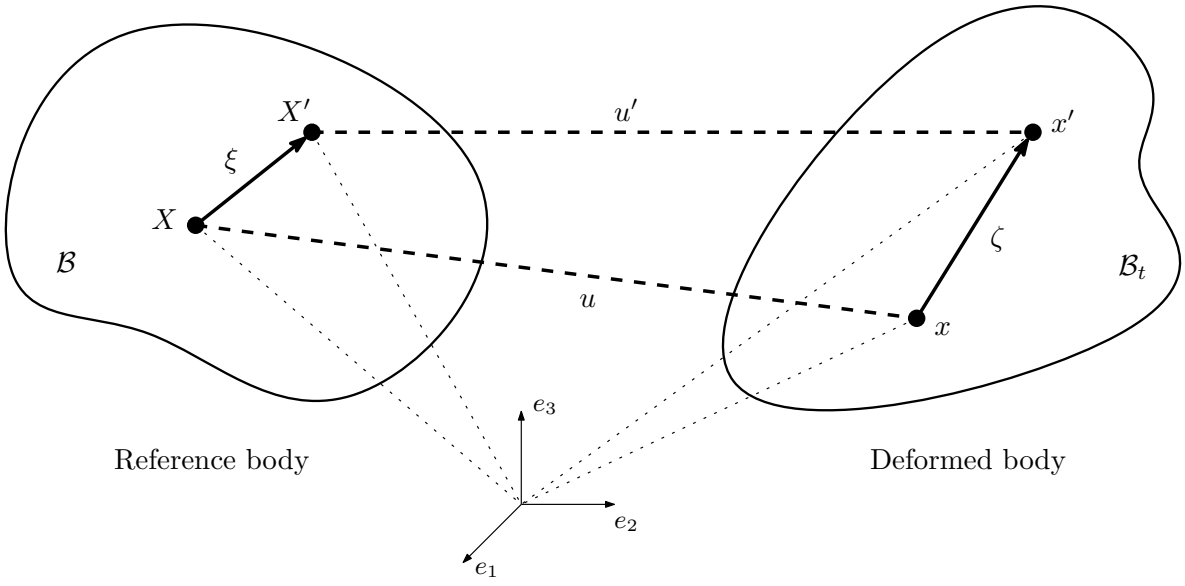

Figure 2.2: Kinematic relations of the bond-based PD

Now, let us define the governing equations of the bond-based peridynamics. The nonlocal balance of linear momentum [85] gives us the following equation of motion.

$$\rho(\boldsymbol{X})\ddot{\boldsymbol{u}}(\boldsymbol{X}) = \int_{\mathcal{B}} \boldsymbol{f}(\boldsymbol{X}, \boldsymbol{X'}) dV_{X'} + \boldsymbol{b}(\boldsymbol{X}) \qquad \forall \boldsymbol{X} \in \mathcal{B} \tag{2.6}$$

In this context, $\rho(\boldsymbol{X})$ represents the mass density at a point $\boldsymbol{X}$, $\ddot{\boldsymbol{u}}(\boldsymbol{X})$ denotes the acceleration, and $\boldsymbol{b}(\boldsymbol{X})$ is the bond force per unit volume acting on the material body. The term $\boldsymbol{f}(\boldsymbol{X}, \boldsymbol{X'})$ inside the integral is referred to as the *dual force density*, which quantifies the force interactions per unit volume squared between the material points $\boldsymbol{X}$ and $\boldsymbol{X'}$. Another important concept introduced is the bond force density, $\boldsymbol{t}(\boldsymbol{X}, \boldsymbol{X'})$, that is equal to the half of the dual force density, $\boldsymbol{t}(\boldsymbol{X}, \boldsymbol{X'}) = \frac{1}{2}\boldsymbol{f}(\boldsymbol{X}, \boldsymbol{X'})$.

The bond force density incorporates the constitutive model. In bond-based PD, it is only dependent on the bond deformation and the initial bond vectors $\boldsymbol{\eta}$ and $\boldsymbol{\xi}$, in addition to the material constants. Therefore, we can express it as $\boldsymbol{t}(\boldsymbol{\eta}, \boldsymbol{\xi})$.

A key assumption in bond-based PD is that particle interactions exist only in a finite domain, called the peridynamic horizon, denoted as $\mathcal{H}$. With the choice of a circular or spherical horizon, we indicate the distance where the interactions diminish as the horizon radius δ. The horizon centered on a material point $\boldsymbol{X}$ in the reference configuration and the corresponding radius are depicted in Fig.2.1, which also displays an initial bond vector $\boldsymbol{\xi}$ between the material points $\boldsymbol{X}$ and $\boldsymbol{X'}$.

In the original formulation of the bond-based PD, pairwise reactions are constrained to be equal in magnitude and opposite in direction, and they have to lie in the direction of the deformed bond vector. The conditions that the bond force density has to satisfy are summarized in the following equations.

$$\boldsymbol{t}(\boldsymbol{\eta}, \boldsymbol{\xi}) = \mathbf{0}, \quad \forall |\boldsymbol{\xi}| > \delta \tag{2.7}$$

$$\boldsymbol{t}(-\boldsymbol{\eta}, -\boldsymbol{\xi}) = -\boldsymbol{t}(\boldsymbol{\eta}, \boldsymbol{\xi}) \tag{2.8}$$

$$\int_{\mathcal{B}} (\boldsymbol{\xi} + \boldsymbol{\eta}) \times \boldsymbol{t}(\boldsymbol{\eta}, \boldsymbol{\xi}) dV_X = 0 \tag{2.9}$$

Equation (2.7) indicates the diminishing force density beyond the horizon radius and (2.8) is necessary to ensure the action-reaction principle or the anti-symmetry of the force density. Finally, (2.9) is required to guarantee the conservation of the angular momentum [84]. There are other variations of PD, which might introduce rotations of particles or moment couples, that lead to different formulations, but they are not relevant for the purposes of this work.

Peridynamic Stress

The notion of strain and a corresponding stress is not a necessary concept in bond-based peridynamics. They do not appear in the governing equations or in the numerical implementation of the method, as opposed to continuum-based methods such as the FEM. Nevertheless, computing the stress would be useful for comparisons with experimental work or to make connections with existing classical continuum models.

Originally, the peridynamic stress tensor proposed by Lechouq [52], is shown in (2.10). $\boldsymbol{f}(\boldsymbol{X}, \boldsymbol{X'})$ is the dual force density and $d\Omega_{\boldsymbol{M}}$ is the solid angle of the unit sphere S^2 in the direction of the unit vector $\boldsymbol{M}$.

$$\boldsymbol{P}_{LS}(\boldsymbol{X}) = \frac{1}{2} \int_{S^2} \int_0^\infty \int_0^\infty (y+z)^2 \boldsymbol{f}(\boldsymbol{X} + y\boldsymbol{M}, \boldsymbol{X} - z\boldsymbol{M}) \otimes \boldsymbol{M} \, dz \, dy \, d\Omega_{\boldsymbol{M}} \tag{2.10}$$

With this definition, the divergence of the peridynamic stress tensor is equal to the integral of the force density over the horizon, (2.11), given that it is continuosly differentiable over the domain [52].

$$\nabla \cdot \boldsymbol{P}_{LS}(\boldsymbol{X}) = \int_{\mathcal{H}_{\boldsymbol{X}}} \boldsymbol{f}(\boldsymbol{X}, \boldsymbol{X'}) dV_{\boldsymbol{X'}} \tag{2.11}$$

Expressed in terms of the PD stress, the equation of motion reduces to that of the continuum theory, (2.12).

$$\rho(\boldsymbol{X}) \ddot{\boldsymbol{u}}(\boldsymbol{X}) = \nabla \cdot \boldsymbol{P}_{LS}(\boldsymbol{X}) + \boldsymbol{b}(\boldsymbol{X}) \tag{2.12}$$

The field $\boldsymbol{P}_{LS}(\boldsymbol{X})$ can be thought of as a nonlocal first Piola-Kirchhoff (PK1) stress and proved to be equivalent to the static Piola-Kirchhoff Virial stress in a recent study [55].

Although the PD stress proposed in (2.10) is accurate, it does not provide an efficient and straightforward way of numerical implementation. Recently Li provided a simpler and computationally efficient formula [55] which proved useful in numerical simulations, (2.13).

$$\boldsymbol{P}(\boldsymbol{X}) = \frac{1}{2\Omega_{\boldsymbol{X}}} \sum_{I=1}^{N_X} \sum_{J=1, J\neq I}^{N_X} \boldsymbol{t}_{IJ} \otimes (\boldsymbol{X}_J - \boldsymbol{X}_I), \qquad \forall \boldsymbol{X}_I, \boldsymbol{X}_J \in \mathcal{H}_{\boldsymbol{X}} \ . \tag{2.13}$$

where $\boldsymbol{t}_{IJ} = \boldsymbol{t}(\boldsymbol{X}_I, \boldsymbol{X}_J) V_I V_J$ is the bond force and $(\boldsymbol{X}_J - \boldsymbol{X}_I) = \boldsymbol{\xi}_{IJ}$ is the reference bond vector for the material points $\boldsymbol{X}_I$ and $\boldsymbol{X}_J$.

Here we present this new approach to computing the bond-based peridynamic stress and provide a rigorous proof. The presentation is analogous to the stress theory originally developed for molecular dynamics, known as the Noll-Hardy-Murdoch formalism [72, 28, 67, 68] and more recently iterated by other authors [110, 103].

Theorem 1. *Peridynamic PK1 stress has the analytical representation*

$$\boldsymbol{P}(\boldsymbol{X}) = \frac{1}{2} \sum_{I=1}^{N_X} \sum_{J=1, J\neq I}^{N_X} \boldsymbol{t}_{IJ} \otimes (\boldsymbol{X}_J - \boldsymbol{X}_I) B_{IJ}(\boldsymbol{X}) \ , \tag{2.14}$$

where $\boldsymbol{t}_{IJ}$ is the force exerted to by the particle $\boldsymbol{X}_I$ to $\boldsymbol{X}_J$, N_X is the number of particles inside the horizon $\mathcal{H}_{\boldsymbol{X}}$ and

$$B_{IJ}(\boldsymbol{X}) = \int_0^1 \varphi((1-\alpha)\boldsymbol{X}_I + \alpha \boldsymbol{X}_J - \boldsymbol{X}) \, d\alpha \tag{2.15}$$

is the bond function, as defined by Noll [72] and Hardy [28] for deriving the stress tensor for molecular dynamics simulations.It averages the nonlocal window function over the bond length between the material points $\boldsymbol{X}_I$ and $\boldsymbol{X}_J$. Here, $0 \leq \alpha \leq 1$ is a scalar variable and $\varphi(\boldsymbol{X'} - \boldsymbol{X})$ is a window function that is smooth, positive, symmetric, and satisfies the following requirements.

$$\operatorname*{argmax}_{\boldsymbol{X}} \varphi(\boldsymbol{X'} - \boldsymbol{X}) = \boldsymbol{X'} \ , \tag{2.16}$$

$$\lim_{(X'-X)\to\infty} \varphi(\boldsymbol{X'} - \boldsymbol{X}) = 0 \ , \quad \textit{and} \tag{2.17}$$

$$\int_{R^3} \varphi(\boldsymbol{X'} - \boldsymbol{X}) \, d\boldsymbol{X} = 1 \ . \tag{2.18}$$

In bond-based peridynamics, typical choices for the window function φ are the Gaussian function or the cubic spline function. Note that φ does not need to be compactly supported and the integration is over the whole three-dimensional space.

Proof. Consider a Dirac comb for the continuous force density distribution around the material point $\boldsymbol{X}$.

$$\boldsymbol{\mathcal{F}}(\boldsymbol{X},\boldsymbol{X'}) = \sum_{I=1}^{N_X}\sum_{J=1,J\neq I}^{N_X} \boldsymbol{t}_{IJ}\delta(\boldsymbol{X}_I-\boldsymbol{X})\delta(\boldsymbol{X}_J-\boldsymbol{X'}) \ , \qquad \forall \boldsymbol{X}_I,\boldsymbol{X}_J \in \mathcal{H}_{\boldsymbol{X}} \ , \tag{2.19}$$

where N_X is the number of particles inside the horizon $\mathcal{H}_{\boldsymbol{X}}$ and $\delta(\boldsymbol{X})$ is the Dirac delta function.

Lehoucq and Silling [52] utilized Noll's lemmas to construct the peridynamic stress tensor mentioned in (2.10). The force density $\boldsymbol{\mathcal{F}}(\boldsymbol{X},\boldsymbol{X'})$ is continuously differentiable and anti-symmetric, therefore we have the following expression for the peridynamic PK1 stress based on Noll's lemmas [72, 51];

$$\boldsymbol{P}(\boldsymbol{X}) = -\frac{1}{2}\int_{\boldsymbol{V}_R}\int_0^1 \boldsymbol{\mathcal{F}}(\boldsymbol{X}+\alpha\boldsymbol{R},\boldsymbol{X}-(1-\alpha)\boldsymbol{R})\otimes\boldsymbol{R}\,d\alpha\,dV_{\boldsymbol{R}} \tag{2.20}$$

where $\boldsymbol{X}$ is the position of a material point where the stress is being evaluated, $\boldsymbol{R}$ is the integration variable over the space $V_{\boldsymbol{R}}$ with the infinitesimal volume element $dV_{\boldsymbol{R}}$ and α is a scalar variable with $0 \leq \alpha \leq 1$.
We then introduce a window function $\varphi(\boldsymbol{Y}-\boldsymbol{X})$ to smooth the stress field,

$$\boldsymbol{P}(\boldsymbol{X}) = \int_{V_{\boldsymbol{Y}}} \varphi(\boldsymbol{Y}-\boldsymbol{X})\boldsymbol{P}(\boldsymbol{Y})\,d\boldsymbol{Y} \ . \tag{2.21}$$

Substituting PK1 stress expression of (2.20) for $\boldsymbol{P}(\boldsymbol{Y})$ into (2.21) , we obtain

$$\boldsymbol{P}(\boldsymbol{X}) = -\frac{1}{2}\int_{V_{\boldsymbol{Y}}}\int_{V_{\boldsymbol{R}}}\int_0^1 \varphi(\boldsymbol{Y}-\boldsymbol{X})\boldsymbol{\mathcal{F}}(\boldsymbol{Y}+\alpha\boldsymbol{R},\boldsymbol{Y}-(1-\alpha)\boldsymbol{R})\otimes\boldsymbol{R}\,d\alpha\,dV_{\boldsymbol{R}}\,dV_{\boldsymbol{Y}} \ . \tag{2.22}$$

Considering the change of variables $(\boldsymbol{R},\boldsymbol{Y}) \rightarrow (\boldsymbol{u},\boldsymbol{v})$,

$$\boldsymbol{u} = \boldsymbol{Y}+\alpha\boldsymbol{R} \qquad \rightarrow \qquad \boldsymbol{R} = \boldsymbol{u}-\boldsymbol{v} \ , \tag{2.23}$$

$$\boldsymbol{v} = \boldsymbol{Y}-(1-\alpha)\boldsymbol{R} \qquad \rightarrow \qquad \boldsymbol{Y} = (1-\alpha)\boldsymbol{u}+\alpha\boldsymbol{v} \ , \tag{2.24}$$

where the Jacobian of the transformation is

$$\det(\mathrm{J}(\boldsymbol{u},\boldsymbol{v})) = \begin{vmatrix} \dfrac{\partial\boldsymbol{R}}{\partial\boldsymbol{u}} & \dfrac{\partial\boldsymbol{R}}{\partial\boldsymbol{v}} \\ \dfrac{\partial\boldsymbol{Y}}{\partial\boldsymbol{u}} & \dfrac{\partial\boldsymbol{Y}}{\partial\boldsymbol{v}} \end{vmatrix} = \begin{vmatrix} 1 & -1 \\ (1-\alpha) & \alpha \end{vmatrix} = 1 \ . \tag{2.25}$$

Therefore, (2.22) becomes

$$\boldsymbol{P}(\boldsymbol{X}) = -\frac{1}{2}\int_{\boldsymbol{V}_{\boldsymbol{v}}}\int_{V_{\boldsymbol{u}}}\int_0^1 \varphi((1-\alpha)\boldsymbol{u}+\alpha\boldsymbol{v}-\boldsymbol{X})\boldsymbol{\mathcal{F}}(\boldsymbol{u},\boldsymbol{v})\otimes(\boldsymbol{u}-\boldsymbol{v})\,d\alpha\,d\boldsymbol{u}\,d\boldsymbol{v} \ . \tag{2.26}$$

Recalling the definition of $\boldsymbol{\mathcal{F}}(\boldsymbol{u},\boldsymbol{v})$ in (2.19), we finally obtain

$$\begin{aligned}\boldsymbol{P}(\boldsymbol{X}) &= -\frac{1}{2}\int_{V_{\boldsymbol{v}}}\int_{V_{\boldsymbol{u}}}\int_0^1 \varphi((1-\alpha)\boldsymbol{u}+\alpha\boldsymbol{v}-\boldsymbol{X}) \\ &\quad \sum_{I=1}^{N_X}\sum_{J=1,J\neq I}^{N_X} \boldsymbol{t}_{IJ}\delta(\boldsymbol{X}_I-\boldsymbol{u})\delta(\boldsymbol{X}_J-\boldsymbol{v})\otimes(\boldsymbol{u}-\boldsymbol{v})\,d\alpha\,d\boldsymbol{u}\,d\boldsymbol{v} \qquad (2.27)\\ &= -\frac{1}{2}\sum_{I=1}^{N_X}\sum_{J=1,J\neq I}^{N_X} \boldsymbol{t}_{IJ}\otimes(\boldsymbol{X}_I-\boldsymbol{X}_J)\int_0^1 \varphi((1-\alpha)\boldsymbol{u}+\alpha\boldsymbol{v}-\boldsymbol{X})\,d\alpha \qquad (2.28)\\ &= \frac{1}{2}\sum_{I=1}^{N_X}\sum_{J=1,J\neq I}^{N_X} \boldsymbol{t}_{IJ}\otimes(\boldsymbol{X}_J-\boldsymbol{X}_I)B_{IJ}(\boldsymbol{X})\ . \qquad \square\end{aligned}$$

For numerical implementation of the stress expression in (2.14), we need to select a window function that satisfies (2.16)-(2.18). Typical choices would be a Gaussian or a radial step function. Here, choose the radial step function:

$$\varphi(\boldsymbol{X'}-\boldsymbol{X}) = \begin{cases} \dfrac{1}{\Omega_{\boldsymbol{X}}}, & |\boldsymbol{X'}-\boldsymbol{X}|<\delta \\ \\ 0, & \text{otherwise}\ , \end{cases} \qquad (2.29)$$

where $\Omega_{\boldsymbol{X}}$ is the horizon volume and δ is the radius of the horizon $\mathcal{H}_{\boldsymbol{X}}$. For this choice, we can show that the bond function reduces to simply

$$B_{IJ}(\boldsymbol{X}) = \frac{1}{\Omega_{\boldsymbol{X}}}\ , \qquad \forall \boldsymbol{X}_I,\boldsymbol{X}_J\in\mathcal{H}_{\boldsymbol{X}}\ . \qquad (2.30)$$

Plugging the bond function into (2.14), we recover

$$\boldsymbol{P}(\boldsymbol{X}) = \frac{1}{2\Omega_{\boldsymbol{X}}}\sum_{I=1}^{N_X}\sum_{J=1,J\neq I}^{N_X} \boldsymbol{t}_{IJ}\otimes(\boldsymbol{X}_J-\boldsymbol{X}_I), \qquad \forall \boldsymbol{X}_I,\boldsymbol{X}_J\in\mathcal{H}_{\boldsymbol{X}}\ . \qquad (2.31)$$

where $\boldsymbol{t}_{IJ}=\boldsymbol{t}(\boldsymbol{X}_I,\boldsymbol{X}_J)V_IV_J$ is the bond force and $(\boldsymbol{X}_J-\boldsymbol{X}_I)=\boldsymbol{\xi}_{IJ}$ is the reference bond vector for the material points $\boldsymbol{X}_I$ and $\boldsymbol{X}_J$.

From (2.31), we can also get an expression for the Cauchy stress using the standard expression of the continuum mechanics,

$$\boldsymbol{\sigma} = J^{-1}\boldsymbol{P}\boldsymbol{F}^{T} \ , \tag{2.32}$$

where $J = det(\boldsymbol{F})$ is the Jacobian of the deformation and $\boldsymbol{F}$ is the nonlocal deformation gradient, as first defined by Silling [86, 85]. If the horizon is sufficiently small, the Jacobian can be approximated as the ratio between the horizon volumes in the deformed and reference configurations, that is, $J \approx \Omega_{\boldsymbol{x}}/\Omega_{\boldsymbol{X}}$. Assuming homogeneous deformation within the material horizon and adopting the first-order Cauchy-Born rule [97, 10], we get

$$\boldsymbol{F}(\boldsymbol{X}) \cdot (\boldsymbol{X}_J - \boldsymbol{X}_I) = (\boldsymbol{x}_J - \boldsymbol{x}_I), \qquad \forall \boldsymbol{X}_I \boldsymbol{X}_J \in \mathcal{H}_{\boldsymbol{X}}. \tag{2.33}$$

Substituting (2.33) into (2.32), we obtain an expression for the peridynamic Cauchy stress:

$$\boldsymbol{\sigma}(\boldsymbol{x}) = \frac{1}{2\Omega_{\boldsymbol{x}}} \sum_{I=1}^{N_X} \sum_{J=1, J\neq I}^{N_X} \boldsymbol{t}_{IJ} \otimes (\boldsymbol{x}_J - \boldsymbol{x}_I), \qquad \forall \boldsymbol{x}_I, \boldsymbol{x}_J \in \mathcal{H}_{\boldsymbol{x}} \ , \tag{2.34}$$

where $\boldsymbol{t}_{IJ} = \boldsymbol{t}(\boldsymbol{X}_I, \boldsymbol{X}_J) V_I V_J$ is the the bond force, $\Omega_{\boldsymbol{x}}$ is the volume of the horizon in the deformed configuration $\mathcal{H}_{\boldsymbol{x}}$, and $(\boldsymbol{x}_J - \boldsymbol{x}_I) = \boldsymbol{\zeta}_{IJ}$ is the deformed bond vector for the material points $\boldsymbol{x}_I$ and $\boldsymbol{x}_J$.

Note that the PK1 stress expression proposed in (2.31) is bond-based PD analog of the static first Piola-Kirchhoff Virial stress in molecular dynamics theory [37, 55]. If the PD particle spacing is sparse, the numerical value may be oscillatory, whereas a smooth stress distribution may be obtained by using a window function smoothed Hardy stress.

2.3 Constitutive Relations for Elastomers

In non-Gaussian chain statistics theory, Kuhn and Grün [49] idealized polymer molecules as a randomly jointed chain which consists of n rigid links of length l. As discussed by Treloar [93], with this idealization the free energy of a polymer chain with end-to-end length r can be described as

$$\phi_{KG}(r) = k\theta n \left[\frac{r}{nl}\beta + \ln\left(\frac{\beta}{\sinh\beta}\right)\right] \ , \tag{2.35}$$

where k is the Boltzmann constant, θ is the absolute temperature, and

$$\beta = \mathcal{L}^{-1}\left(\frac{r}{nl}\right) \ , \tag{2.36}$$

in which $\mathcal{L}(\beta)$ is the Langevin function, defined as

$$\mathcal{L}(\beta) = \coth\beta - \frac{1}{\beta} \ . \tag{2.37}$$

Chain stretch is defined as $\lambda = r/r_0$ where r_0 is the undeformed chain length, which can be determined from random walk statistics as $r_0 = \sqrt{n}l$. Due to the rigidity of the Kuhn segments, the deformation mechanism is simply the untangling of the randomly jointed chains so the maximum extension is limited by $r_{max} = nl$ which gives a maximum chain stretch of $\lambda_{max} = \sqrt{n}$. This mechanism is depicted in Fig. 2.3.

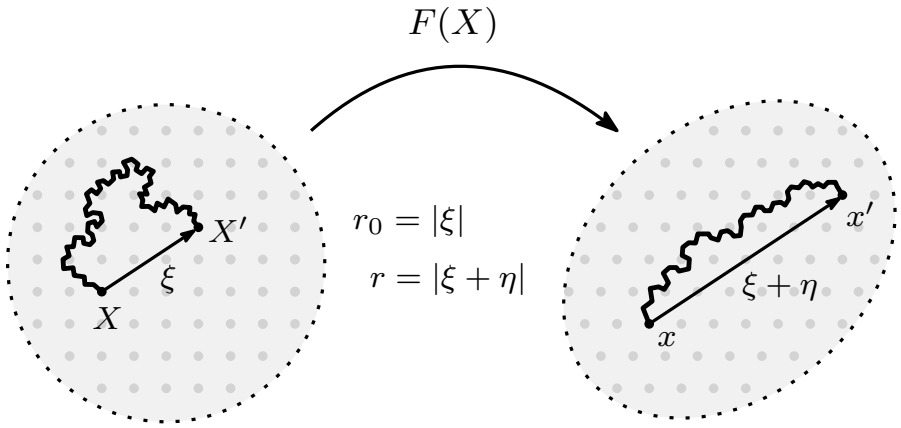

Figure 2.3: Peridynamic representation of a rubber chain with rigid Kuhn segments in the initial and deformed configurations. Dashed lines indicate the horizon and $F(X)$ refers to the nonlocal deformation gradient as discussed in (2.33).

Mao et al. [61] relaxed the rigidity of Kuhn segments by introducing an internal degree of freedom to account for the stretching of the atomic bonds and added a bond potential term to the original free energy expression (2.35). This model allowed them to simulate deformation beyond the $\sqrt{n}$ limit, hence modeling the rupture of elastomers via the chain scission mechanism [61, 89].

In our proposed non-local model, we treat each peridynamic bond to represent a unit cell that consists of multiple freely jointed polymer chains. We define $\overline{n}$ as *effective number of links*, which is the number of links per peridynamic bond. Considering the Arruda-Boyce 8-chain model [3], we choose $\overline{n} = 8n$. Next, we define $\overline{\lambda}$ to be *effective peridynamic stretch*, which is simply the stretch of a peridynamic bond, that is, $\overline{\lambda} = |\boldsymbol{\xi}+\boldsymbol{\eta}|/|\boldsymbol{\xi}|$. Using the network model described by Arruda and Boyce [3], we relate the effective peridynamic stretch ($\overline{\lambda}$) to the molecular chain stretch (λ) via

$$\overline{\lambda} = \sqrt{\frac{tr\overline{C}}{3}} = \sqrt{\frac{\lambda^{4/3} + 2\lambda^{-2/3}}{3}} \tag{2.38}$$

In light of the above definitions, we introduce a mesoscale potential for the nonlocal polymeric networks as follows.

$$\phi(\overline{\lambda}, \lambda_b) = k\theta\overline{n}\left[\frac{\overline{\lambda}}{\lambda_b\sqrt{\overline{n}}}\beta + \ln\left(\frac{\beta}{\sinh\beta}\right)\right]|\boldsymbol{\xi}| + \overline{n}\frac{1}{2}D(\ln\lambda_b)^2|\boldsymbol{\xi}| \tag{2.39}$$

where λ_b is the *Kuhn segment stretch*, D is the atomistic *bond stiffness* and

$$\beta = \mathcal{L}^{-1}\left(\frac{\overline{\lambda}}{\lambda_b\sqrt{\overline{n}}}\right) \ . \tag{2.40}$$

We postulate that the optimal value of the Kuhn segment stretch will minimize the potential energy. Thus, by invoking the condition $\partial\phi/\partial\lambda_b = 0$, we get the implicit relation between $\overline{\lambda}$ and λ_b as

$$D\ln(\lambda_b)\lambda_b = k\theta\frac{\overline{\lambda}}{\sqrt{\overline{n}}}\beta \ . \tag{2.41}$$

In the expression above, $(k\theta)$ can be grouped together to be referred to as *rubber modulus*, which will be linked to the macroscale elastic constants of the material. We can freely choose the number of links $\overline{n}$ to model a wide range of polymers. The bond constant D has dimensions of energy and can be computed by using molecular dynamics (MD) or density functional theory (DFT) simulations considering the backbones of the polymer at the equilibrium bond length. Mao et al. reported that the DFT simulation using VASP resulted in $D = 2300k\theta$ for C-C bonds at equilibrium bond length [61].

The bond force density that corresponds to the potential introduced in (2.39) can be derived as follows. Consider the definition of the Langevin function,

$$\frac{\overline{\lambda}}{\lambda_b\sqrt{\overline{n}}} = \coth\beta - \frac{1}{\beta} \tag{2.42}$$

we get the equality,

$$\frac{\partial}{\partial\beta}\left[\ln\left(\frac{\beta}{\sinh\beta}\right)\right] = \frac{1}{\beta} - \coth\beta = -\frac{\overline{\lambda}}{\lambda_b\sqrt{\overline{n}}} \tag{2.43}$$

Taking the partial derivative of the potential function with respect to λ_b and using (2.43),

$$\frac{\partial}{\partial\lambda_b}\phi(\overline{\lambda},\lambda_b) = k\theta\overline{n}\left[-\frac{\overline{\lambda}}{{\lambda_b}^2\sqrt{\overline{n}}}\beta + \frac{\overline{\lambda}}{\lambda_b\sqrt{\overline{n}}}\frac{\partial\beta}{\partial\lambda_b} - \frac{\overline{\lambda}}{\lambda_b\sqrt{\overline{n}}}\frac{\partial\beta}{\partial\lambda_b}\right] + \overline{n}D(\ln\lambda_b)\frac{1}{\lambda_b}\ . \tag{2.44}$$

Invoking the postulate $\partial\phi/\partial\lambda_b = 0$, we get the relation between $\overline{\lambda}$ and λ_b as

$$D\ln(\lambda_b)\lambda_b = k\theta\frac{\overline{\lambda}}{\sqrt{\overline{n}}}\beta\ . \tag{2.45}$$

Proceeding similarly for the derivation of the bond force density $\boldsymbol{t}(\overline{\lambda},\lambda_b)$, we start by taking the partial derivative of the potential with respect to $\overline{\lambda}$, using (2.43) we get

$$\frac{\partial\phi(\overline{\lambda},\lambda_b)}{\partial\overline{\lambda}} = k\theta\overline{n}\left[\frac{1}{\lambda_b\sqrt{\overline{n}}}\beta + \frac{\overline{\lambda}}{\lambda_b\sqrt{\overline{n}}}\frac{\partial\beta}{\partial\overline{\lambda}} - \frac{\overline{\lambda}}{\lambda_b\sqrt{\overline{n}}}\frac{\partial\beta}{\partial\overline{\lambda}}\right] = k\theta\sqrt{\overline{n}}\frac{\beta}{\lambda_b}\ . \tag{2.46}$$

Therefore, the bond force density becomes

$$\boldsymbol{t}(\overline{\lambda},\lambda_b) = \frac{\partial\phi(\overline{\lambda},\lambda_b)}{\partial\boldsymbol{\eta}} = \frac{\partial\phi(\overline{\lambda},\lambda_b)}{\partial\overline{\lambda}}\frac{\partial\overline{\lambda}}{\partial\boldsymbol{\eta}} = k\theta\sqrt{\overline{n}}\frac{\beta}{\lambda_b}\frac{\boldsymbol{\zeta}}{|\boldsymbol{\zeta}|} \tag{2.47}$$

In the expression above, $(k\theta)$ can be grouped together to be referred to as *rubber modulus*, which will be linked to the macroscale elastic constants of the material. We can freely choose the number of links $\overline{n}$ to model a wide range of polymers. The bond constant D has dimensions of energy and can be computed by using molecular dynamics (MD) or density functional theory (DFT) simulations considering the backbones of the polymer at the equilibrium bond length. Mao et al. reported that the DFT simulation using VASP resulted in $D = 2300k\theta$ for C-C bonds at equilibrium bond length [61].

The inverse Langevin function that appears in the bond force does not have a closed form, but there are many forms of approximate expressions of the inverse Langevin function in the literature [39]. One popular choice is to use the Padé approximation proposed by Cohen [18]: $\mathcal{L}^{-1}(x) \approx x(3-x^2)/(1-x^2)$. This approximation is valid for the entire domain $(-1,1)$, and it is simple yet accurate enough for robust numerical implementation. For a discussion of approximate forms of the inverse Langevin function, readers may consult [39].

The bond force density should vanish beyond a stretch level, which we will refer to as *critical effective stretch* $\overline{\lambda}_{crit}$. This quantity depends on how much strain the polymer backbones can sustain, which can be found by using MD or DFT simulations, e.g. [41, 40]. For example, if we assume that the C-C bonds fail at 20% strain, the critical molecular stretch becomes $\lambda_{crit} = 1.2\sqrt{n}$ which is linked to $\overline{\lambda}_{crit}$ via (2.38) and this value can be used to break the peridynamic bonds during the time evolution of the numerical model. Note that the bond failure strain can be precisely computed via DFT simulations if desired.

Now we would like to identify the last remaining piece of our model, the rubber modulus ($k\theta$), and eventually link it to the macroscale elastic constants. For this purpose we shift our attention to the energy principles, and we start by defining the nonlocal macroscale strain energy density:

$$W(\boldsymbol{X}) = \frac{1}{2\Omega_{\boldsymbol{X}}} \int_{\mathcal{H}_{\boldsymbol{X}}} \int_{\mathcal{H}_{\boldsymbol{X}}} \phi(\boldsymbol{\eta}, \boldsymbol{\xi}) d\boldsymbol{X}' d\boldsymbol{X}'' \ , \tag{2.48}$$

where $\mathcal{H}_{\boldsymbol{X}}$ denotes the peridynamic horizon of the material point $\boldsymbol{X}$. Double integration implies that we are counting all the bonds within the horizon, not only those connected to $\boldsymbol{X}$, as illustrated in Fig. 2.4. Note that $\overline{\lambda}$ and thus λ_b depend only on the reference and deformed peridynamic bonds, $\boldsymbol{\xi}$ and $\boldsymbol{\eta}$ respectively, so it is natural to denote the potential as $\phi(\boldsymbol{\eta}, \boldsymbol{\xi})$ and the bond force density as $\boldsymbol{t}(\boldsymbol{\eta}, \boldsymbol{\xi})$.

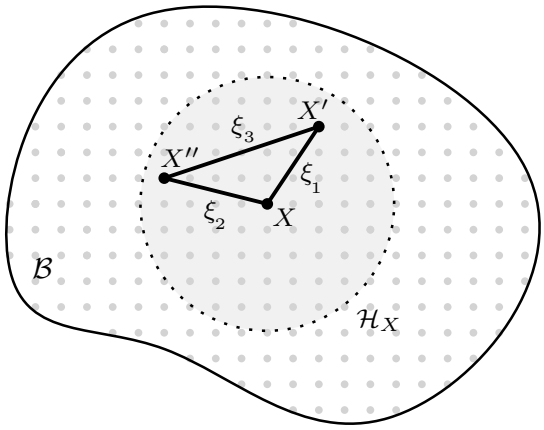

Figure 2.4: Particle interactions inside the horizon

Assuming homogeneous deformation within the material horizon and adopting the first-order Cauchy-Born rule, the following relations hold:

$$\boldsymbol{F}(\boldsymbol{X}) \cdot \boldsymbol{\xi} = \boldsymbol{\xi} + \boldsymbol{\eta} \ , \qquad \forall \boldsymbol{\xi} \in \mathcal{H}_{\boldsymbol{X}} \tag{2.49}$$

$$\frac{\partial}{\partial \boldsymbol{F}}(\boldsymbol{F}(\boldsymbol{X}) \cdot \boldsymbol{\xi}) = \frac{\partial}{\partial \boldsymbol{F}}(\boldsymbol{\xi} + \boldsymbol{\eta}) \quad \rightarrow \quad \frac{\partial \boldsymbol{\eta}}{\partial \boldsymbol{F}} = \mathbf{I}^{(2)} \otimes \boldsymbol{\xi} \ , \tag{2.50}$$

where $\boldsymbol{F}(\boldsymbol{X})$ is the constant deformation gradient in $\mathcal{H}_{\boldsymbol{X}}$ and $\mathbf{I}^{(2)}$ is the second order identity tensor. Using the above approximations, we can now derive the PK1 stress tensor at $\boldsymbol{X}$ as

$$\boldsymbol{P}(\boldsymbol{X}) = \frac{\partial W(\boldsymbol{X})}{\partial \boldsymbol{F}} \tag{2.51}$$

$$= \frac{1}{2\Omega_{\boldsymbol{X}}} \int_{\mathcal{H}_{\boldsymbol{X}}} \int_{\mathcal{H}_{\boldsymbol{X}}} \frac{\partial \phi(\boldsymbol{\eta}, \boldsymbol{\xi})}{\partial \boldsymbol{\eta}} \cdot \frac{\partial \boldsymbol{\eta}}{\partial \boldsymbol{F}} dX' dX'' \tag{2.52}$$

$$= \frac{1}{2\Omega_{\boldsymbol{X}}} \int_{\mathcal{H}_{\boldsymbol{X}}} \int_{\mathcal{H}_{\boldsymbol{X}}} \big[\boldsymbol{t}(\boldsymbol{\eta}, \boldsymbol{\xi}) \otimes \boldsymbol{\xi}\big] dX' dX'' \ . \tag{2.53}$$

Similarly, we can derive the Cauchy stress:

$$\boldsymbol{\sigma}(\boldsymbol{x}) = J^{-1} \boldsymbol{P} \boldsymbol{F}^T \tag{2.54}$$

$$= \frac{\Omega_{\boldsymbol{X}}}{\Omega_{\boldsymbol{x}}} \frac{1}{2\Omega_{\boldsymbol{X}}} \int_{\mathcal{H}_{\boldsymbol{X}}} \int_{\mathcal{H}_{\boldsymbol{X}}} \big[\boldsymbol{t}(\boldsymbol{\eta}, \boldsymbol{\xi}) \otimes \boldsymbol{\xi} \cdot \boldsymbol{F}^T\big] dX' dX'' \tag{2.55}$$

$$= \frac{1}{2\Omega_{\boldsymbol{x}}} \int_{\mathcal{H}_{\boldsymbol{X}}} \int_{\mathcal{H}_{\boldsymbol{X}}} \big[\boldsymbol{t}(\boldsymbol{\eta}, \boldsymbol{\xi}) \otimes \boldsymbol{\zeta}\big] dX' dX'' \ . \tag{2.56}$$

Peridynamic stress expressions derived by using the Hardy-Noll formalism, (2.13) and (2.34), are the discrete analogs of the PK1 and Cauchy stress obtained from the hyperelastic assumption here.

Peridynamic Cauchy stress of the polymeric network micropotential (2.39) is symmetric.

Proof. If we plug in the force density expression (2.47) into (2.56), we can immediately see the symmetric nature of the tensor:

$$\boldsymbol{\sigma}(\boldsymbol{x}) = \frac{1}{2\Omega_{\boldsymbol{x}}} \int_{\mathcal{H}_{\boldsymbol{X}}} \int_{\mathcal{H}_{\boldsymbol{X}}} k\theta\sqrt{n} \frac{\beta}{\lambda_b} \frac{1}{|\boldsymbol{\zeta}|} (\boldsymbol{\zeta} \otimes \boldsymbol{\zeta}) \, dX' dX'' \ . \tag{2.57}$$

Alternatively, for numerical applications, we consider the discrete version in (2.32) and substitute for $\boldsymbol{t}_{IJ} = \boldsymbol{t}(\boldsymbol{\eta}, \boldsymbol{\xi}) V_I V_J$ using (2.47):

$$\boldsymbol{\sigma}(\boldsymbol{x}) = \frac{1}{2\Omega_{\boldsymbol{x}}} \sum_{I=1}^{N_X} \sum_{J=1, J\neq I}^{N_X} \boldsymbol{t}_{IJ} \otimes (\boldsymbol{x}_J - \boldsymbol{x}_I) \tag{2.58}$$

$$= \frac{1}{2\Omega_{\boldsymbol{x}}} \sum_{I=1}^{N_X} \sum_{J=1, J\neq I}^{N_X} k\theta\sqrt{n} \frac{\beta}{\lambda_b} \frac{1}{|\boldsymbol{x}_J - \boldsymbol{x}_I|} (\boldsymbol{x}_J - \boldsymbol{x}_I) \otimes (\boldsymbol{x}_J - \boldsymbol{x}_I) \ . \tag{2.59}$$

□

To establish the connection between the rubber modulus ($k\theta$) and the constitutive relations of the macro-scale continuum, we can evaluate the elasticity tensor $\mathbb{C}$ arising from the

micro potential and solve for the rubber modulus assuming linear elastic isotropic behavior at zero deformation.

Consider the fourth-order tensor,

$$\mathbb{C}'(\boldsymbol{X}) = \frac{\partial^2 W(\boldsymbol{X})}{\partial \boldsymbol{F} \partial \boldsymbol{F}} = \frac{1}{2\Omega_{\boldsymbol{X}}} \int_{\mathcal{H}_{\boldsymbol{X}}} \int_{\mathcal{H}_{\boldsymbol{X}}} \left[\frac{\partial}{\partial \boldsymbol{\eta}} \boldsymbol{t}(\boldsymbol{\eta}, \boldsymbol{\xi}) \right] \otimes (\boldsymbol{\xi} \otimes \boldsymbol{\xi}) d\boldsymbol{X}' d\boldsymbol{X}'' \ , \tag{2.60}$$

which can be mapped to the elasticity tensor through $\mathbb{C}_{ijkl}(\boldsymbol{X}) = \mathbb{C}'_{ikjl}(\boldsymbol{X})$.

By the chain rule, the term inside the brackets becomes

$$\frac{\partial \boldsymbol{t}(\lambda, \lambda_b)}{\partial \boldsymbol{\eta}} = \frac{\partial \boldsymbol{t}}{\partial \lambda} \frac{\partial \lambda}{\partial \boldsymbol{\eta}} + \frac{\partial \boldsymbol{t}}{\partial \lambda_b} \frac{\partial \lambda_b}{\partial \lambda} \frac{\partial \lambda}{\partial \boldsymbol{\eta}} \ . \tag{2.61}$$

The first term of (2.61) reads as follows.

$$\frac{\partial \boldsymbol{t}}{\partial \lambda} \frac{\partial \lambda}{\partial \boldsymbol{\eta}} = \frac{k\theta\sqrt{\overline{n}}}{\lambda_b} \left[\left(\frac{\partial \beta}{\partial \lambda} \frac{1}{|\boldsymbol{\xi}|} \frac{1}{|\boldsymbol{\zeta}|^2} - \beta \frac{1}{|\boldsymbol{\zeta}|^3} \right) (\boldsymbol{\zeta} \otimes \boldsymbol{\zeta}) + \frac{1}{|\zeta|} \beta \mathbf{I} \right] \ . \tag{2.62}$$

Similarly, the second term becomes

$$\frac{\partial \boldsymbol{t}}{\partial \lambda_b} \frac{\partial \lambda_b}{\partial \lambda} \frac{\partial \lambda}{\partial \boldsymbol{\eta}} = \frac{k\theta\sqrt{\overline{n}}}{|\boldsymbol{\xi}||\boldsymbol{\zeta}|^2} \left[\frac{\partial \beta}{\partial \lambda_b} \frac{1}{\lambda_b} - \frac{\beta}{\lambda_b^2} \right] \frac{\partial \lambda_b}{\partial \lambda} (\boldsymbol{\zeta} \otimes \boldsymbol{\zeta}) \ . \tag{2.63}$$

We now need to solve for $\partial \lambda_b / \partial \lambda$. Starting with $\partial \phi / \partial \lambda_b = 0$ and taking the total derivative, we get

$$\frac{D}{D\lambda} \left(\frac{\partial \phi}{\partial \lambda_b} = 0 \right) \quad \rightarrow \quad \frac{\partial^2 \phi}{\partial \lambda \partial \lambda_b} + \frac{\partial^2 \phi}{\partial \lambda_b \partial \lambda_b} \frac{\partial \lambda_b}{\partial \lambda} = 0 \ . \tag{2.64}$$

Isolating the term we are looking for:

$$\frac{\partial \lambda_b}{\partial \lambda} = - \left(\frac{\partial^2 \phi}{\partial \lambda_b \partial \lambda_b} \right)^{-1} \left(\frac{\partial^2 \phi}{\partial \lambda \partial \lambda_b} \right) \ . \tag{2.65}$$

Now we need to find the second partial derivatives of the bond potential. Starting with

$$\frac{\partial \phi}{\partial \lambda} = k\theta\sqrt{\overline{n}} \frac{\beta}{\lambda_b} \ , \tag{2.66}$$

$$\frac{\partial \phi}{\partial \lambda_b} = D \frac{\ln \lambda_b}{\lambda_b} - k\theta\sqrt{\overline{n}} \frac{\beta \lambda}{{\lambda_b}^2} \ , \tag{2.67}$$

we find that

$$\frac{\partial^2 \phi}{\partial \lambda \partial \lambda_b} = - \frac{k\theta\sqrt{\overline{n}}}{\lambda_b^2} \left[\beta + \lambda \frac{\partial \beta}{\partial \lambda} \right] \ , \tag{2.68}$$

$$\frac{\partial^2 \phi}{\partial \lambda_b \partial \lambda_b} = D \left[- \frac{\ln \lambda_b}{\lambda_b^2} + \frac{1}{\lambda_b^2} \right] - k\theta\sqrt{\overline{n}} \lambda \left[\frac{\partial \beta}{\partial \lambda_b} \frac{1}{\lambda_b^2} - \frac{2\beta}{\lambda_b^3} \right] \ . \tag{2.69}$$

At zero deformation, $\lambda = 1$ and $\lambda_b = 1$ thus $\beta \to 0$ and we have the limits.

$$\lim_{\beta\to 0} \frac{\partial \beta}{\partial \lambda} = \frac{3}{\sqrt{\overline{n}}} \ , \tag{2.70}$$

$$\lim_{\beta\to 0} \frac{\partial \beta}{\partial \lambda_b} = \frac{-3}{\sqrt{\overline{n}}} \ . \tag{2.71}$$

Bringing everything together, we evaluate the tensor $\mathbb{C}'(\boldsymbol{X})$ at zero deformation as

$$\mathbb{C}'(\boldsymbol{X}) \Big|_{\boldsymbol{\eta}=0} = \frac{1}{2\Omega_{\boldsymbol{X}}} \int_{\mathcal{H}_{\boldsymbol{X}}} \int_{\mathcal{H}_{\boldsymbol{X}}} \left(3k\theta - \frac{9(k\theta)^2}{D + 3k\theta} \right) \frac{1}{|\boldsymbol{\xi}^3|} (\boldsymbol{\xi} \otimes \boldsymbol{\xi} \otimes \boldsymbol{\xi} \otimes \boldsymbol{\xi}) d\boldsymbol{X}' d\boldsymbol{X}'' \ . \tag{2.72}$$

Evaluation of the above integral in the horizon is somewhat cumbersome, hence we will only present the result; a detailed discussion can be found in the appendix. For 3D and plane strain problems, we pick a spherical peridynamic horizon, $\Omega_{\boldsymbol{X}} = 4/3\pi R^3$, and the integral is evaluated as

$$\frac{1}{2\Omega_{\boldsymbol{X}}} \int_{\mathcal{H}_{\boldsymbol{X}}} \int_{\mathcal{H}_{\boldsymbol{X}}} \frac{1}{|\boldsymbol{\xi}^3|} (\boldsymbol{\xi} \otimes \boldsymbol{\xi} \otimes \boldsymbol{\xi} \otimes \boldsymbol{\xi}) dX' dX'' = \frac{R^4 \pi}{15} (\delta_{ij}\delta_{kl} + \delta_{ik}\delta_{jl} + \delta_{il}\delta_{jk}) \ . \tag{2.73}$$

Therefore, the elasticity tensor at zero deformation is read as

$$\mathbb{C}(\boldsymbol{X}) \Big|_{\boldsymbol{\eta}=0} = \left(3k\theta - \frac{9(k\theta)^2}{D + 3k\theta} \right) \frac{R^4 \pi}{15} (\delta_{ik}\delta_{jl} + \delta_{ij}\delta_{kl} + \delta_{il}\delta_{kj}) \ . \tag{2.74}$$

For an isotropic linear elastic solid, we have the following standard relations.

$$\mathbb{C}_{1111} = \frac{E(1-\nu)}{(1+\nu)(1-2\nu)} \qquad\qquad \mathbb{C}_{1122} = \frac{E\nu}{(1+\nu)(1-2\nu)} \ , \tag{2.75}$$

where E is the elastic modulus and ν is the Poisson's ratio of the material.

We can ignore the second term inside the parentheses in (2.74) since the denominator is large, that is, $D = 2500k\theta$. Finally, using (2.75), we obtain the rubber modulus as

$$k\theta = \frac{2E}{R^4 \pi} \tag{2.76}$$

along with $\nu = 1/3$. Note that the restriction on the Poisson's ratio is a natural outcome of the ordinary bond-based peridynamics.

For the plane stress conditions, we can get the rubber modulus in a similar fashion. Assuming thickness t in the e_3 direction, the horizon has volume $\Omega_{\boldsymbol{X}} = \pi R^2 t$ and the integral is evaluated as

$$\frac{1}{2\Omega_{\boldsymbol{X}}} \int_{\mathcal{H}_{\boldsymbol{X}}} \int_{\mathcal{H}_{\boldsymbol{X}}} \frac{1}{|\boldsymbol{\xi}^3|} (\boldsymbol{\xi} \otimes \boldsymbol{\xi} \otimes \boldsymbol{\xi} \otimes \boldsymbol{\xi}) d\boldsymbol{X}' d\boldsymbol{X}'' = \frac{tR^3 \pi}{12} (\delta_{ij}\delta_{kl} + \delta_{ik}\delta_{jl} + \delta_{il}\delta_{jk}) \ . \tag{2.77}$$

and the elasticity tensor becomes

$$\mathbb{C}(\boldsymbol{X})\Big|_{\boldsymbol{\eta}=0} = \left(3k\theta - \frac{9(k\theta)^2}{D+3k\theta}\right)\frac{tR^3\pi}{12}(\delta_{ik}\delta_{jl}+\delta_{ij}\delta_{kl}+\delta_{il}\delta_{kj}) \ . \tag{2.78}$$

Using the isotropic linear elastic plane stress conditions,

$$\mathbb{C}_{1111} = \frac{E}{(1-\nu^2)} \qquad\qquad \mathbb{C}_{1122} = \frac{E\nu}{(1-\nu^2)} \ , \tag{2.79}$$

we get the rubber modulus as

$$k\theta = \frac{3E}{2tR^3\pi} \ , \tag{2.80}$$

and the restriction on the Poisson's ratio $\nu = 1/4$.

2.4 Numerical Examples

In this section, we present a series of numerical examples to demonstrate the validity as well as capabilities of our nonlocal polymer network model. All numerical simulations are conducted using an in-house MATLAB program on a standard workstation.

Discrete version of the peridynamic equation of motion (2.6) is solved using the Adaptive Dynamic Relaxation scheme, as described by Madenci et al. [58, 96] . The purpose of this method is to obtain the steady-state solution of the dynamic problem by introducing an artificial damping to the system. In essence, we find the critical damping coefficient at each time step that corresponds to the first mode of the system and use this to solve the equation of motion via a central difference scheme, which leads us to the quasi-static solution.

One caveat of our proposed nonlocal polymer network model is the need to calculate the effective bond stretch λ_b at each time step by solving the implicit relation (2.41) for a given λ. Doing this on-the-fly, for instance, by using a Newton-Raphson scheme at each time step, is quite expensive considering the number of peridynamic bonds in the domain. Our current approach is to solve (2.41) for a given set of material parameters before time integration and interpolate the resulting relation at each time step for the current λ. A linear interpolation, as implemented in [14] is used. Although the interpolation is also not cheap and may introduce another layer of numerical error, it is certainly more robust than the on-the-fly approach.

Plate with a Hole: Stress Verification and Convergence Study

To verify our stress expression and the proposed elastomer micropotential, we begin with a well-established benchmark problem in elastostatics: a plate with a hole experiencing uniaxial tension. We consider a thin plate with a circular hole of radius a in the middle, exposed to remote tensile stress $\boldsymbol{\sigma}^\infty$, as depicted in Fig. 4(a). The analytical solution to this problem is provided in polar coordinates by the famous Kirch's equations [45], which do not depend on the properties of the material. The stress components in Cartesian coordinates are described as follows.

$$\sigma_{xx}(r,\theta) = \sigma^\infty - \sigma^\infty \frac{a^2}{r^2}\left(\frac{3}{2}\cos 2\theta + \cos 4\theta\right) + \sigma^\infty \frac{3a^4}{2r^4}\cos 4\theta \ , \tag{2.81}$$

$$\sigma_{yy}(r,\theta) = -\sigma^\infty \frac{a^2}{r^2}\left(\frac{1}{2}\cos 2\theta - \cos 4\theta\right) - \sigma^\infty \frac{3a^4}{2r^4}\cos 4\theta \ , \tag{2.82}$$

$$\sigma_{xy}(r,\theta) = -\sigma^\infty \frac{a^2}{r^2}\left(\frac{1}{2}\sin 2\theta + \sin 4\theta\right) + \sigma^\infty \frac{3a^4}{2r^4}\sin 4\theta \ . \tag{2.83}$$

We chose a thin plate with dimensions 1000×1000 mm and a thickness of $t = 10$ mm. In the center of the plate, we place a circular hole with a radius of $a = 60$ mm. To examine the mesh sensitivity and convergence to the analytical solution, we use different particle

spacings;$\Delta X = \{4, 2, 1\}$ mm, while keeping the horizon size constant at $\delta = 3.015\Delta X$. In the x-direction, we impose traction boundary conditions as a uniform body force within the boundary layers. The number of boundary layers is chosen as the same as the horizon radius, which is a standard practice in PD. The domain and boundary conditions are depicted in Fig.2.5.

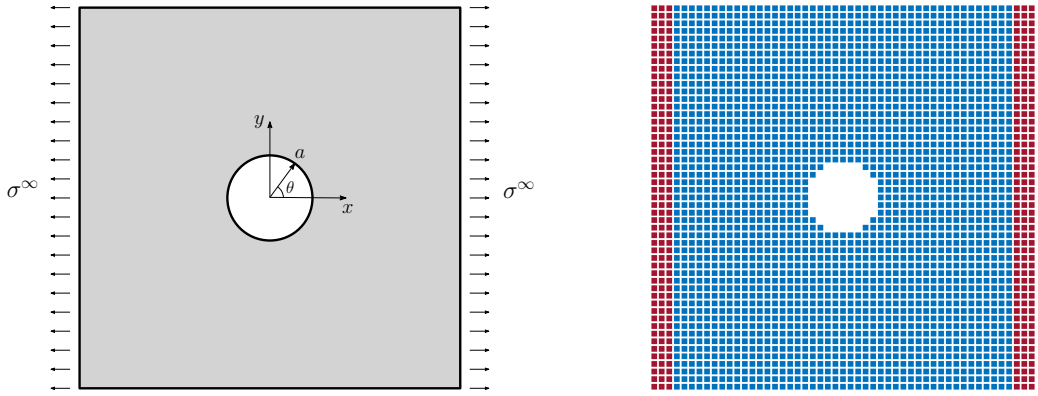

Figure 2.5: (a) Plate with a hole under remote uniaxial stress, (b) Peridynamic domain of the problem; red indicates the boundary particles where the body forces are applied.

In Fig.2.6, we present the resulting peridynamic Cauchy stress components around the hole, normalized by the far-field stress σ^∞. We plot the normalized σ_{11} stress varied in the radial direction at $\theta = \pi/2$, along with the Kirch's solution around the hole in Fig.2.7. From the results shown in Figs. 5 and 6, it is evident that both the stress distribution and the stress concentration factor converge to the analytical solution as the particle spacing gets smaller. This validates the use of the proposed peridynamic stress formulation along with our polymeric network potential.

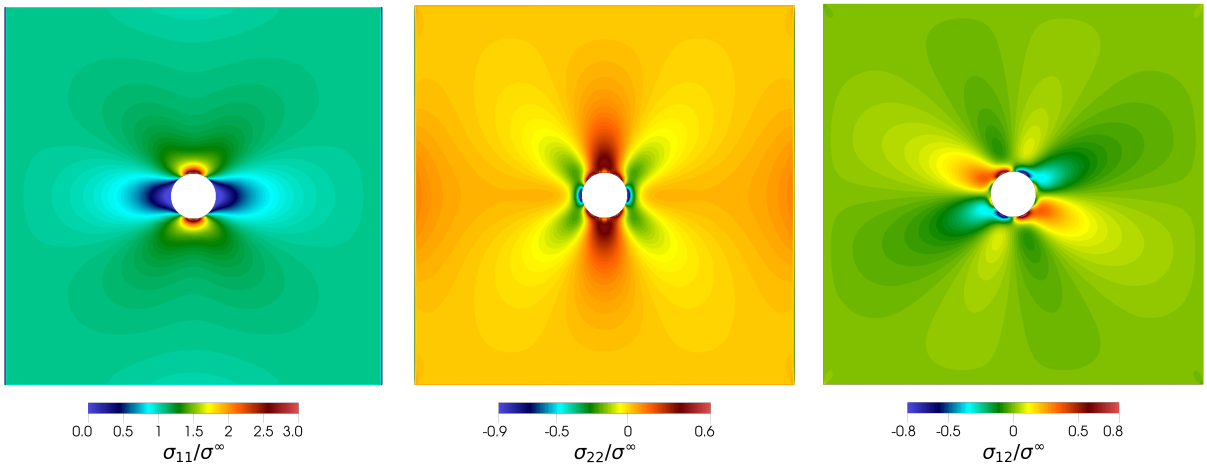

Figure 2.6: Normalized Cauchy stress distribution around the hole.

To further investigate the numerical behavior of the peridynamics solution, we conducted *m-convergence* and Δ-*convergence* analysis. In this context, we define m to be the ratio between the horizon radius and the particle spacing, namely $m = \delta/\Delta X$. To assess the convergence rate, root-mean-square error (RMSE) of stress is employed which is defined as

$$RMSE(\sigma) = \left[\sum_{i=1}^{N} \frac{(\sigma_{PD} - \sigma_{Cont})^2}{N}\right]^{0.5} \tag{2.84}$$

where σ_{PD} is the numerical solution, σ_{Cont} is the continuum mechanics solution given by the Kirch's equations and N is the total number of particles in the problem domain.

For the analysis, we choose the m values as $m = \{3, 4, 6, 8\}$ and the particle spacings as $\Delta X = \{1, 2, 4, 5\}$ mm. The results are shown in Fig.2.8 in log-log scale. As m decreases, the numerical solution converges to the local solution for all the choices of ΔX, as expected. We observed that $m = 3$ gave us the most accurate results and is computationally feasible; hence the horizon radius $\delta = 3.015\Delta X$ is employed for the rest of this study.

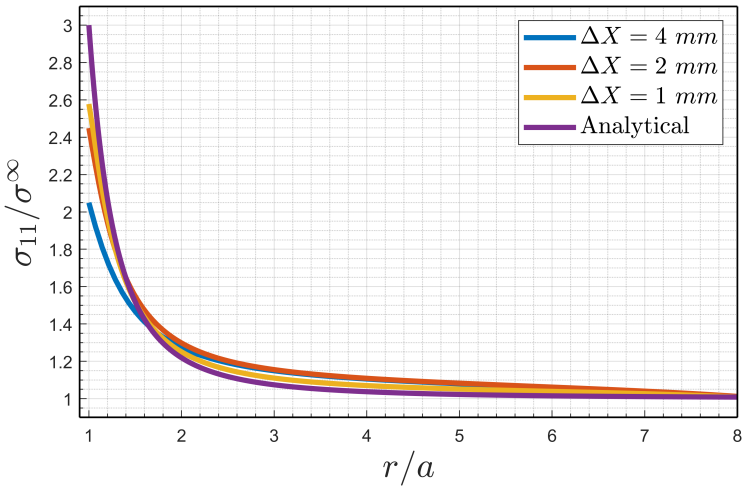

Figure 2.7: Comparison of the normalized stress variation $\sigma_{11}(r, \pi/2)/\sigma^{\infty}$ in the radial direction for different particle spacing and Kirch's solution.

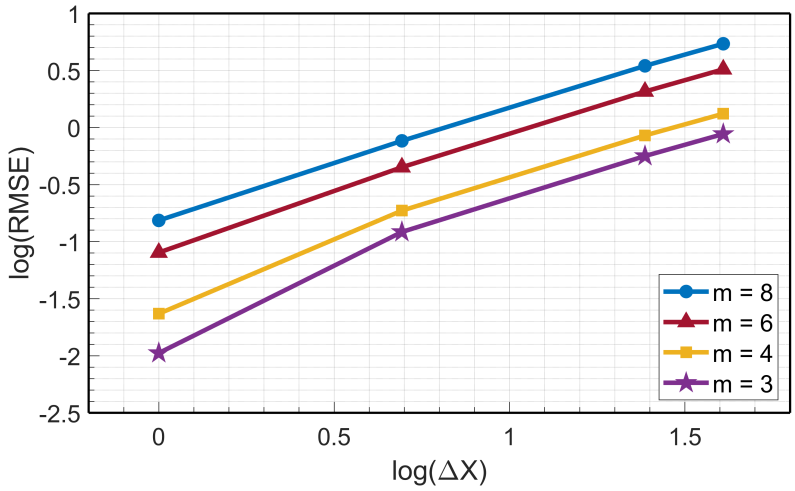

Figure 2.8: m and Δ-convergence for the plate-with a hole problem.

Double-edge-notch under tension (DENT)

In this example, we simulate a double edge notch specimen in tension (DENT) and compare it with the experimental data obtained from Hocine et al. [30]. Previously, other numerical simulations such as the phase field model [89] and state-based peridynamics [7], were also compared with this experimental data. The geometric setup and the corresponding peridynamic model are shown in Fig. 2.12, where the initial crack length is chosen having the following values $a = \{12, 20, 28\}$ mm. The particle spacing is set to $\Delta X = 2$ mm and the horizon radius is chosen as $\delta = 3.015\Delta X$.

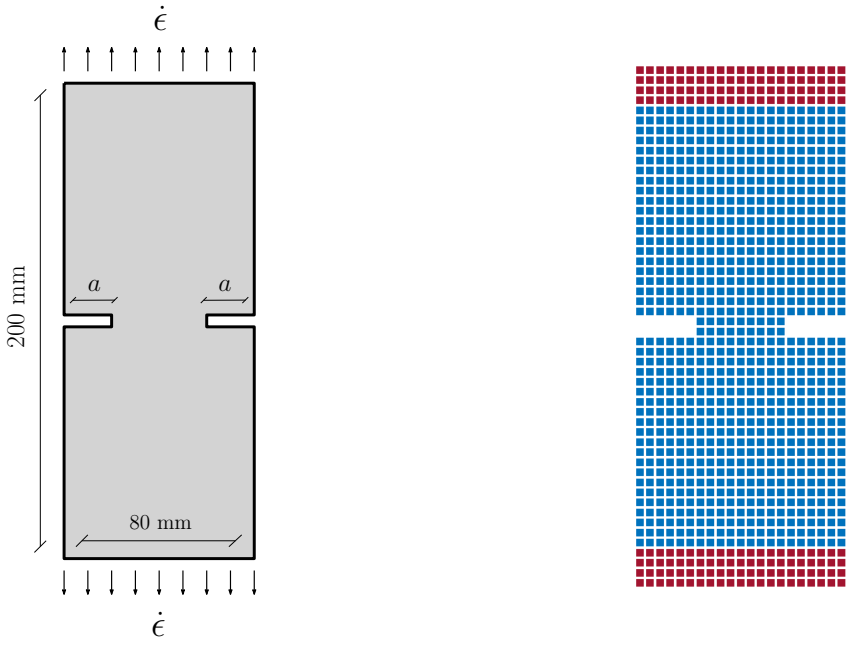

Figure 2.9: (a) Geometry of the double edge notch specimen, (b) Peridynamic model of the DENT simulation; displacement boundary conditions enforced to red particles.

The material considered is polybutadine, which is a synthetic rubber, and it is modeled by an elastic modulus $E = 0.6$ N/mm^2 and a Poisson's ratio $\nu = 1/3$ in the plane stress conditions. The bond constant is chosen as $D = 1200\ k_b\theta$, number of chains per peridynamic bond is $\overline{n} = 720$ and the critical bond stretch is set to $\lambda_{critical} = 1.2\sqrt{n}$.

The specimen is stretched by a monotonic displacement boundary condition until a complete rupture is observed. Cauchy stress is calculated using the formulation discussed in Section 2, and the contours of σ_{22} are plotted in different time steps, as shown in Fig. 2.10. The stress concentration in the vicinity of the crack is clearly captured. The growth or propagation of the crack is observed, followed by the rupture of the specimen, as illustrated in a sequence of computations shown in Fig. 2.10.

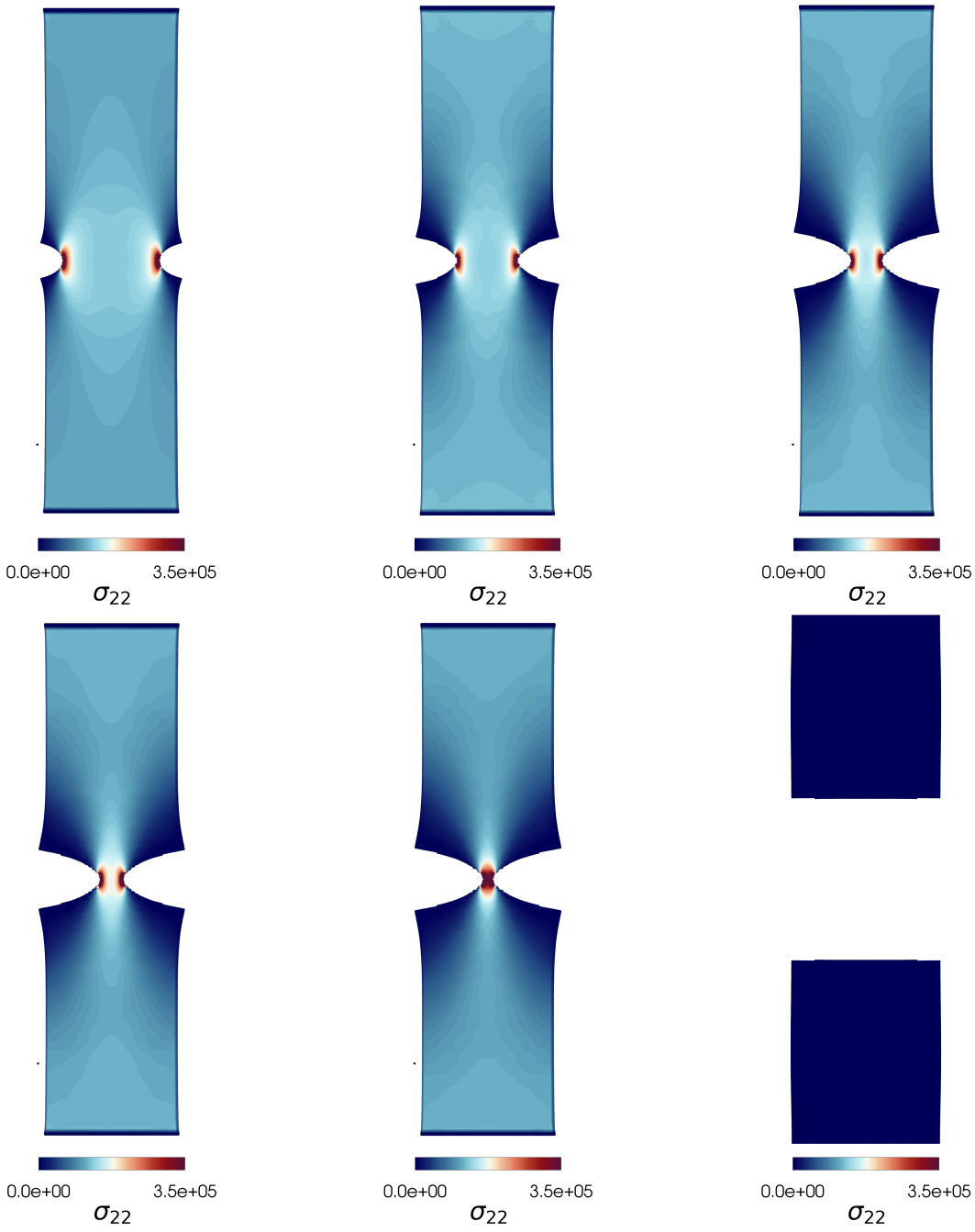

Figure 2.10: Stress distribution of the DENT specimen during different stages of the deformation. σ_{22} is the Cauchy stress component in the direction of load, given in (Pa).

The load-displacement curves are obtained for each choice of initial crack length and are plotted against the experimental data [30], as shown in Fig. 2.11. From Fig. 2.11, one may find that the proposed peridynamic polymer model successfully captures the critical failure displacement and the ultimate load in simulations with $a = \{12, 20\}$ mm, but may underestimate the strength of the material in the elastic region. Moreover, the strain hardening behavior, intrinsic to the Arruda-Boyce model, is observed in our proposed model.

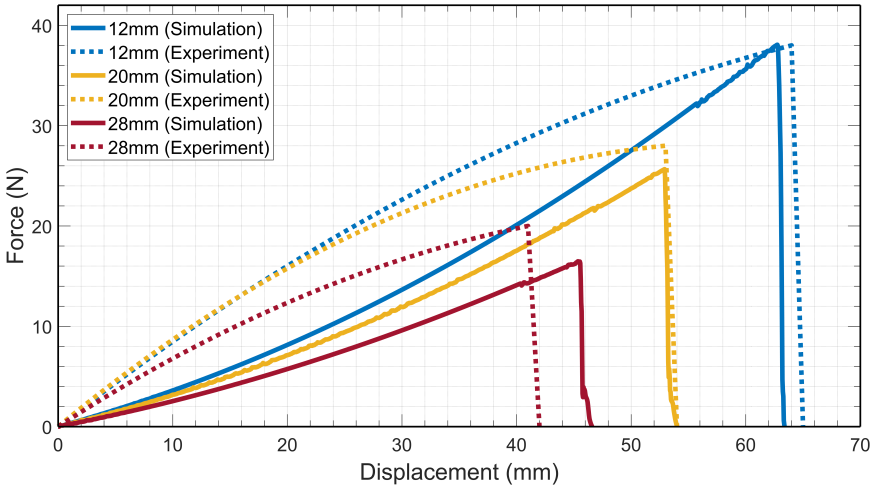

Figure 2.11: Load-displacement results for the DENT specimen with varying notch size (solid lines), compared to the experimental data from Hotcine et al. (dashed lines [30]).

Square Plate: Mode-I Crack Opening

The purpose of the numerical examples reported in this section is to use the proposed peridynamic polymer model to tackle standard Mode I fracture problems in elastic fracture mechanics. Our aim is to investigate the resulting crack patterns and fracture behaviors of polymeric networks and to understand their dependence on the initial crack or notch configuration. We consider a square plate with side length $L = 300$ mm. Two different initial configurations are considered. First, a preexisting crack is placed in its middle section with dimensions $C_L = 40$ mm and $C_W = 4\Delta X$, as shown in Figs. 2.12(a,b). Next, we placed several voids around the same location as the crack. Each void has dimensions $(3\Delta X \times 4\Delta X)$ and they are aligned in the middle section of the specimen up to the crack length of the first configuration, as depicted in Fig. 2.12 (c).

The plate is thin in the out-of-plane direction, and hence we adopted the plane stress conditions. The particle spacing is set to $\Delta X = 2$ mm, horizion radius is chosen as $\delta = 3.015\Delta X$ and the elastic modulus is chosen as $E = 0.01$ GPa. The bond constant is chosen as $D = 1200\ k_b\theta$, number of chains per peridynamic bond is $\overline{n} = 400$, and the critical bond stretch is set to $\lambda_{critical} = 1.1\sqrt{n}$. We stretch the plate parallel to the faces of the cracks,

with a constant strain rate of $\dot{\epsilon} = 5 \times 10^{-5}$ 1/s. The boundary conditions are modeled by prescribing constant velocities to the material points in the boundary layers, as depicted in Figs. 2.12(b) and (c).

As shown in Figs. 2.12 (b) and (c), there are two pre-notch configurations: (1) a finite width precrack or continuous notch, and (2) an array of voids. Because void growth is one of the main mechanisms for the ductile fracture of metallic materials [25], we are curious if a similar mechanism would exist in polymeric materials.

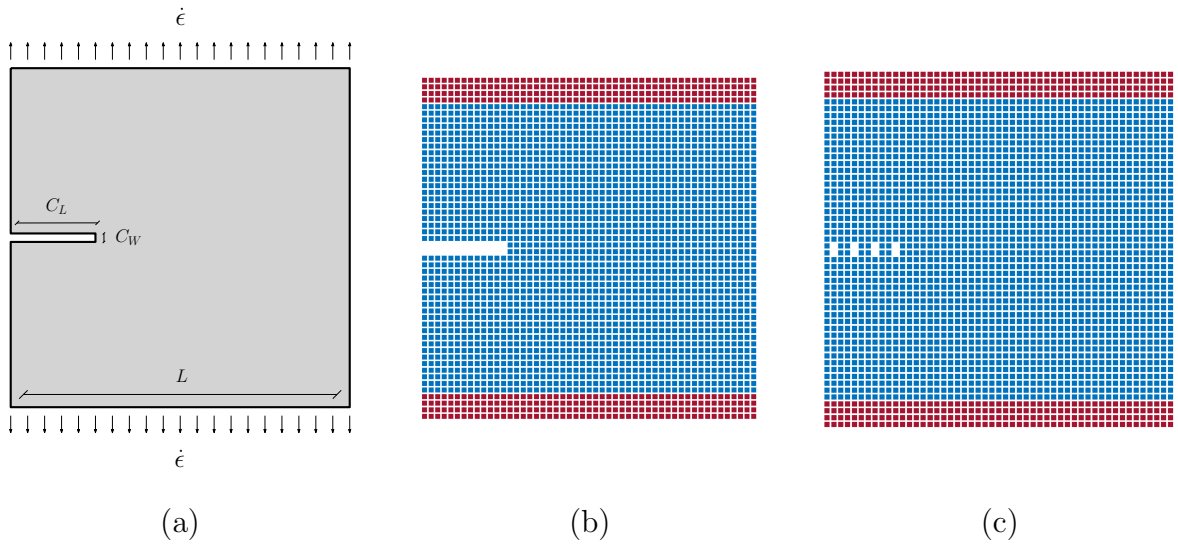

Figure 2.12: (a) The Mode-I crack opening with constant strain rate, (b) Peridynamic model of the problem; displacement boundary conditions enforced to red particles, (c) Alternative configuration with the voids instead of the pre-crack

Simulations were carried out until the complete failure of the specimens, and the resulting fracture patterns are shown in Fig. 2.13 for the precrack and void configurations. For the first specimen, the stress concentration around the crack tip is followed by a brittle crack propagation that ultimately leads to the total rupture of the medium. In the second sample, coalescence of the voids is first observed, which is then followed by crack propagation and the final rupture of the specimen.

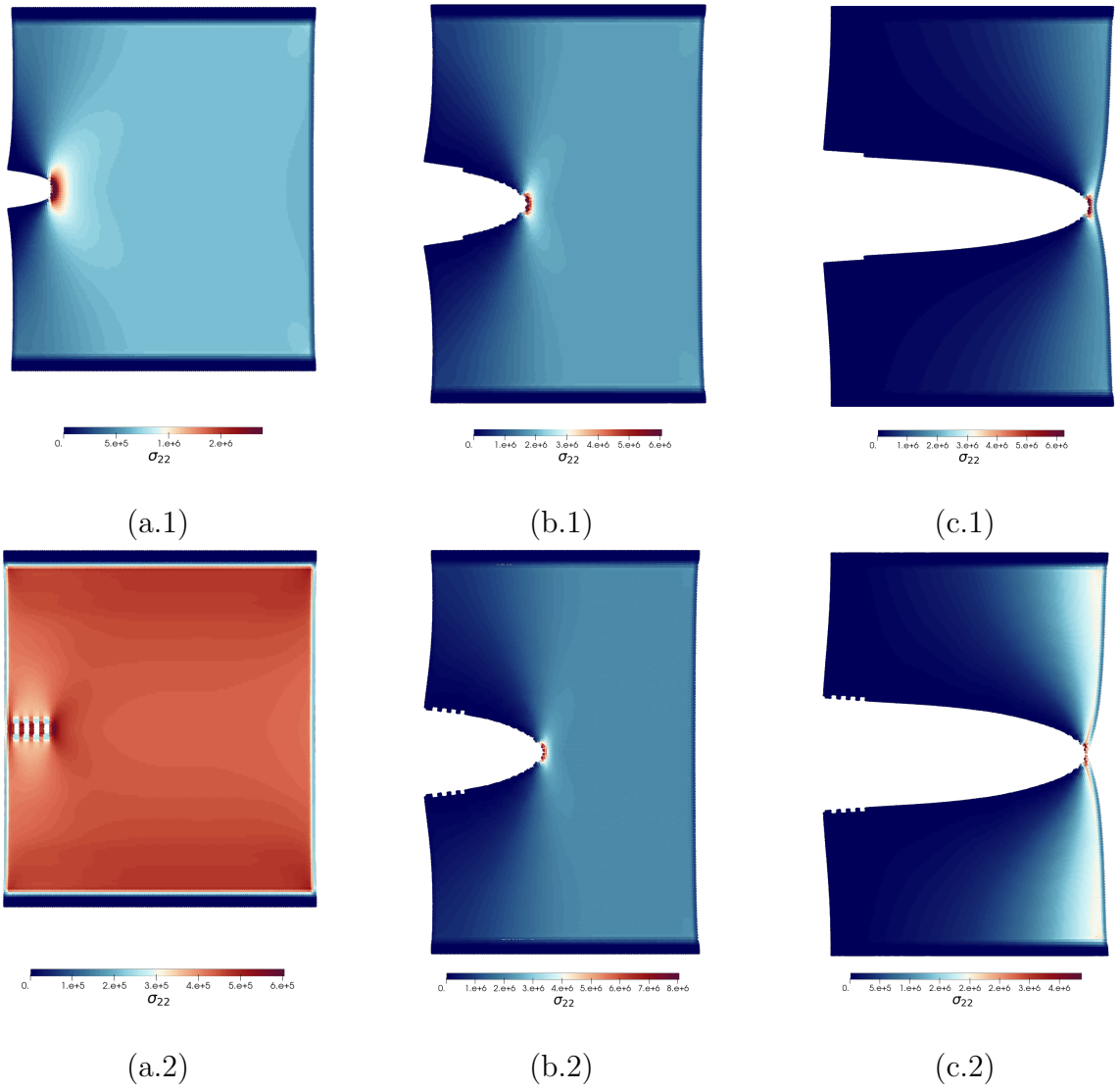

Figure 2.13: The Cauchy stress (σ_{22}) distribution during different stages of the deformation for the Mode-I opening. (a) Initial stress concentration around the crack/voids. (b) Propagation of the crack towards the right edge (c) Configuration right before complete rupture.

Load displacement curves are obtained for both specimens and plotted in Fig. 2.14. Clearly, the sample with the initial voids dissipates more energy before the fracture, resulting in more ductile behavior. The results are in agreement with the high-energy fracture mechanism that the void coalescence process yields. It should be noted that the void-notch configuration also results in a higher ultimate breaking stress for polymeric materials.

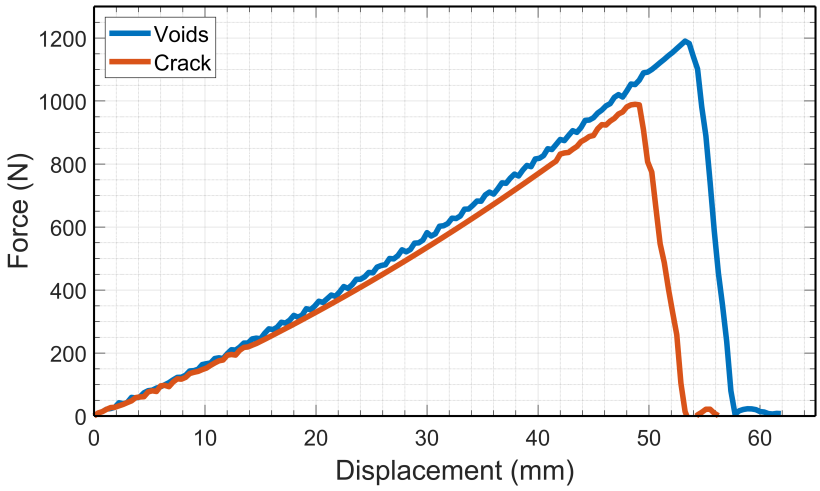

Figure 2.14: Load-displacement curves for the Mode-1 fracture simulations. Comparison between the pre-crack and voids configurations.

Square Plate: Mode-II Crack Opening

In this subsection, we present the results of the numerical simulation of a thin square plate with an initial crack under the simple shear loading condition. The geometry and boundary conditions of the specimen are depicted in Fig. 2.15. The bottom boundary is fixed, and the top left side of the specimen is restricted in the vertical direction. The length of the plate is set to $L = 400$ mm and has a thickness of $t = 2$ mm. The particle spacing is set to $\Delta X = 2$ mm and the horizon radius is chosen as $\delta = 3.015\Delta X$. The initial crack is located in the middle section and has dimensions $C_L = 200$ mm and $C_W = 4$ mm. The elastic modulus is chosen as $E = 0.1$ GPa, the bond constant is $D = 1200k\theta$, the number of links per bond is $\overline{n} = 200$ and the critical stretch is set to $\lambda_{critical} = 1.1\sqrt{n}$.

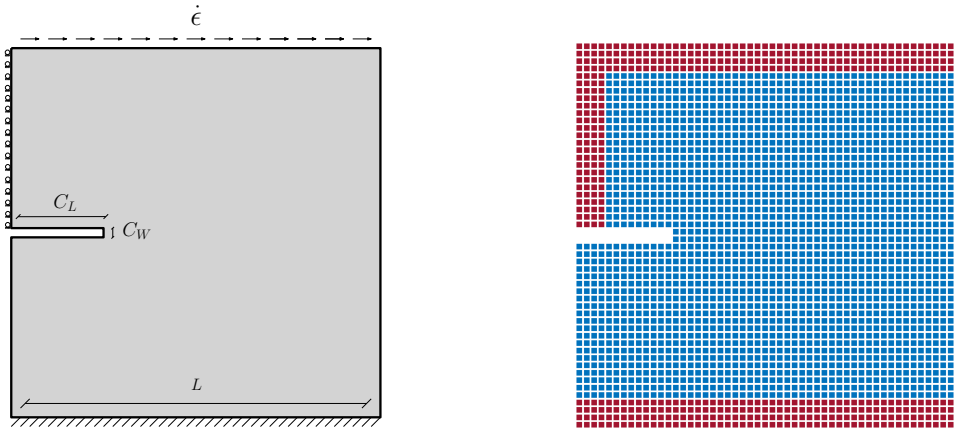

(a) (b)

Figure 2.15: (a) Square plate with an initial crack, (b) Peridynamic model of the problem; displacement boundary conditions enforced to red particles.

The upper surface of the specimen is pulled with a constant strain rate of $\dot{\epsilon} = 10^{-4}$ / s until a complete separation is observed. The contours of the shear component of the Cauchy stress (σ_{12}) are plotted at different stages of the simulation in Fig. 2.16.

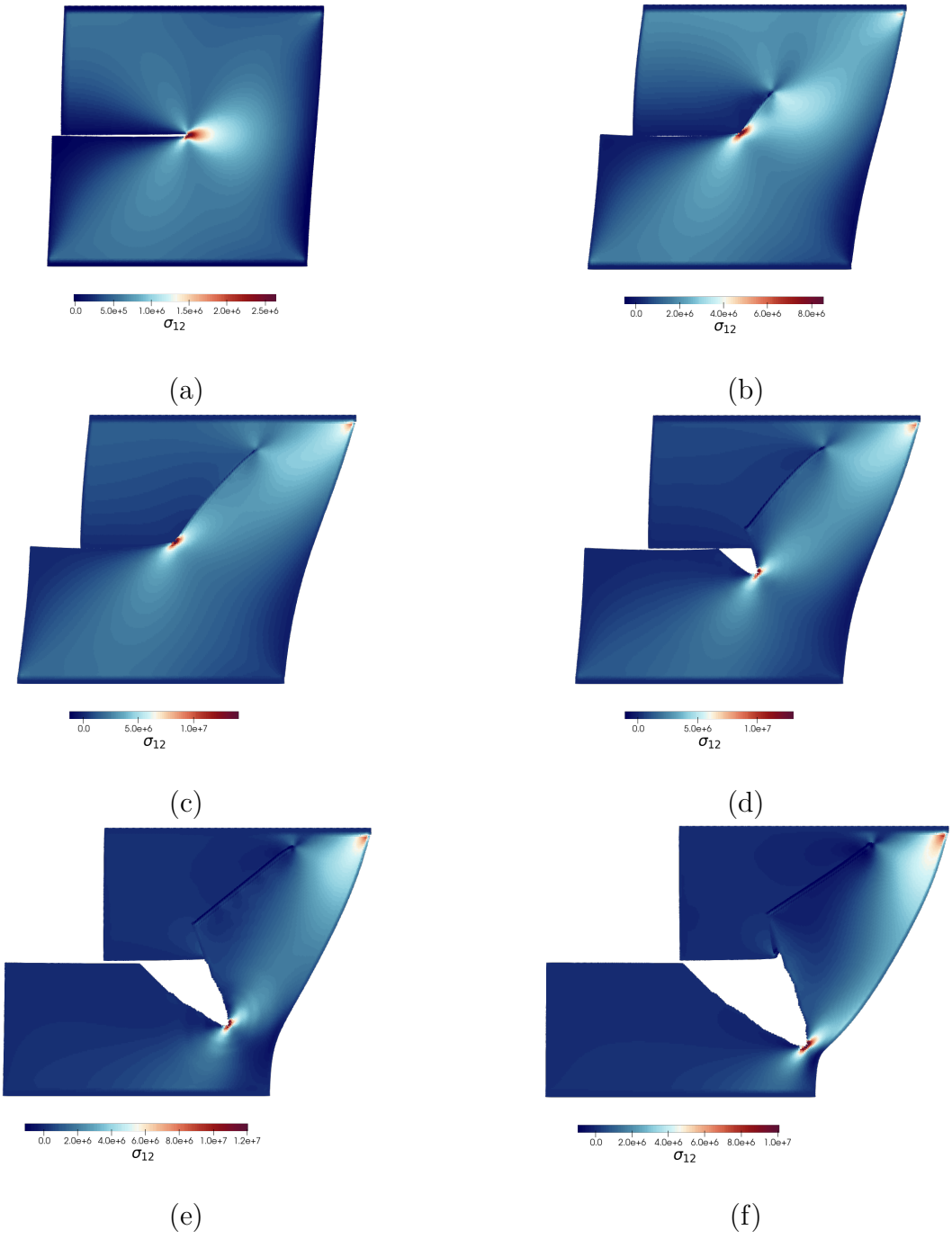

Figure 2.16: Shear stress (σ_{12}) distribution during different stages of the deformation for the shear specimen. (a) Initial stress concentration. (b) Formation of the compression crack. (c) Compression crack propagation towards the top surface. (d) Formation of the tensile crack. (e) Tensile Crack Propagation. (f) Configuration right before tensile crack reaches the right edge.

In Figs. 2.16 (a), (b), and (c), one may observe that a compression crack forms at the crack tip when the stretch of the polymer network reaches a critical value and it moves towards the upper edge of the plate. This is followed by the formation of a tensile or mixed mode crack in the lower part of the specimen and the complete rupture of the specimen.

Moreover, in Figs.2.16 (d), (e) and (f), we observed for the first time in peridynamics simulations that an overlap folding of the compression fracture surfaces as a secondary crack, which is a real crack formation during compression when a wing crack grows during shear loading [11]. It has been noted in various publications that the secondary crack may occur for polymeric materials under shear, e.g. [43, 54, 65].

However, it is very difficult to capture them in numerical simulations. There have been reports in the literature that some phase field fracture models can simulate secondary crack growth in a simple shear test, e.g. [2]. To the best of the authors' knowledge, this has not been captured by any peridynamics modeling, which requires the method to be capable of capturing the bifurcation solution of a large deformation problem. Clearly, this simulation example demonstrated the robustness, prowess, and versatility of the proposed peridynamic polymer model. One caveat to the current model is the lack of a contact formulation, and hence we are limited to simulating fracture under the plane stress condition for now. In order for us to simulate general 3D or plane strain problems, a contact formulation may be necessary.

Three-dimensional cylindrical bar

To fully evaluate the performance of the proposed bond-based peridynamics polymeric model, we also performed a fully three-dimensional (3D) numerical simulation. The example is a cylindrical bar with a thin cross section in the middle, which is loaded in the axial direction. We have prepared three samples with length $L = 100$ mm, regular cross section radius $R = 40$ mm, and the thin section varies in radius as $r = \{16, 20, 30\}$ mm, which is illustrated in Fig. 2.17. Particle spacing is chosen as $\Delta X = 2$ mm and the horizon size is set to $\delta = 3.015\Delta X$. Resulting peridynamic model is illustrated in Fig. 2.17(b)

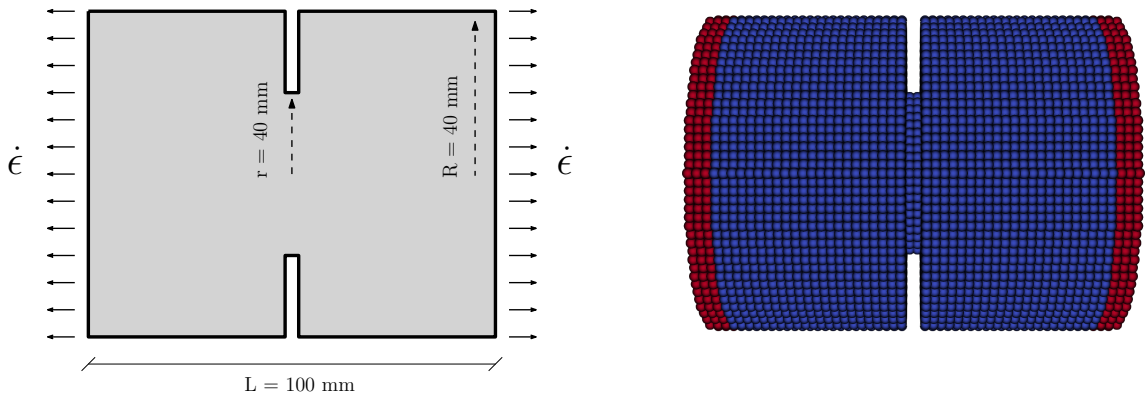

(a) (b)

Figure 2.17: (a) 3D cylindrical bar with a thin cross section in the middle; geometric description (b) Peridynamic model of the problem; displacement boundary conditions enforced to red particles.

The elastic constants are chosen as $E = 0.01$ GPa, $\nu = 1/4$. The bond constant is chosen as $D = 1200\ k_b\theta$, number of chains per peridynamic bond is $\overline{n} = 100$ and the critical bond stretch is set to $\lambda_{critical} = 1.1\sqrt{n}$. By imposing displacement boundary conditions, we load the samples in the axial direction with a constant strain rate of $\dot{\epsilon} = 10^{-3}$ 1/s until a total rupture occurs.

The resulting crack pattern along with the contours of the axial stress component σ_{33} is visualized in Fig. 2.18 for the sample with mid-section radius $r = 20$ mm. From the snapshots of the fracture process, one clearly sees the thinning of the middle section as the circumference crack progresses and the back contract of the polymer material once the cylinder is severed into two halves, which finally recovers the broken smooth fracture cross section.

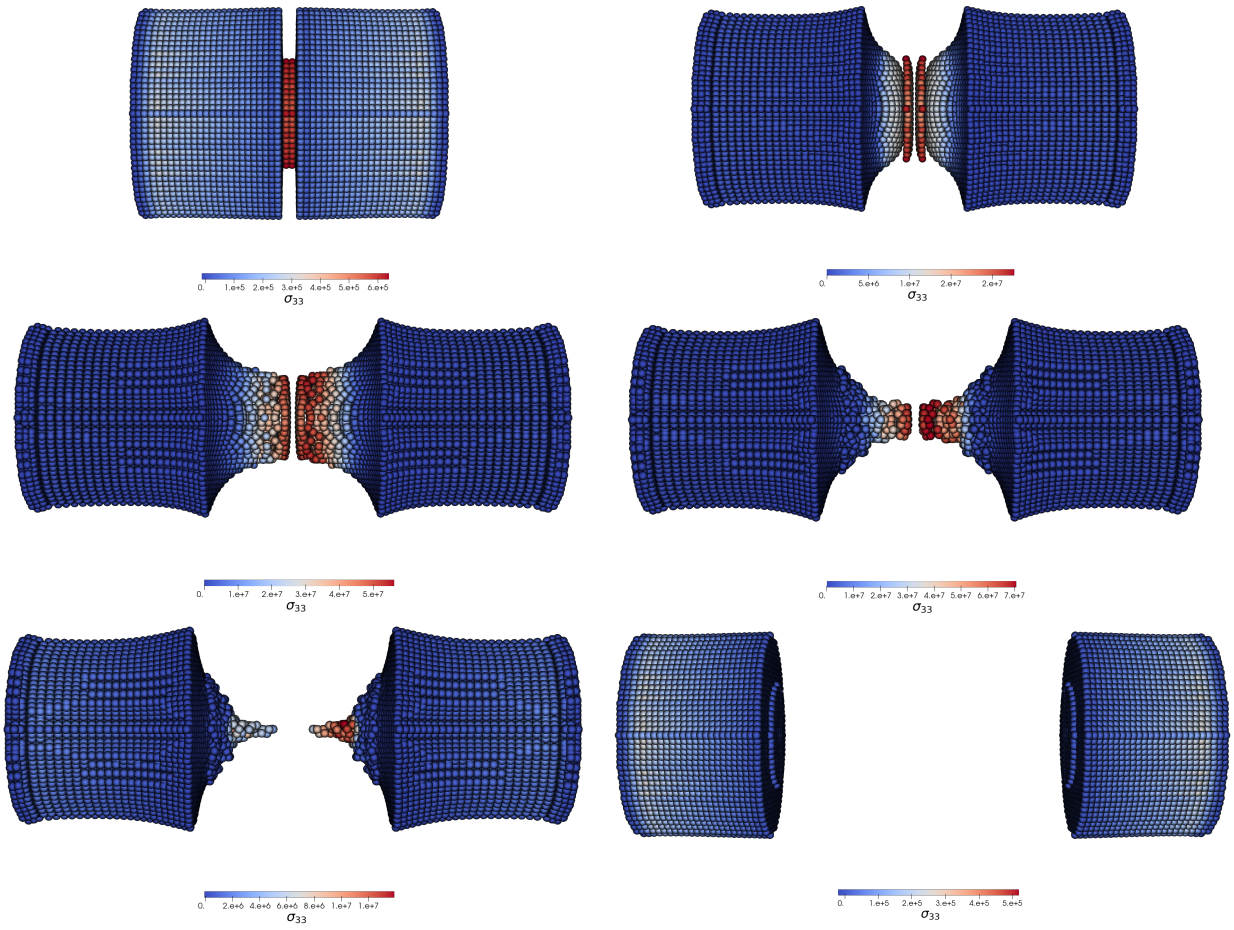

Figure 2.18: Cylindrical bar at different stages of deformation. Contours indicate the axial stress (σ_{33}) distribution.

We obtained the load versus displacement relations by recording the axial force at the top section and total stretch of the cylinder throughout the simulation, and the resulting force-displacement relations for all three specimens are plotted in Fig. 2.19. As shown in Fig. 17, the maximum breaking force increases with the increase of the radius of the middle thin section, and so does the fracture energy.

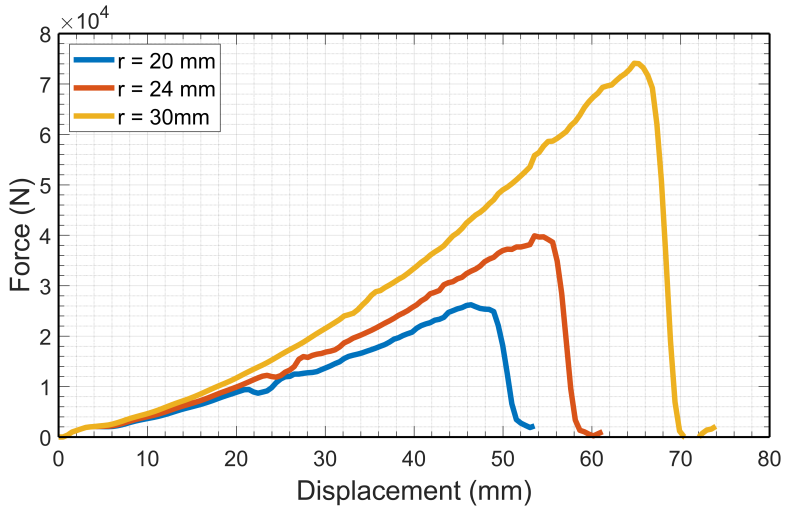

Figure 2.19: Load-displacement curves for the 3D cylindrical bar with varying middle section radius.

2.5 Concluding Remarks

In this work, we proposed and developed a novel nonlocal bond-based peridynamics model for general polymeric materials. The main novelty of the work is the formulation of the mesoscale peridynamic potential that incorporates the conventional Arruda-Boyce model into the bond-based peridynamics framework, which results in a nonlocal rubber continuum mechanics model under finite deformation.

We demonstrated through a series of numerical examples that the proposed polymeric material model works well and compares well with the experimental and numerical data obtained through previous studies. Moreover, we have shown that the unique advantage of the proposed method is its ability to capture and predict the fracture and damage processes in polymeric materials with simplicity and accuracy, under various loading modes and geometric configurations. Our model is a valuable addition to the field of polymer mechanics and has the potential to impact future advancements in the design and optimization of polymeric materials.

The present model may be extended to take into account the shear deformation of polymer chain networks by following the non-ordinary bond-based framework demonstrated by Han et al. [27], which may finally provide a nonlocal inelastic bond-based peridynamics model for general polymeric materials that is much needed in many engineering applications.

Chapter 3

A Deep Learning Based Constitutive Modeling for Crystalline Polymers

3.1 Introduction

Material modeling of 3D printed material products has been a great challenge for additive manufacturing and other advanced manufacturing technologies. In additive manufacturing, the product is built on a material point upon a material point; thus, the resultant properties are highly dependent on the printing process both spatially and temporally at the localized regions. A microstructurally informed and robust mechanical model is highly anticipated, as it would help to overcome the challenges with manufacturing process, product design, and material selection.

One of the promising approaches is the multiscale modeling of 3D printed materials [57, 83, 38], which has the ability to extract bottom-up material information to assess the macroscale properties of a product that is additively manufactured. However, the cost of multiscale modeling may vary, especially when it is involved with molecular-scale simulations. Traditionally, in multiscale modeling of crystalline materials, this is overcome by using a technique called the Cauchy-Born rule [97, 9], which is an approximation of molecular dynamics by using simplified molecular statics or by using phase field crystal method for polycrystalline metals [109]. However, for semicrystalline or amorphous materials, due to the lack of a definite crystal structure, full-scale molecular dynamics must be utilized, which will significantly increase the cost of the multiscale simulation. This is because the macroscale finite element method would require a molecular-level stress-strain relation at each quadrature point for an arbitrarily given strain, and it is almost impossible to conduct concurrent molecular dynamics simulations unless one has abundant computational resources.

The task at hand is to simulate the molecular-level stress-strain relation under arbitrary strain and temperature with good accuracy, efficiency, and low cost. To solve this problem, in the present work, we adopted a machine learning approach by developing an artificial neural network (ANN) that is trained on a molecular dynamics (MD) data set, which can

predict the molecular-level mechanical material properties of polymeric materials.

Current efforts in machine learning-driven material property predictions involve a variety of approaches. One common approach is to use features based on the material composition to obtain structure and electronic properties, such as predicting the band gap of semiconductor materials using convolutional neural networks [80] and predicting adsorption energies of high-entropy alloys through deep neural networks [79]. In a recent study, standard feed-forward neural networks are used with EAM-based MD simulations to model crystal plasticity in a multiscale framework [9].

Additive manufacturing can use a wide range of materials, such as synthetic polymers, metal alloys [99], and biomaterials. Industrial applications range from the automotive industry to tissue engineering [102], and understanding the mechanical properties of such materials is still an open topic. Our focus in this work is on polymers, for which new applications emerge everyday, such as polyester membranes for biomedical applications [101] and geopolymers used in the construction industry [42].

Polymeric materials have three different microstructural forms: crystal, amorphous, and semicrystalline. As a starting point, we first develop an ANN to predict the mechanical response of the anisotropic crystalline forms of polymers. The approach we presented can be extended to include amorphous phases and will eventually be incorporated into the constitutive relations of a multiscale finite element method for semicrystalline polymers. One of the polymeric materials widely used in additive manufacturing is Polyamide12 (PA12), also known as Nylon12, which is a synthetic polymer that is used in many industrial applications, such as automotive parts, aerospace applications and medical components. An automotive part manufactured using the multi-jet fusion process is shown in Fig. 3.1.

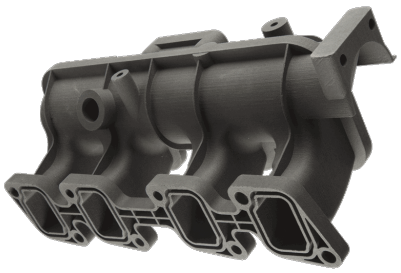

Figure 3.1: 3D printed PA12 auto part via HP multi-jet fusion (Courtesy of Ford Motor Company).

PA12 has the chemical formula $[\text{-}(CH_2)_{11}C(O)NH\text{-}]_n$ as visualized in Fig. 3.2. In recent years, many 3D printed PA12 products have been fabricated, and they have shown some outstanding material properties. Additively manufactured PA12 is a semicrystalline material, in which the microstructure has a sandwich-like structure of alternating regions of crystal and amorphous zones.

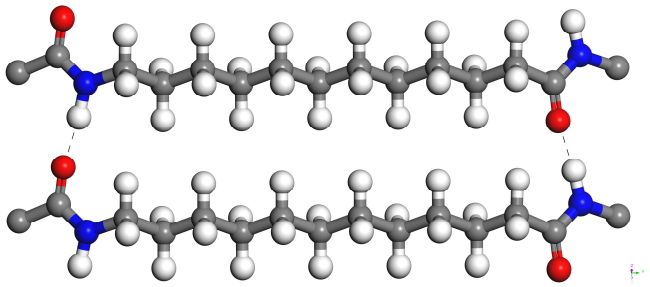

Figure 3.2: Polyamide12 molecules. Gray, white, blue and red spheres represent carbon, hydrogen, nitrogen and oxygen atoms respectively. Dashed lines indicate the H bonds.

Its structural characterization has been extensively studied since the 1970s with x-ray diffraction (XRD) experiments [19, 36] and with nuclear magnetic resonance (NMR) spectroscopy [63], which revealed that PA12 displays polymorphism and can have crystal phases α, α', γ and γ'. The most abundant phase is the γ form, which results from slow cooling at atmospheric pressure, whereas the other phases require specific conditions such as rapid quenching and/or high-pressure treatment. For the purposes of our study, we focus on the γ crystal form.

3.2 Molecular Dynamics Simulations

In this section, we describe the details of molecular dynamics simulations, such as the preparation of initial configurations, the force field selection, and simulation procedures, and we conduct a preliminary study.

Molecular dynamics (MD) is a simulation technique for analyzing the atomistic trajectories. The main idea is to use the inter-atomic potentials (force fields) to describe the interactions between each particle and then numerically solve the Newton's equation of motion (3.1). MD simulations prove to be useful for scientific research in many fields; drug discoveries in the pharmaceutical industry, analyzing organic molecules in biophysics, designing nano-materials in materials science and understanding the constitutive behavior in civil and mechanical engineering.

$$m_i \frac{\partial r_i}{\partial t} = F_i = -\frac{\partial V}{\partial r_i} \qquad \text{for } i = 1, 2, .., N \tag{3.1}$$

where r_i are the coordinates of each atom and V is the empirical interatomic potential and N is the number of atoms in the system.

Although being a very powerful tool, MD simulations are limited to small time and space scales, due to their high computational expense. A classical way of doing MD simulations is to use periodic boundary conditions, which replicates the unit cell in three dimensions, and it allows us to simulate the macroscale behavior of the material. MD simulations are based

on statistical ensembles, where one assumes some combination of number of particles (N), volume (V), macro scale temperature (T), total energy (E), and macroscale pressure (P) of the system is constant. Most common statistical ensembles used in classical MD simulations are NVE, NVT and NPT ensembles, which can simulate different conditions for the system.

System Setup

We start by constructing the unit cell of the γ form PA12 crystal. The γ phase has a pseudo-hexagonal monoclinic structure with the lattice parameters summarized in Table 3.1 [19, 36]. Using the atomistic coordinates and the lattice parameters from the experimental literature [36], the unit cell of the γ phase is constructed. This monoclinic structure contains four PA12 chains and is visualized in Fig. 3.3. Note that the dashed lines indicate hydrogen bonds and that the unit cell is periodic in all directions.

Lattice Parameters	
a	4.79 Å
b	31.90 Å
c	9.58 Å
β	120°
Space Group	P21/C

Table 3.1: Lattice Parameters for γ form PA12 crystal

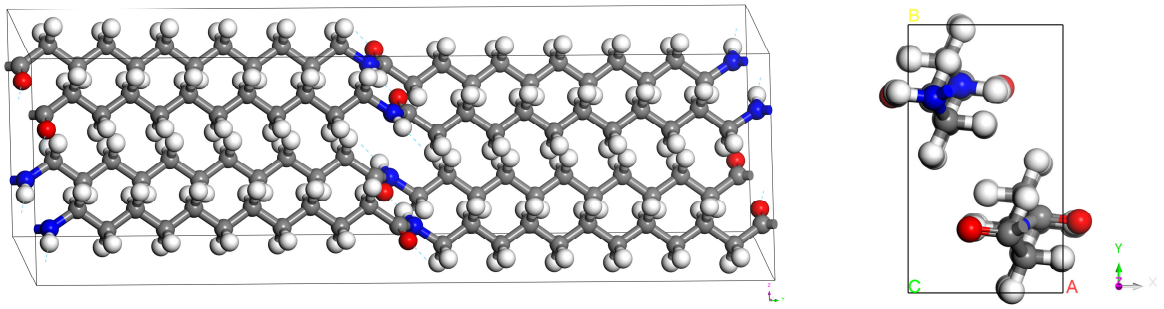

(a) (b)

Figure 3.3: Unit cell of the γ form PA12: (a) Monoclinic cell (b) Orthogonal transformation.

Polymer chains are aligned with the y-axis, and the unit cell represents a perfect crystalline system with infinite chain length and no defects. MD simulations of triclinic (non-orthogonal) boxes are computationally expensive, due to the irregular partitioning of the

processor subdomain. To improve efficiency, we transform the simulation box into an orthogonal cell with chains aligned with the z-axis, which is depicted in Fig. 3.3. The unit cell is then duplicated by $(8 \times 4 \times 2)$ in the (x, y, z) directions, respectively, to create a supercell for MD simulations. The resulting model, which consists of around 9,500 atoms, has dimensions [38.3Å $\times$ 33.2Å $\times$ 63.8Å], is visualized in Fig. 3.4.

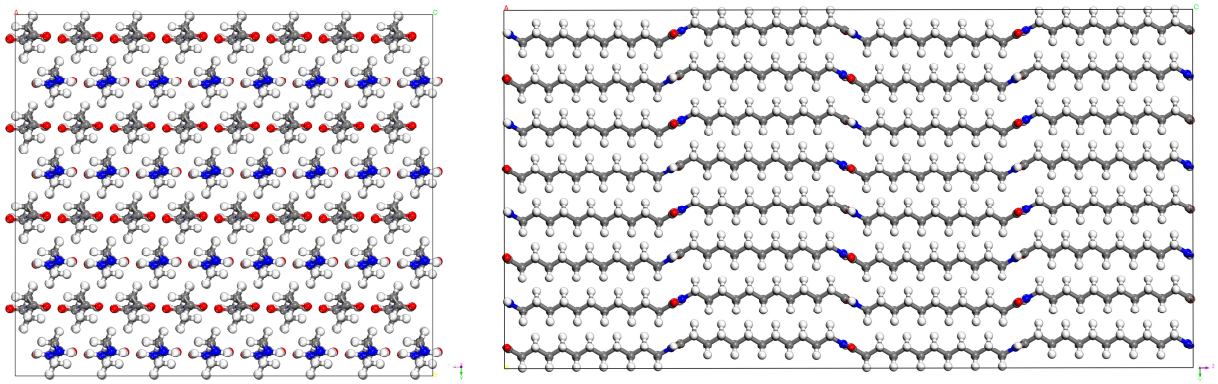

(a) (b)

Figure 3.4: Supercell of perfect PA12 crystals (a) View from x-y plane (b) View from y-z plane.

Force Field Selection

Force fields represent the interactions between atoms and molecules using a set of equations. In classical forms, force fields consist of empirical potentials that describe bonded interactions (primary bonds, bond angles, and dihedrals) and non-bonded interactions (van der Waals and electostatic). Choosing a suitable force field for the system under consideration is a crucial part of molecular dynamics simulations.

Several empirical force fields have been used in the simulation of polyamides; some popular examples being OPLS, CVFF, COMPASS, and DREIDING [47]. However, these potentials are typically unable to model chemical reactions and cannot account for bond dissociation. Hence, they are not the ideal choice for investigating the mechanical response of the system in the context of fracture mechanics and rupture of polymer crystals, which may involve the chain scission process [76, 6].

Reactive force fields, on the other hand, have been developed to simulate complex chemical reactions and have been used successfully in deformation simulations that involve bond cleavage. Once such a force field is ReaxFF, originally developed by van Duin [98], which utilizes the so-called bond order formalism to describe chemical bonding. ReaxFF requires no topology information, and it is easy to construct initial MD configurations since only the atomistic coordinates are needed. ReaxFF specially treats weak hydrogen bonds with an

explicit energy term in the functional, which plays an important role in polymer systems. The current implementation in LAMMPS utilizes the functional described in [16].

ReaxFF is parameterized for a wide range of materials through quantum mechanical calculations [82] and has also been used in the simulation of polyamide crystals before [104]. For our polymer system, we tested three such parameterizations [46, 64, 107]. The test process involved relaxing the initial structure in the NPT ensemble and comparing the resultant lattice parameters with the experimental values. Among these, the ReaxFF parameterization by Mattson [64] yielded the best result; therefore, it was chosen as the force field for this study.

Simulation Details

Molecular dynamics simulations are performed using the Large-Scale Atomic/Molecular Massively Parallel Simulator (LAMMPS) [92]. The simulations are run on Berkeley's high-performance computing cluster Savio using a $[4 \times 2 \times 4]$ CPU grid. MD time steps are chosen as 0.5 fs. Nosé-Hoover thermostat and barostat [21] are used to control temperature and pressure, respectively, with damping parameters chosen as 50 fs and 500 fs. Damping parameters were chosen according to the LAMMPS documentation, which recommends temperature and pressure damping to be 100 and 1000 times the time step, respectively.

The initial structure is relaxed in the constant pressure and temperature (NPT) ensemble at 300 K and 1 atm, where the pressure is controlled independently in all directions. We observed that an NPT simulation for 50 ps was sufficient to reach equilibrium, as the lattice parameters stabilized adequately at this point.

As a preliminary study and to investigate in detail the anisotropic mechanical response of PA12 crystals, we constructed a larger MD cell with 38,000 atoms. After relaxation under ambient conditions, we deform the system in different directions under uniaxial tension. Uniaxial deformation is imposed by stretching the unit cell in one direction at a constant strain rate and relaxing the other two dimensions with the NPT ensemble at 1 atm. For this part of the study, we used slower strain rates and deformed the cell quasi-statically in a step-by-step fashion as described in [105]. In this process, the MD cell is deformed to 1% of its final stretch, relaxed in the NVT ensemble, and the stress is sampled and averaged over 5 ps intervals. These steps are repeated until rupture of the polymer chains is observed and the resulting stress-strain behaviors are shown in Fig. 3.5 for each direction.

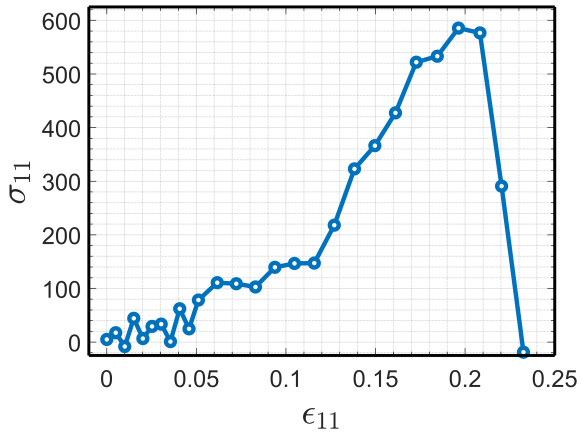

(a) x-direction

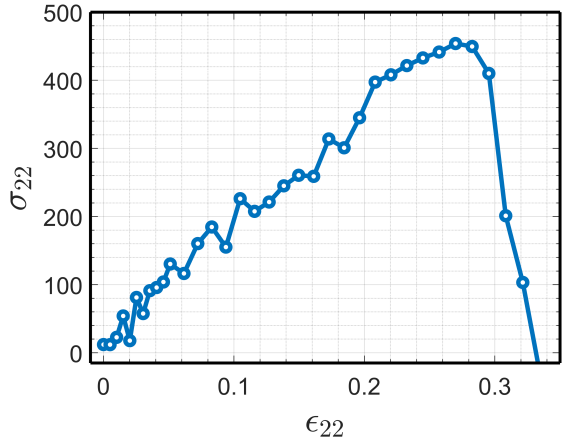

(b) y-direction

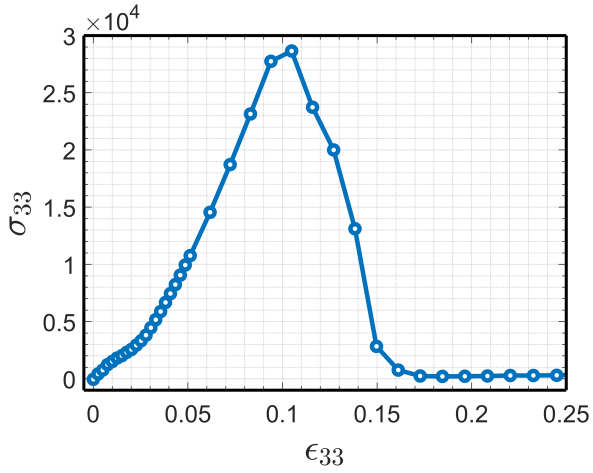

(c) z-direction

Figure 3.5: Stress (MPa) versus Strain (engineering) behavior of PA12 in uniaxial tension.

In Fig. 3.5, we observe that the system is highly anisotropic; crystal is significantly more stiff in the z-direction, which is the direction of polymer chain alignment, and it is more ductile in the other two directions. Interestingly, for the x-direction, Fig. 3.5 (a) , there was a notable increase in the elastic modulus once the strain reaches around 12%. We explored this phenomenon to comprehend whether it involves a mechanically induced phase transformation by deforming the original monoclinic crystal supercell in the x-direction. The resulting atomistic configurations before and after the change in elastic modulus are visualized in Fig. 3.6, in which we clearly observe a change in the microstructural configurations.

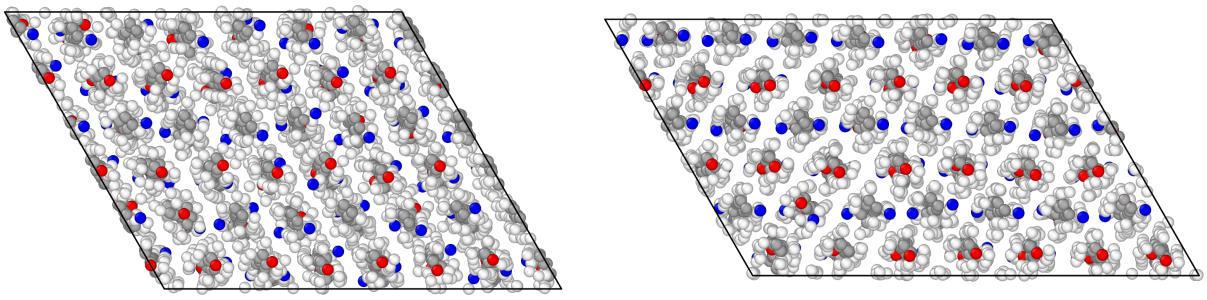

(a) Before the elastic modulus change (b) After the elastic modulus change

Figure 3.6: Snapshots of the atomistic configurations during deformation in the x-direction.

Upon additional analysis, we understood that the process is completely reversible and the effect disappears once the MD cell is unloaded to its original state. Further investigation may be required to draw a meaningful conclusion about the phenomenon.

3.3 Deep Neural Networks for Constitutive Relations

In this section, we present a data-driven approach to model the hyperelastic constitutive law of crystalline PA12, to be used in multiscale mechanics simulations. Our task is to find the mapping between the deformation state and the resulting material response, using the data obtained from the molecular dynamics simulations on an artificial neural network (ANN). We discuss data collection, model selection, training phase, and predictions in detail.

Data Collection

In order to generate the data set to train the learning model, we performed MD simulations by deforming the PA12 supercell in different directions with varying strain rates. For the purposes of this study, we limit our attention to uniaxial and biaxial tensile deformations, although the presented methodology should be applicable to any deformation mode. Using the findings of the preliminary study, Fig. 3.5, we determined the final stretch limits

of the simulation box necessary in each direction and corresponding strain rate ranges, as summarized in Table 3.2. In all simulations, the supercell is deformed for 10,000 steps with a rate chosen from the prescribed ranges depending on the loading direction. Specifically, we chose 15 evenly spaced values from the ranges in Table 3.2 and took their combinations to obtain uniaxial and biaxial loading cases, resulting in 720 different MD simulations, each having different final stretches and strain rates. Note that the ultimate strains would only be reached at simulations which utilize the maximum strain rates.

	Deformation Direction		
	x	y	z
Ultimate Strain	0.5	0.6	0.15
Strain Rate ($10^{-6}/fs$)	[3.3, 50]	[4, 60]	[1, 15]

Table 3.2: Ultimate strain and resulting ranges of strain rates for each direction.

Each deformation simulation is run for 5 ps, and the Virial stress and the box dimensions are sampled at 50 fs intervals. Consequently, after running all the 720 simulations, we collected a data set consisting of 72,720 data points. Each data point is 12 dimensional, representing the deformation (6 components) and stress (6 components) states of the PA12 crystal. Note that the process described here involves remarkably high strain rates and short simulation times, since it was not computationally feasible to conduct slower simulations and collect a large data set at the same time.

The original data from MD simulations consist of box dimensions $l = \{l_x, l_y, l_z\}$ which can be used to construct the deformation gradient $\boldsymbol{F}$, and the stress measure we get is the pressure tensor, known as the Virial stress. Virial stress has been shown to be equivalent to continuum Cauchy stress $\boldsymbol{\sigma}$ [88]. In order to adopt the model into the continuum mechanics framework, we need to transform the data set into the tensor quantities utilized in finite deformation. To preserve material objectivity [4, 9], we chose the energetic conjugates right Cauchy-Green tensor $\boldsymbol{C}$ and the second Piola-Kirchhoff (PK2) stress tensor $\boldsymbol{S}$ to represent the deformation state and material response, respectively. Each of these second-order tensors have nine components, but making use of the symmetry and Voigt notation we represent them in the vector form as below.

$$\boldsymbol{C} = [C_{11},\ C_{22},\ C_{33},\ C_{12},\ C_{13},\ C_{23}] \tag{3.2}$$

$$\boldsymbol{S} = [S_{11},\ S_{22},\ S_{33},\ S_{12},\ S_{13},\ S_{23}] \tag{3.3}$$

Using the elementary relations of continuum mechanics, we can obtain the $\boldsymbol{C}$ and $\boldsymbol{S}$ tensors as follows.

$$J = \det \boldsymbol{F} \tag{3.4}$$

$$\boldsymbol{C} = \boldsymbol{F}^T \boldsymbol{F} \tag{3.5}$$

$$\boldsymbol{S} = J \boldsymbol{F}^{-1} \boldsymbol{\sigma} \boldsymbol{F}^{-T} \tag{3.6}$$

Now we can state our goal as finding the map,

$$\Psi : \boldsymbol{C} \rightarrow \boldsymbol{S} \tag{3.7}$$

where Ψ encapsulates the constitutive model that we are going to approximate through supervised learning.

Finally, we normalize our input data set to have a mean of zero and a standard deviation of one, a process known as *standardization*. It is common practice in gradient-based learning methods to standardize the data, which improves the performance of ANNs by helping to solve the convergence issues of the backpropagation algorithm [50, 87]. Standardization can be described as follows.

$$C_{ij}^{std} = \frac{C_{ij} - \hat{\mu}_{ij}}{\hat{\sigma}_{ij}} \quad for \quad i,j = 1,2,3. \tag{3.8}$$

where C_{ij}^{std} are the normalized components of the right Cauchy-Green tensor, $\hat{\mu}_{ij}$ is the sample mean and $\hat{\sigma}_{ij}$ is the sample standard deviation of the respective component.

Model Selection and Training

We adopt a fully connected feedforward network architecture to construct our regression ANN, which may be called a multilayer perceptron (MLP). As shown by the universal approximation theorem, feedforward neural networks can approximate any continuous function, provided that they have at least one hidden layer, have enough neurons, and the activation functions satisfy certain properties [35, 34]. Thus, we believe that an MLP is a suitable choice to approximate the hyperelastic constitutive law. Keras [17] Python interface of the TensorFlow [62] machine learning package is used to select and train our ANN model.

Our task is to find an approximation to the constitutive model defined in (3.7). Formally, we can express the learning problem as follows. Find

$$\mathcal{N}(\boldsymbol{C}, \boldsymbol{w}) = \hat{\boldsymbol{S}} \ , \tag{3.9}$$

such that

$$\boldsymbol{w} = \underset{\boldsymbol{w}}{\operatorname{argmin}} \, \mathcal{L}(\boldsymbol{S}, \hat{\boldsymbol{S}}) \ , \tag{3.10}$$

where $\mathcal{N}$ is encodes the ANN, $\boldsymbol{w}$ are known as the *weights* of each neuron and $\mathcal{L}$ is a *loss function*. The task in supervised learning is to find optimal weights $\boldsymbol{w}$ such that the metric defined in the loss function is minimized.

To select the ANN model parameters known as *hyperparameters*, such as the number of hidden layers, the number of neurons in each layer, the type of activation functions and the learning rate of the gradient descent, we perform hyperparameter optimization. We chose two candidate activation functions that are commonly used in regression, *ReLu* function and its smooth approximate version known as the *Softplus* function.

$$\text{ReLu} \ : \ \sigma(x) = \max(x) \qquad \text{Softplus} \ : \ \sigma(x) = \log(1 + e^x) \tag{3.11}$$

For the loss function, we choose the mean squared error (MSE) of the PK2 stress:

$$\mathcal{L}_{MSE}(\boldsymbol{S}, \hat{\boldsymbol{S}}) = \frac{1}{n} \sum_{i=1}^{n} ||\boldsymbol{S}_i - \hat{\boldsymbol{S}}_i||_2^2 \ , \tag{3.12}$$

where $\boldsymbol{S}$ is the PK2 stress obtain from MD simulations, $\hat{\boldsymbol{S}}$ is the predicted stress from ANN and n is the number of data points.

We tried two methodologies to select the best set of hyperparameters, the HyperBand algorithm [56] and Bayesian Optimization with Gaussian Process [73]. Both algorithms would pick the best parameters from a predefined set, which would give the lowest validation loss. The set of parameters that we make the search is determined by preliminary analysis, where the optimizer of the ANN is chosen as the Adam algorithm [44], which implements a version of the stochastic gradient descent (SGD) method. Accordingly, we chose the following range of parameters to perform hyperparameter tuning.

Hyperparameters			
Hidden Layers	Neurons	Activation Function	Learning Rate
$[2, 5]$	$[32, 256]$	{ReLu, Softplus}	$\{10^{-1}, 10^{-2}, 10^{-3}\}$

Table 3.3: Hyperparameter search grid

We start by partitioning the data into a random 80% - 20% train-test split. Then, we run hyperparameter optimization using Hyperband and Bayesian Optimization methods in the domain described in Table 3.3, leaving aside 20% of the training data to be used to compute validation loss. For all models, the learning rate $\gamma = 10^{-2}$ and the number of hidden layers of four or five gave us the best results. For the rest of the hyperparameters, we investigated the top ten models and chose the ones with the lowest complexity to reduce overfitting. Resulting candidate models are summarized in Table 3.4.

	Hyperband (1)	Bayesian (2)	Hyperband (3)	Bayesian (4)
Input Layer	6	6	6	6
Hidden Layer 1	192 × ReLu	64 × ReLu	160 × ReLu	224 × ReLu
Hidden Layer 2	32 × Softplus	32 × Softplus	64 × Softplus	96 × Softplus
Hidden Layer 3	32 × ReLu	256 × Softplus	32 × ReLu	64 × ReLu
Hidden Layer 4	64 × ReLu	32 × ReLu	128 Softplus	96 × Softplus
Hidden Layer 5	128 × ReLu	64 × ReLu	-	-
Output Layer	6 × Linear	6 ×Linear	6 × Linear	6 ×Linear
Validation Loss	15630	15026	14109	13538

Table 3.4: ANN architectures resulting from Hyperband method and Bayesian Optimization

Prediction Results

The models summarized above are trained on the train data set for 1000 epochs, and predictions are made on the test data to assess our final performance. The resulting train-test history curves, in terms of MSE in PK2 stress (MPa), are presented in Fig. 3.7. We conclude that the ANNs are stable, there is no significant overfitting, and they perform well against the test data set. The best model appears to be ANN-4, the rightmost column in Table 3.4, and its architecture is schematically visualized in Fig. 3.8.

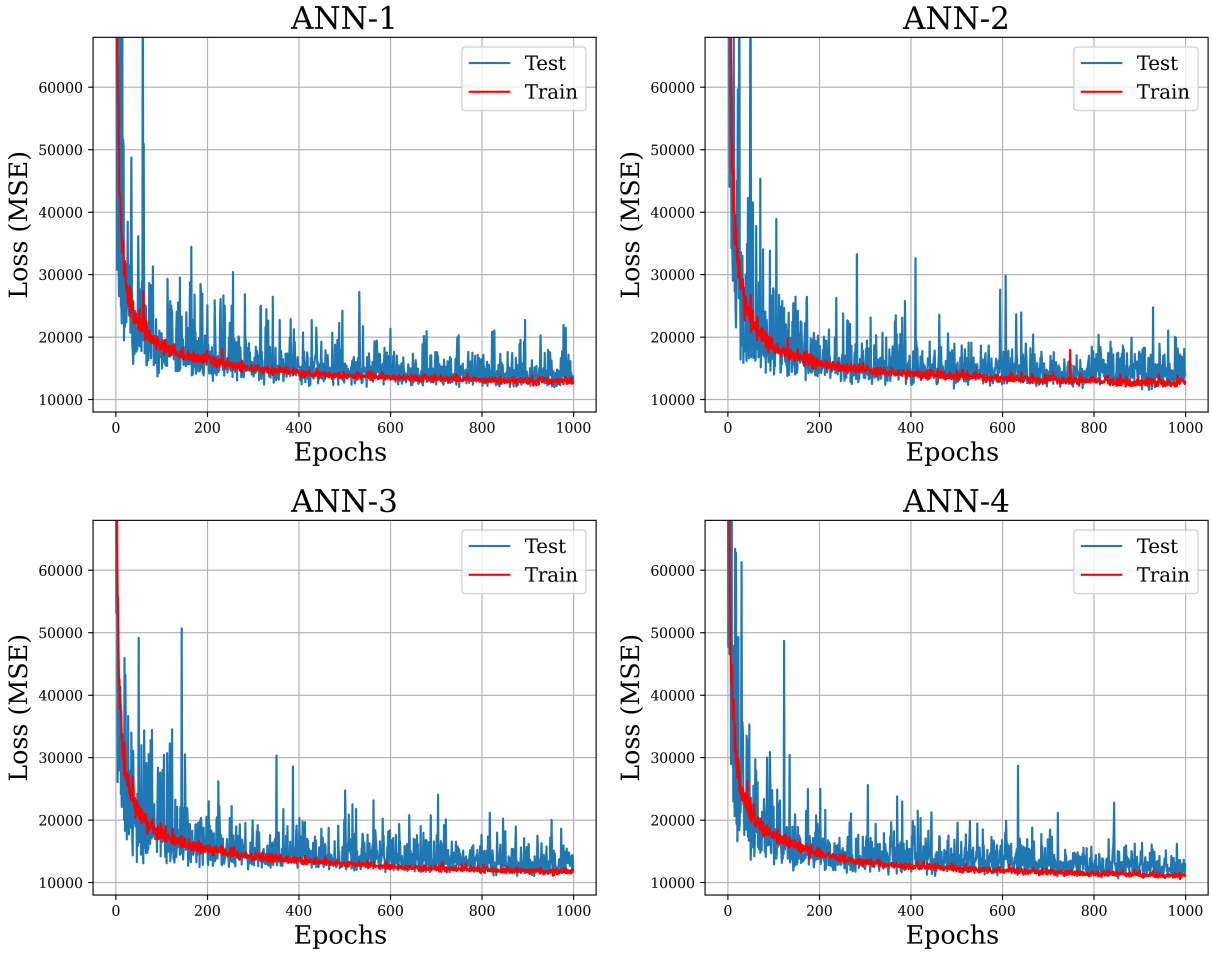

Figure 3.7: Learning curves of the ANNS: Training and test loss (MPa) during training phase.

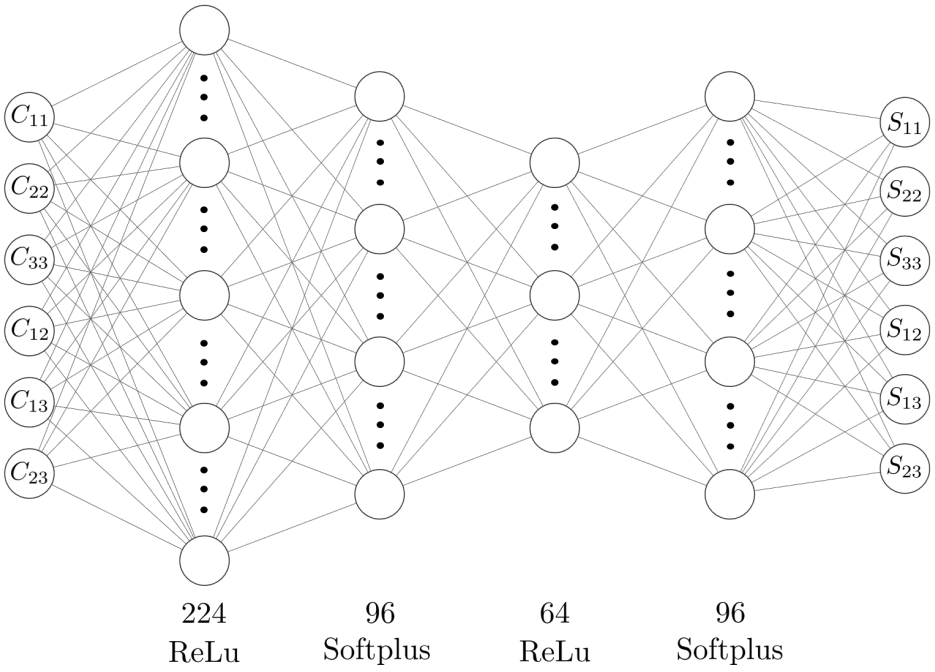

Figure 3.8: ANN-4 schematic representation [53].

We tested ANN-4 against a new set of uniaxial tension MD simulations to observe the performance of our models against the variance in the strain rate. Two of the simulations utilized strain rates $\dot{\epsilon}_1 = 5 \times 10^{-6}/fs$ and $\dot{\epsilon}_2 = 10 \times 10^{-6}/fs$, which are within the training interval defined in Table 3.7. Predictions from ANN-4 is compared with the MD results and the resultant C_{33} versus S_{33} (MPa) relations are shown in Fig. 3.9. The predictions in the elastic range and the ultimate strength are in great agreement with the MD findings, demonstrating the predictive power of the ML approach.

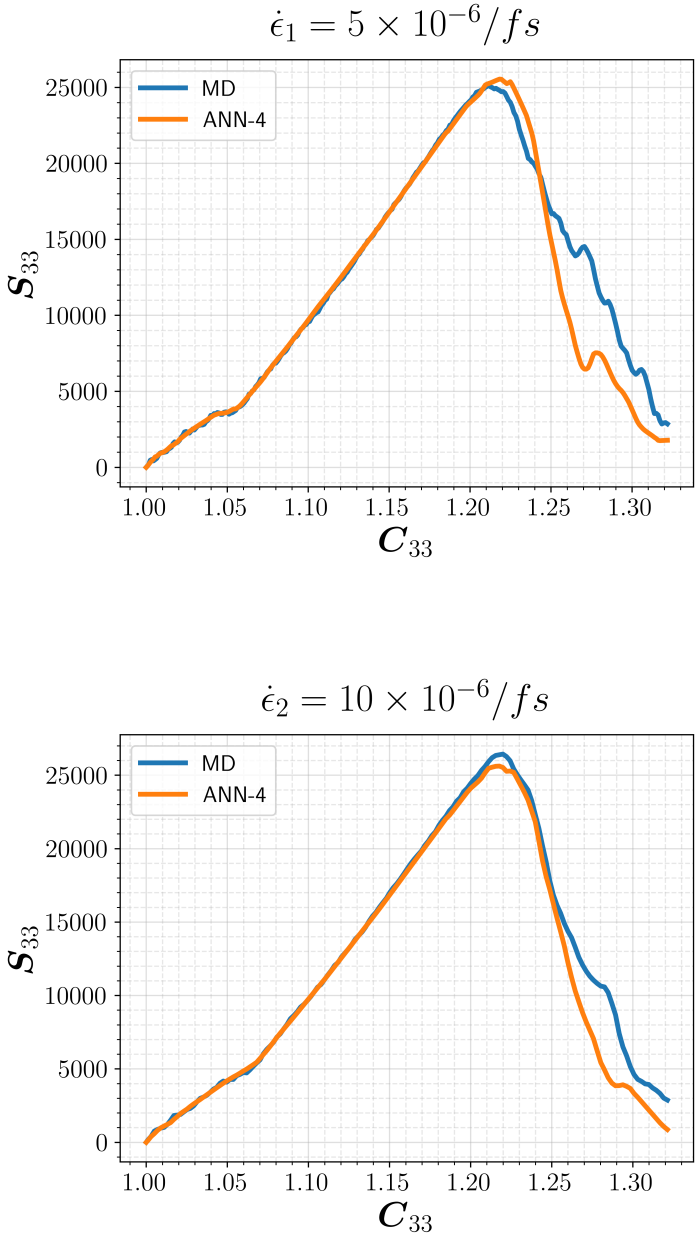

Figure 3.9: Predictions of ANN-4 for uniaxial tension in z-direction for a new set of simulations. The strain rates are contained in the training range.

We consider two additional MD simulations that employed strain rates lying beyond the training range, encompassing both extremes. These strain rates are defined as $\dot{\epsilon}_3 = 0.5 \times 10^{-6}/fs$ (slower) and $\dot{\epsilon}_4 = 30 \times 10^{-6}/fs$ (faster). The corresponding results are shown in Fig. 3.10, together with the MD results, for comparison. Although the slower rate led to a slightly higher ultimate strength, remarkable agreement is observed within the elastic range.

Here, the ANN effectively captured intricate aspects of the loading path. The findings clearly demonstrate the capacity of the model for generalization and robustness across various strain rates, which makes it a promising candidate for effectively describing the constitutive laws of crystalline polymers to be used in large-deformation FEM simulations.

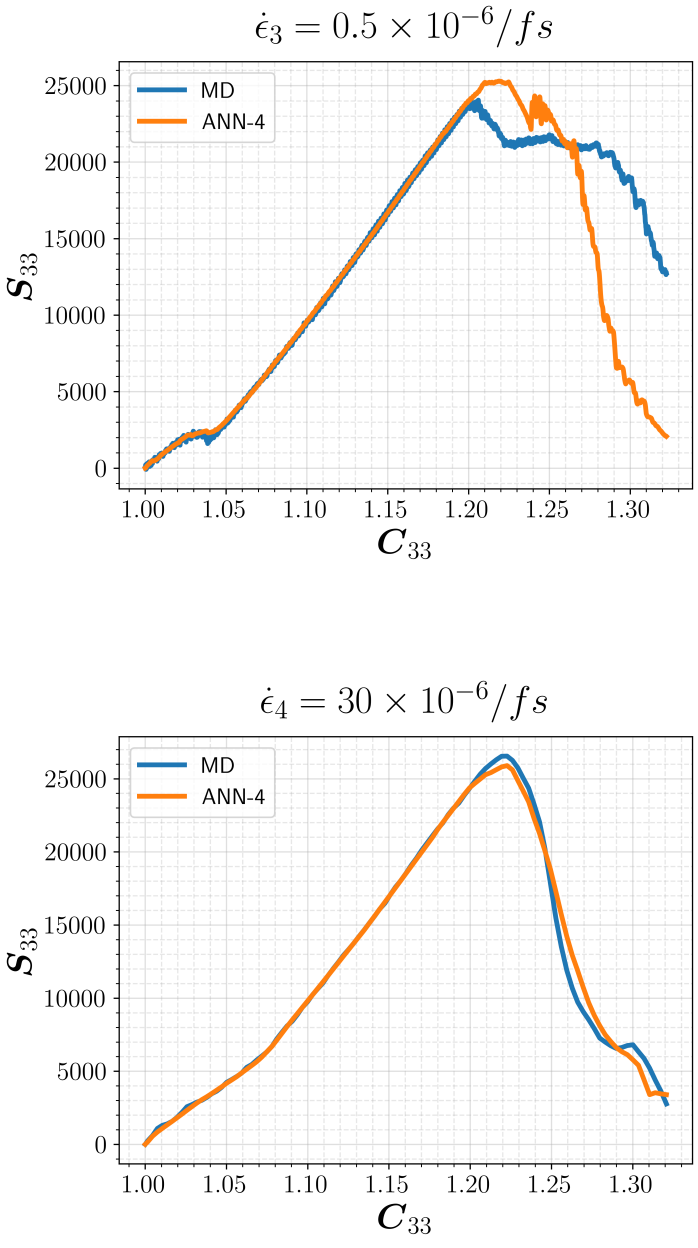

Figure 3.10: Predictions of ANN-4 for uniaxial tension in z-direction for a new set of simulations. The strain rates are beyond the range of the training data.

In order to better quantify model uncertainty of the ANN, we performed an error analysis. We use the same four sets of simulations with different strain rates as previously shown in Figs. 3.9-3.10. We consider the full six components of the prediction, namely the second Piola-Kirchhoff tensor $\hat{\boldsymbol{S}}$, and investigate how the error evolves with the deformation by comparing it to the MD result $\boldsymbol{S}$. Since the use of MSE does not make sense here, we use the percentage error defined below.

$$\text{Percentage Error} = 100 \times \frac{||\boldsymbol{S} - \hat{\boldsymbol{S}}||_2}{||\boldsymbol{S}||_2} \ , \tag{3.13}$$

Results are presented in Fig. 3.11, with respect to the deformation. Note that we used the tensor component C_{33} to represent axial deformation, to be consistent with the previous discussions. We observe that the error remains close to zero for the elastic region, except for the initial loading regime. When the material is further deformed and starts to yield, that is, for $C_{33} > 1.20$, we start to see a significant increase in error. This is expected as the failure mechanism and the material response beyond yielding would involve high uncertainty. Out-of-domain data $\dot{\epsilon}_3$ result in a significant error, especially during the initial loading phase. On the other hand, $\dot{\epsilon}_4$ outcomes are similar to those of the in-range data. From these findings we infer that the model performs better when dealing with faster loading rates, and there is a high uncertainty within the initial loading and the failure regions. Further analysis may be required to draw a final conclusion as the data here were rather limited.

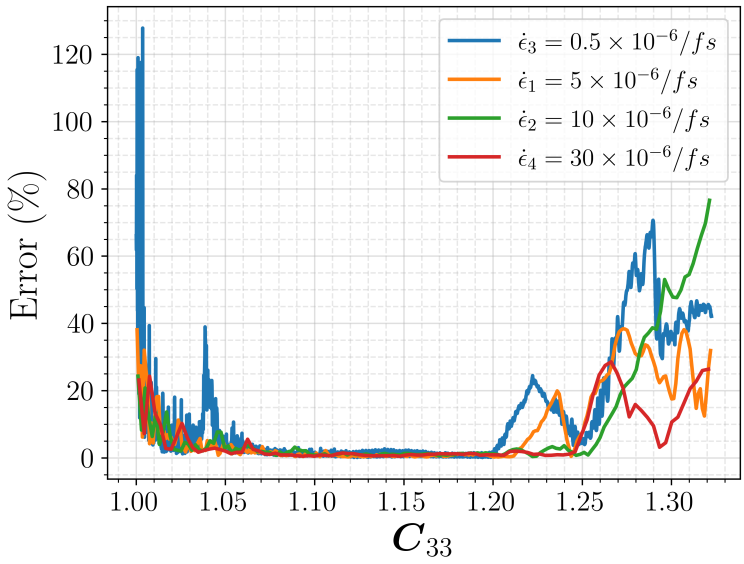

Figure 3.11: Percentage error, as defined in (3.13), for different strain rates.

3.4 Concluding Remarks

In this study, we have developed an artificial neural network to model the mechanical response of crystalline polymers based on molecular dynamics simulations. Initial configurations are generated to model PA12 in γ crystal form. ReaxFF was our choice for the force field, and MD simulations are performed under uniaxial and biaxial tensile deformations to generate a data set for the learning model.

ANN architecture is selected through hyperparameter tuning algorithms and carefully calibrated using the training set. The training and validation process produced the best model to be ANN-4, which is proven to be robust and accurate with no significant overfitting. The best model is tested against different strain rates, which covers above and beyond the loading rate range of the training set. The results demonstrated the predictive power and generalization capacity of our approach, even with strain rates that are much slower or faster than the original data.

The presented methodology proved to be an efficient way of modeling the microstructurally informed constitutive relation of crystalline polymers, which would be used in macroscale FEM simulations. Namely, we presented an approach to accurately predict the mapping between the right Cauchy-Green ($\boldsymbol{C}$) and second PK2 stress ($\boldsymbol{S}$) tensors, which shall be utilized to compute the strain energy density of large deformation problems. Once the model is trained, we can simply treat it as a black box for computing the strain energy at arbitrary quadrature points and time steps, corresponding to the current deformation state of the material.

There are some caveats that need further attention. As detailed in Section 2.3, there may be a mechanically induced phase transformation of PA12, which may depend on the particular additive manufacturing method and process parameters such as temperature and printing speed. Furthermore, we only considered uniaxial and biaxial tensile deformations in our training set. For general loading conditions, such as pure shear, compression, and torsion, the artificial neural network will need more data and the associated ML training procedure may become more complicated and expensive. Nevertheless, the approached outlined in this work can easily be extended to any deformation mode by obtaining the corresponding MD data set and repeating the ML process.

It should be noted that our current investigation was limited to the fully crystalline form of PA12 for demonstration purposes. The actual material components consist of semicrystalline structures wherein the microstructure comprises amorphous and crystalline regions. However, the MD and ML methodologies presented can be easily adopted for amorphous domains. Additionally, considering larger simulation cells, having longer relaxation windows and adopting slower strain rates may be necessary to simulate more accurate and realistic scenarios. These matters will be further investigated and reported in a separate study.

Chapter 4

Polymer Crystallization in Additive Manufacturing

4.1 Introduction

Additive manufacturing (AM), also called 3D printing, is a broad family of technologies that build 3D objects by adding layer upon layer of material. The main advantage of AM is to give the user the freedom to produce complex geometries without being restricted by traditional manufacturing constraints. Historically AM was a tool for rapid prototyping, but with the recent advances in technology, it is now widely used to produce fully functional parts in many industries. AM can be used for a wide range of materials, such as polymers, metals, and ceramics, although it is most commonly used for thermoplastics.

There are many different types of 3D printing techniques, the most common ones being material extrusion and powder-bed type processes. In the material extrusion process, a solid material filament is melted and deposited to define the printed part, whereas in the powder bed process a heat source moves across a bed of granular material, selectively melting and fusing the powder to build the part. These types of AM processes are highly nonisothermal, and the material properties of the manufactured part greatly differ from those of the raw material. The degree of crystallinity is one of the many properties that affects the mechanical properties of thermoplastics.

Finite element methods (FEM) have proved to be useful in many engineering applications and additive AM is no different. Over the past decade, a lot of work has been put into developing and improving the finite element simulations of the AM process; they can now be conducted easily with the help of commercial software, such as Abaqus. It is in the interest of industry to understand the AM process better in order to optimize the production cost and quality by calibrating the design geometry, material, and process specific parameters; FEM provides a convenient way of doing so.

It is crucial to predict the crystallinity evolution during and after the printing process to ensure the desired strength of the polymer. In this part of the research, an FEM simulation was carried out in order to understand the degree of crystallinity change along the printing process. Polyamide-12 (PA12) is used as the material of interest, which is used by Ford Motor Company to produce plastic automobile parts, by using Multi-Jet Fusion (MJF) 3D printing technologies.

Semicrytalline Polyamide12

Polyamide12 (PA12, Nylon12) is a thermoplastic that can be used in additive manufacturing techniques. Due to its good mechanical and thermal properties, it is used in many industries such as aerospace technologies, electronics, and automotive industry. The choice of this material is inspired by the fact that PA12 is used by Ford Motor Companies to produce plastic automobile parts, with the help of Multi-Jet Fusion 3D printing technologies developed by HP Inc. PA12 has the chemical formula $[(CH_2)_{11}C(O)NH]_n$. Having a long and complicated monomer, its crystallization is limited, typically in the range of 15-30%.

4.2 Crystallization Kinetics

When the printed material solidifies from the melt, it forms crystals depending on the cooling rate. However, newly printed material can melt the layer underneath, causing a decrease in the crystallinity. In order to track the evolution of crystallinity, we need to define a kinetic model which would capture both crystallization and melting dynamics and work together.

Crystallization Model

The degree of crystallinity, $\alpha(t)$, is defined as the ratio between the crystallized volume and the ultimate crystallizable volume. In isothermal conditions, it can be computed based on the Avrami theory [5] as follows.

$$\alpha(t) = \frac{x_c(t,T)}{x_\infty} \tag{4.1}$$

$$\alpha(t) = 1 - \exp(-k(T)t^n) \tag{4.2}$$

where $k(T)$ is called the temperature-dependent crystallization rate and n is the Avrami exponent, which stands for the nucleation and growth mechanisms.

This theory was extended by Ozawa [75] to describe nonisothermal conditions at constant cooling rate.

$$X(t) = 1 - \exp(-k(T)\psi^m) \tag{4.3}$$

However, since there is no constant cooling rate in the 3D printing process, the models described above are not sufficient. To model crystallization in more general nonisothermal settings, Nakamura et al. [70, 69] developed a model based on the Avrami theory.

$$\alpha(t) = 1 - \exp(-(\int_0^t K(T)d\tau)^n) \tag{4.4}$$

where n is the Avrami exponent and $K(\tau)$ is the non-isothermal crystallization rate.

For the purpose of the numerical simulations, we need to consider the time differential form of the Nakamura model, which can be derived as:

$$\frac{\partial \alpha}{\partial t} = nK(T)(1-\alpha)\left[\ln\left(\frac{1}{1-\alpha}\right)\right]^{\frac{n-1}{n}} \tag{4.5}$$

Nakamura and Avrami rates can be related to each other via the expression:

$$K(T) = k(T)^{\frac{1}{n}} = \ln(2)^{\frac{1}{n}}\left(\frac{1}{t_{1/2}}\right) \tag{4.6}$$

where $t_{1/2}$ is the half-crystallization time.

Temperature dependent half crystallization time can be determined according to the Hoffman-Lauritzen theory [31]:

$$\frac{1}{t_{1/2}} = K_0 \exp\left(\frac{-U}{R(T-T_\infty)}\right)\exp\left(\frac{-K_G(T+T_0)}{2T^2\Delta T}\right) \tag{4.7}$$

where U = 6270 J/mol is the activation energy, R = 8.314 J/mol is the universal gas constant, $T_\infty = T_g$ – 30K, where T_g is the glass transition temperature, Δ T = T_m – T; where T_m is the equilibrium melting temperature, which can be determined by Hoffman-Weeks construction [32]. K_0 is the growth rate constant, K_G is the nucleation rate constant, and both of these parameters can be determined empirically by means of differential scanning calirometry (DSC) measurements of the material.

For the purpose of this FEM simulation, the results of PA12 DSC measurements from the literature have been used to choose the Avrami exponent and the parameters of the Hoffman-Lauritzen theory. The results of two studies [108, 1], summarized in Table 4.1, have been tested and no significant differences have been observed for our purposes.

Using the Hoffman-Lauritzen theory, half crystallization time can be obtained and then it can be used to calculate the Nakamura rate, which finally leads to the nonisothermal crystallization rate $\frac{\partial \alpha}{\partial t}$.

	1[108]	**2**[1]
K_0 $(1/s)$	37,869	55,600
K_G (K^2)	136,235	140,866
T_0 (°C)	193.2	192.4
T_∞(°C)	21	21
n $(mean)$	2.678	2.618

Table 4.1: Parameters of the Hoffman-Lauritzen Theory

Melting Model

In the AM process, when molten polymer is printed on top of the previous layer, melting can happen which may result in a decrease of crystallinity. The overall model should take care of this phenomena so there is a need to define a melting model.

To express melting behavior, one can adopt a kinetics or statistical approach. In the latter, melting temperature is regarded as a random variable, having a statistical distribution. Generally, a statistical melting model can be developed based on the assumption that the DSC melting peak can be regarded as a statistical distribution of melting temperatures of the crystallites [24].

Melting is expressed by using the degree of melting, X_m, which is equal to 1.0 when the material is fully molten and 0.0 when it is in solid state. Integral curve of the DSC melting peak, defined as X_m, can be regarded as the cumulative distribution function [24].

Following the approach developed by Greco et al. [23, 24], we can model the melting temperature distribution based on a sigmoidal growth curve, known as the Richard's function, (4.8).

$$\frac{dX_m}{dT}(T) = k_m(\exp(-k_m(T-T_p)))(1+(d-1)\exp(-k_m(T-T_p)))^{\frac{d}{1-d}} \tag{4.8}$$

where T_p is the most probable melting temperature, which can be obtained from DSC experiment, and it is the corresponding peak of the signal. k_m and d are fitting factors describing the sharpness and the shape of the distribution.

Using the values $k_m = 0.965\ K^{-1}$, $d = 8.584$ and $T_p = 450$°K [23], we obtain the melting temperature distribution shown in Fig.4.1.

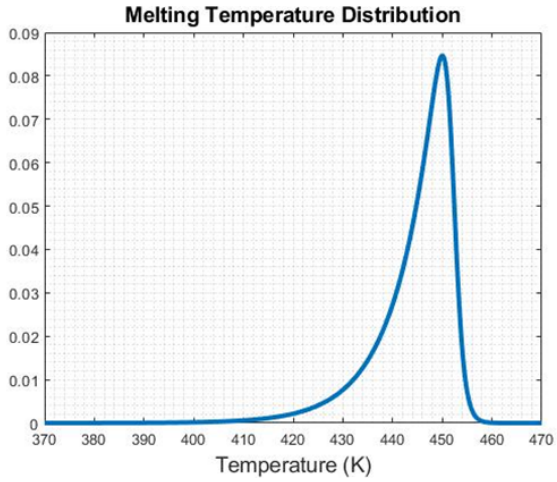

$T > 460 \rightarrow Fully\ Molten \rightarrow X_m = 1.0$

$T < 410 \rightarrow Fully\ Solidified \rightarrow X_m = 0.0$

Figure 4.1: Melting distribution

Finally, we can relate the degree of melting X_m to the degree of crystallization α via

$$\alpha(t + \Delta t) = \alpha(t) - \Delta X_m \ \alpha_{max} \tag{4.9}$$

where α_{max} is the maximum degree of crystallinity.

4.3 Finite Element Analysis for Crystallization

This section describes the FEM based heat transfer analysis of the heat transfer analysis, in which we determine the evolution of the crystallinity. Detailes are provided about the crystallization-melting algorithm and the uncoupled heat analysis as well as their implementation in the commercial FEM software, Abaqus.

Governing Equations for Crystallization and Melting

The crystallization rate can be computed from the Nakamura model combined with the Hoffman-Lauritzen theory. In order to find the time evolution of the crystallinity, we need to numerically integrate the crystallization rate at each time step of the FEM simulation. Euler's method, (4.10), has been chosen as a time integration scheme due to its simplicity. A higher order scheme can be used as well, such as Runge-Kutta 4 (RK4), but the difference is thought to be insignificant since the Euler's method gave promising results.

$$\alpha(t + \Delta t) = \alpha(t) + \Delta t \frac{\partial \alpha(t)}{\partial t} \tag{4.10}$$

$$\frac{\partial \alpha}{\partial t} = nK(T)(1 - \alpha) \left[\ln \left(\frac{1}{1 - \alpha} \right) \right]^{\frac{n-1}{n}} \tag{4.11}$$

Statistical melting model, based on the Richards function and fitted via DSC experiments, has been implemented and its relation to the degree of crystallinity is expressed as follows:

$$\alpha(t + \Delta t) = \alpha(t) - \Delta X_m \ \alpha_{max} \tag{4.12}$$

$$\frac{dX_m}{dT}(T) = k_m(\exp(-k_m(T - T_p)))(1 + (d - 1)\exp(-k_m(T - T_p)))^{\frac{d}{1-d}} \tag{4.13}$$

In the FEM simulation, at each time step we update the degree of crystallinity depending on the resulting temperature. If the material is cooling down and the temperature at the current time step is in the crystallization range, we increase the crystallinity according to the Nakamura model, and if the material is reheated, we adjust the crystallinity according to the melting model. This procedure is summarized in Algorithm 1.

Algorithm 1 Compute degree of crystallinity at each time step

if $T \in \{T_{Crystallization}\}$ **then**

$\frac{\partial \alpha}{\partial t} \leftarrow nK(T)(1 - \alpha)\Big[\ln(\frac{1}{1-\alpha})\Big]^{\frac{n-1}{n}}$

$\alpha \leftarrow \alpha + \Delta t \frac{\partial \alpha}{\partial t}$

else if $T \in \{T_{Melting}\}$ **then**

$\Delta X_m \leftarrow k_m(\exp(-k_m(T - T_p)))(1 + (d - 1)\exp(-k_m(T - T_p)))^{\frac{d}{1-d}}$

$\alpha \leftarrow \alpha - \Delta X_M \alpha_{max}$

else if $T > max\{T_{Melting}\}$ **then**

$\alpha \leftarrow 0$

end if

For the Abaqus implementation, a user subroutine had to be defined. Since a thermal analysis is considered, we needed to implement a UMATHT subroutine, which is normally used to define the thermal constitutive behavior of the material. This subroutine is called for all quadrature points at each time step, and several variables are passed in for the user to define the thermal constitutive relation as well as the internal heat generation during the heat transfer processes. Typically, one needs to update the internal thermal energy, heat flux, and their corresponding time variation and spatial gradients inside UMATHT. In the rest of the subroutine, one can update the solution-dependent state variables, which is the degree of crystallinity in our case.

FEM Formulation

Uncoupled heat transfer is considered as the governing equation of the FEM, where the energy balance of a body Ω with the surface $\partial\Omega$ with the expressed as follows.

$$\int_{\Omega} \rho \dot{U} dV - \int_{\partial\Omega} q dS - \int_{\Omega} r dV = 0 \tag{4.14}$$

where U is the internal thermal energy, r is the external heat per volume and $q = -\boldsymbol{f} \cdot \boldsymbol{n}$ is the heat flux where the $\boldsymbol{f}$ is the heat flux vector and $\boldsymbol{n}$ is the surface normal to $\partial\Omega$, ρ is the density of the material.

Using the above relations and the divergence theorem, we can obtain:

$$\int_{\Omega} \rho \dot{U} dV + \int_{\Omega} \frac{\partial}{\partial \boldsymbol{x}} \cdot \boldsymbol{f} dV - \int_{\Omega} r dV = 0 \tag{4.15}$$

Considering an admissible variation of the temperature, δT, we obtain the weak form as follows.

$$\int_{\Omega} \delta T \rho \dot{U} dV - \int_{\Omega} \delta \nabla T \cdot \boldsymbol{f} dV - \int_{\Omega} \delta\theta r dV - \int_{\partial\Omega} \delta\theta q dS = 0 \tag{4.16}$$

Assuming constant specific heat and conductivity and using Fourier's law, it is straightforward to update the necessary variables. After updating the energy, flux, and corresponding gradients, the combined crystallization/melting model described in the below Algorithm 1 is implemented in the UMATHT subroutine. Further details and the full implementation can be found in Appendix B.

Simulation Setup

A finite element simulation of the 3D printing process has been developed using the commercial software Abaqus. Because the objective is to understand the evolution of crystallinity, a thermal analysis is conducted. The governing equation for uncoupled heat transfer is described in (4.16). A simple bar geometry is adopted for the simulation, which is printed layer by layer on top of a glass substrate, Fig. 4.2.

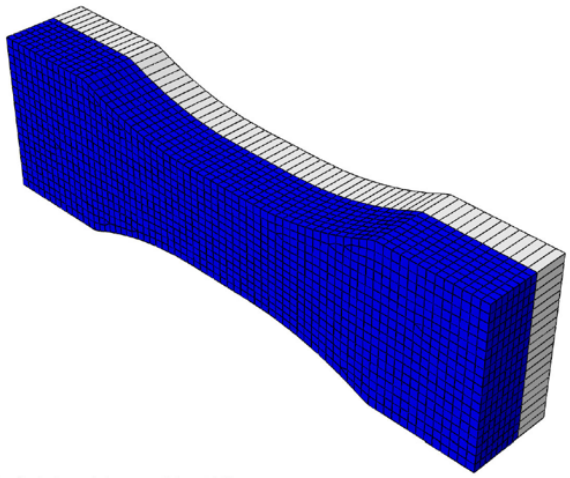

Figure 4.2: Printed part (blue) and glass substrate (white)

The melted material, PA12, comes at an initial temperature 220°C and printed on the glass, which is initially set at 80° C. Dirichlet boundary conditions are enforced on the bottom boundary of the substrate, at 80°C, Fig. 4.3. The convection and radiation coefficients are adjusted accordingly to allow for a smooth temperature gradient and a cooling rate that is slow enough to observe crystal growth.

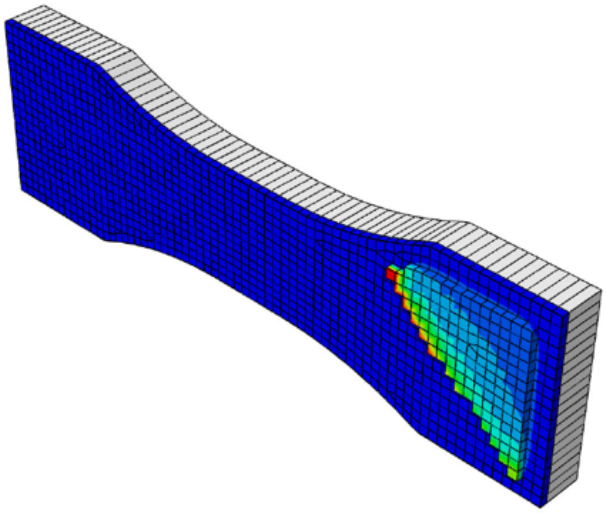

(a) Printing of the new layer at 220 °C

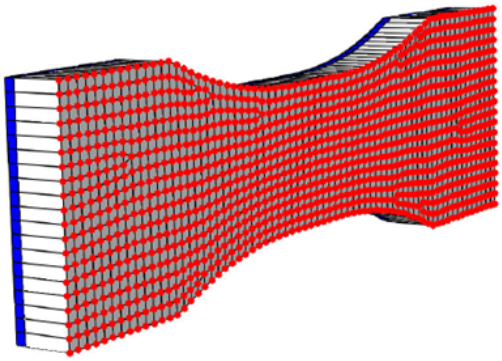

(b) Bottom boundary fixed at 80 °C

Figure 4.3: Initial and boundary conditions of the FEM setup

It is relatively straightforward to conduct these types of thermal simulation in Abaqus, which allows the user to control the process parameters. The main novelty here is the incorporation of crystallinity evolution into the non-isothermal process, which was done as explained in Algorithm 1.

Results

First, a verification study for the user-defined subroutine is carried out before applying it to the printing process simulation. For this purpose, we supplied a temperature history to the software to test if the crystallization/melting model works properly.

The cooling rate strongly affects the crystallization rate; therefore, three cooling rates have been chosen for testing; 1 K/min, 2 K/min and 10 K/min. The corresponding temperature histories were obtained by heating the material to 200° C, then cooling it to 120° C for each cooling rate. Fig. 4.4 represents the temperature histories described.

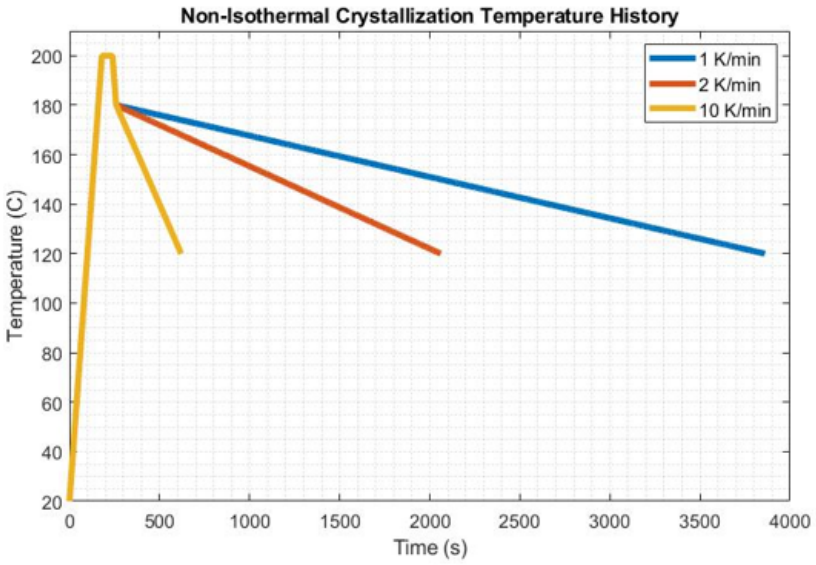

Figure 4.4: Temperature histories of the AM process

After supplying the above temperature histories to the subroutine, the degree of crystallization versus temperature relations are obtained, Fig. 4.6. The results presented here are in great agreement with the findings of Zhao et al. [108] for the nonisothermal crystallization kinetics of PA12.

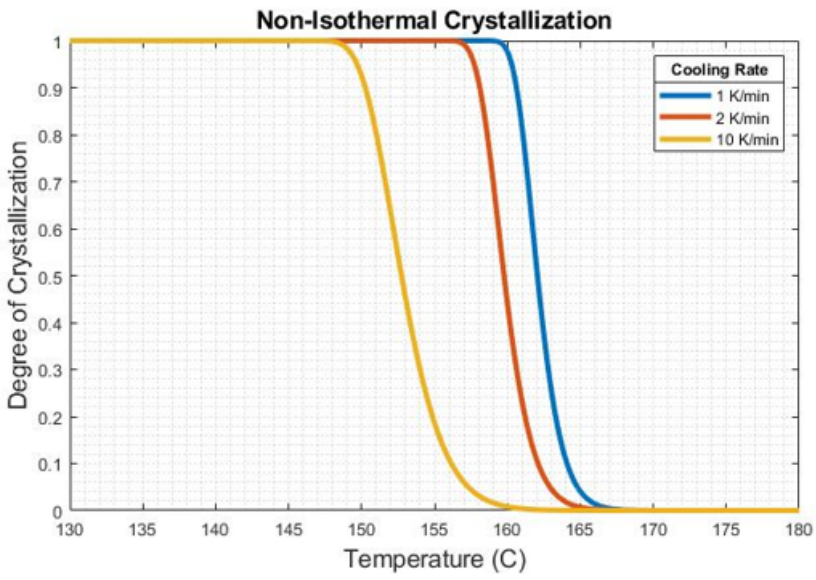

Figure 4.5: Temperature versus degree of crystallization from FEM, for different cooling rates.

Now, the user-defined material subroutine is applied to the simulation of the printing process. First, let us investigate the nodal temperature history. Looking at a typical node from the first printed layer, Fig. 4.6 (a), we see the nodal temperature (NT11) distribution as expected. The new material comes at 220°C and it is cooled down when the rest of the current layer is being printed. When the new layer is printed on top, there is a jump in the nodal temperature, which indicates reheating of the bottom layers due to incoming melted material. Then the material is cooled down until a new layer is printed, which again causes reheating. The cycle continues until the process is complete. After several layers are printed, the temperature change due to the newly printed layer becomes negligible, and the temperature stays constant. The time history of a typical node from the first layer is depicted in Fig. 4.6 (b).

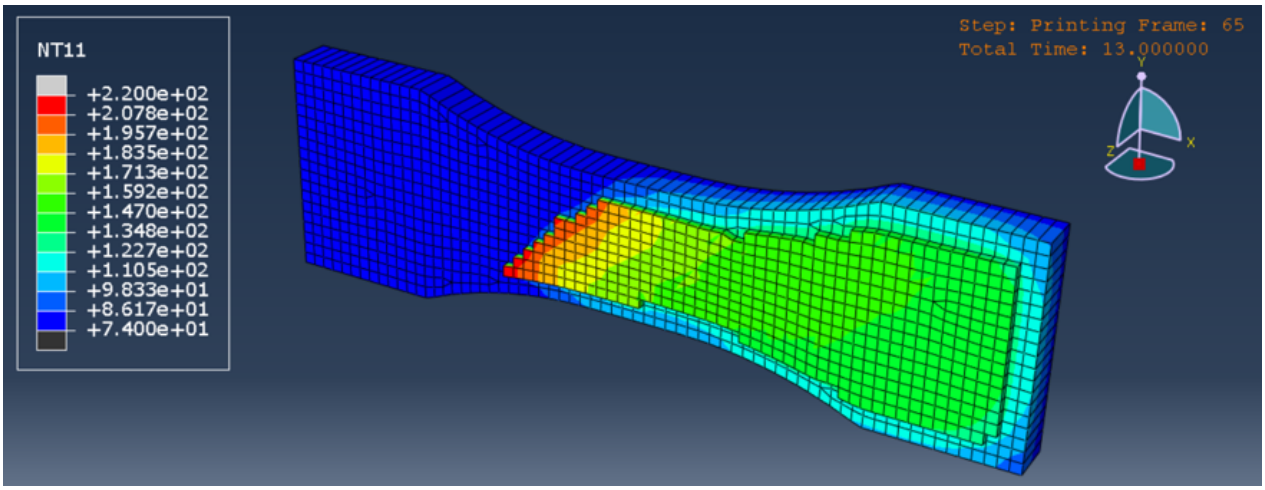

(a) Temperature distribution during printing process.

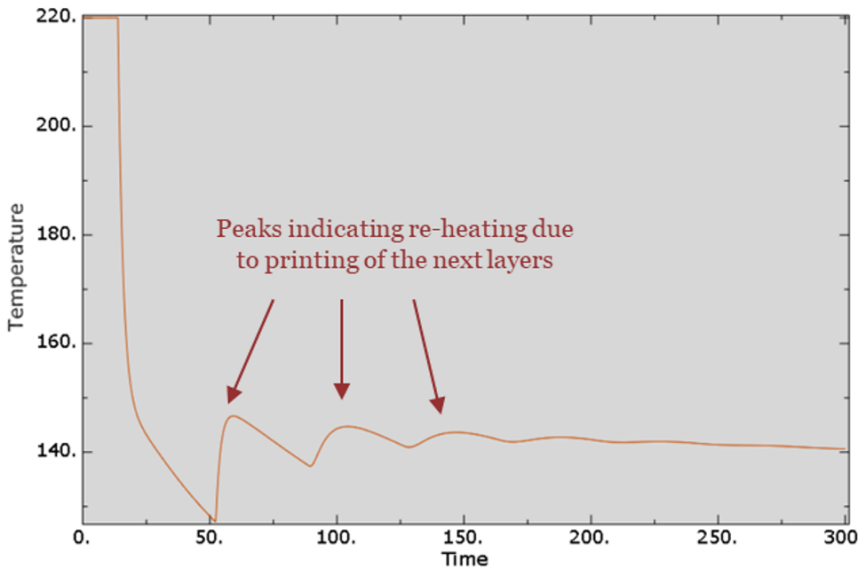

(b) Temperature history of a typical node

Figure 4.6: Temperature distribution and history of the first layer.

In order to confirm this phenomenon in the entire domain, we can look at layer six, Fig. 4.7. We again see a similar behavior, now only having two separate jumps in the temperature due to the printing of the seventh and the eighth (final) layer.

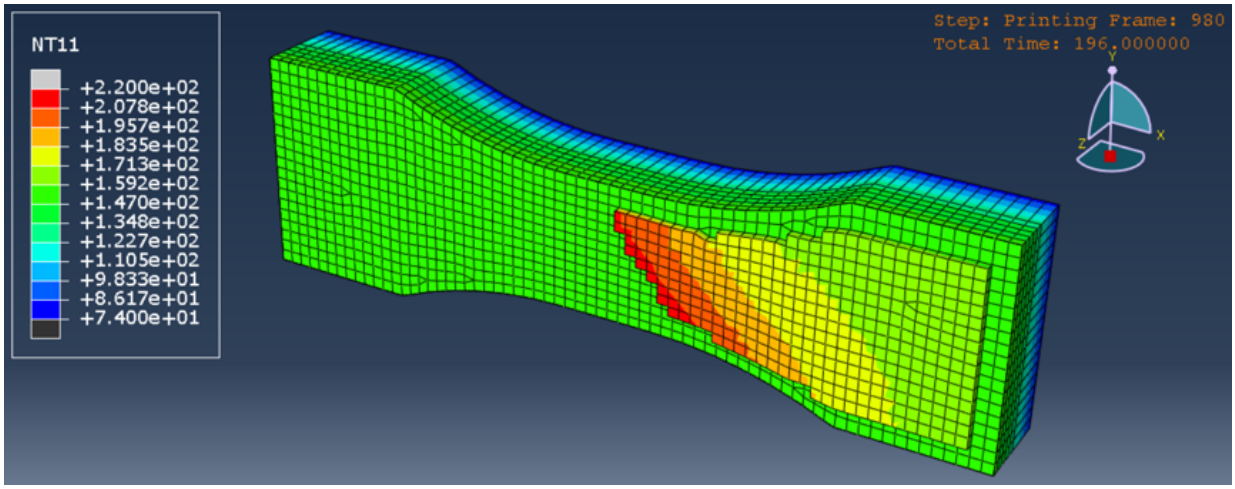

(a) Temperature distribution during printing process.

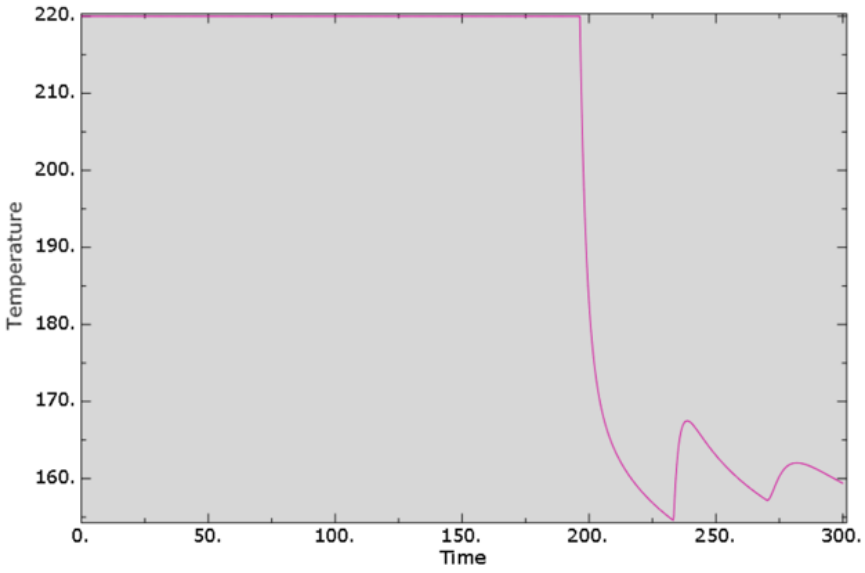

(b) Temperature history of a typical node.

Figure 4.7: Temperature distribution and history of the sixth layer.

When we look at the degree of crystallization, we do not see a clear picture as we did for the nodal temperature since it takes time for the material to cool down and to see any growth in the crystallinity. By the time being, a new layer is printed on top, preventing us from seeing it clearly, like the one in Fig. 4.8. Note that maximum degree of crystallization is assumed to be 25 %.

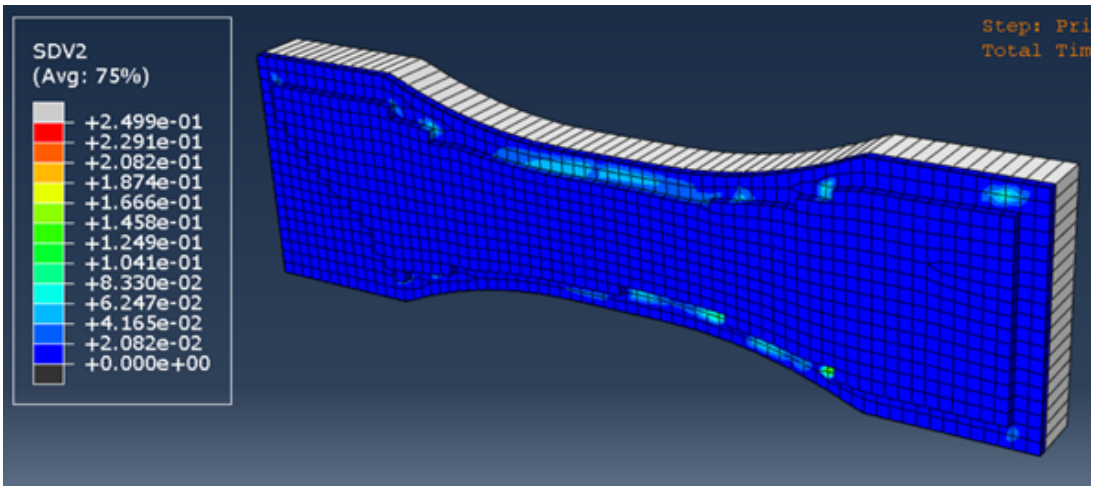

Figure 4.8: Crystallinity evolution during the printing

Looking at a typical node in layer 1, Fig. 4.9 (a), we can see that when a new layer is printed, there is a disruption in crystal growth due to the heat flux coming from the new layer, but it is not sufficient enough to melt the material. At the end of the process, layer 1 fully crystallizes, up to the maximum degree of crystallization, which is assumed to be 25 %. In layer 6, Fig. 4.9 (b), behavior is somewhat different. Because this is close to the end of the process, the material does not cool enough to see a significant increase in the degree of crystallization. However, now there is melting happening when a new layer is being printed, although the effect can be neglected because the degree of crystallization at this layer is relatively small.

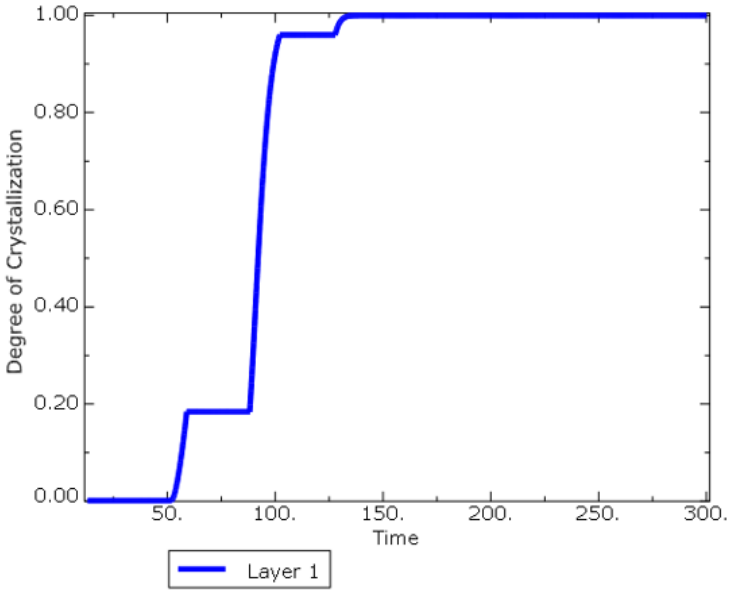

(a) Layer 1

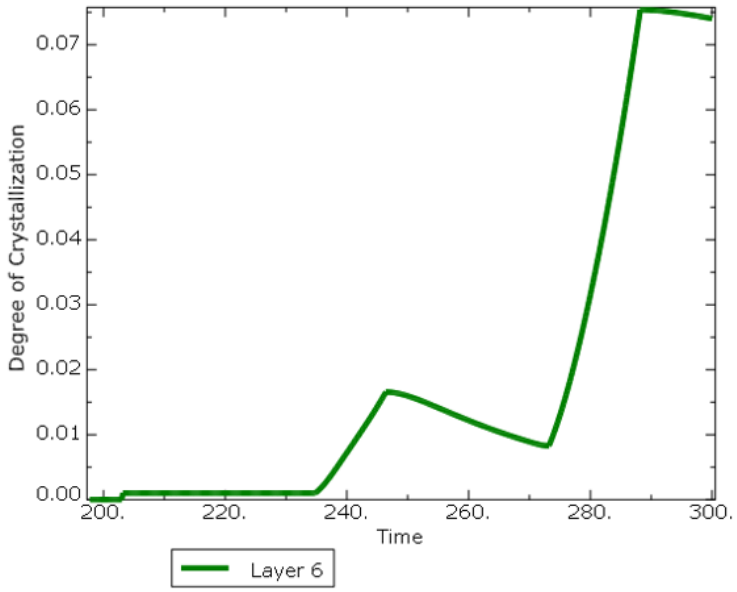

(b) Layer 6

Figure 4.9: Degree of crystallization history.

4.4 Concluding Remarks

In this chapter, our objective was to provide significant advances in understanding the crystallization behavior of semicrystalline polymers during the additive manufacturing process. Using the finite element method (FEM) to conduct a heat analysis with integrated crystallization and melting models, this research has demonstrated the ability to predict and control the evolution of crystallinity under varying thermal conditions of 3D printing.

The study has successfully integrated Nakamura and Hoffman-Lauritzen theories to model the nonisothermal crystallization kinetics of Polyamide-12 (PA12). Incorporation of these models into FEM simulations allows prediction of changes in crystallinity during the printing process, which is crucial for achieving desired mechanical properties in the final product. The user-defined UMATHT subroutine developed for this study effectively captures the thermally induced crystallization and melting dynamics. This subroutine provides a tool for simulating the additive manufacturing of semicrystalline polymers, offering potential for optimization in industrial applications.

The results indicate that the thermal history of the material, particularly the cooling rates, significantly influences the degree of crystallinity. This highlights the importance of temperature control within the printing process in adjusting the properties of the material to specific applications.

The method can be easily tailored to any semicrystalline material provided sufficient experimental data exist. Furthermore, the technique can be translated into larger scale manufacturing simulations as well as different printing methods, which would provide insights into industry applications to achieve specific material properties.

Chapter 5

Conclusion

Polymers, materials with large molecules made up of repeating structural units, play a crucial role in numerous engineering applications. With recent advances in manufacturing techniques and material design, it is becoming increasingly important to develop a better understanding of the mechanics of polymer-based materials, which is the central theme of this dissertation. Traditionally in computational mechanics, polymer-based materials and elastomers are treated as hyperelastic solids, which may fall short in modeling complex nonlinear scenarios, including fracture mechanics and finite deformation problems. Our work aims to explore the mechanics of polymers by focusing on the underlying structure and micromechanical treatments by utilizing numerical methods that include peridynamics, finite elements, molecular dynamics, and deep neural networks with a particular focus on the realms of fracture mechanics, large deformations, and additive manufacturing processes.

In the second chapter, a numerical framework has been introduced to analyze the fracture and large-deformation mechanics of elastomers. The work utilized bond-based peridynamics, which is a nonlocal continuum formulation that can capture discontinuities such as crack propagation in the material. We introduced a mesoscale bond potential function into the framework, which acts as the constitutive model for the elastomer. The potential is based on the non-Gaussian statistical mechanics formulations of single polymer chains, also known as Langevin statistics, and we treat the material as a network of random chains with extensible links. The resultant model can be thought of as an alternative to the hyperelastic continuum models such as the Arruda-Boyce model, with the additional advantage of being able to capture the fracture and crack propagation in the material. The proposed model is calibrated through experimental data using tensile deformation simulations, and several numerical examples were provided in two- and three-dimensional simulations. Some benchmark problems of fracture mechanics are simulated, such as the Mode-I and Mode-II opening, the double edge-notch, and the cylindrical bar under tension. The numerical demonstrations revealed that the nonlocal model handles fracture processes in elastomeric materials under finite deformation without the need for complex ad hoc modeling parameters. By providing a novel simulation approach, the proposed model could influence the developments in the polymer- or elastomer-based designs in engineering applications. One caveat to our current method

is its inability to account for the incompressibility conditions due to the restriction on the Poisson's ratio, which may be overcome by extending the method into the non-ordinary bond-based peridynamics framework that accounts for the shear deformation of the bonds.

Subsequent chapters examined semicrystalline polymers utilized in additive manufacturing, with a focus on multiscale constitutive modeling and crystallization analysis. Conventional modeling techniques often fall short particularly near failure points, due to the complex microstructure of these materials. Greater precision may be achieved through multiscale methods that combine molecular dynamics and finite element analysis. To bridge the gap between atomistic structure and macroscale behavior, we proposed a multiscale constitutive modeling approach in Chapter 3. The method is based on modeling the crystalline structure of PA12 and using molecular dynamics simulations to understand its mechanical response in various deformation modes. Due to the computational expenses of molecular dynamics, deep neural networks that are trained on the MD data are utilized to capture the stress-strain response of the material at the atomistic scale. The resulting neural networks can be thought of as surrogate models that replace the constitutive relations of the crystalline polymers. We have shown that the approach allows for the precise prediction of stress-strain relationships when a macroscale deformation gradient is input into neural networks and it is accurate beyond the training data range. The methodology offers an efficient method that delivers a three-dimensional molecular-level anisotropic constitutive relation that may be used for any macroscale mechanics model, such as finite element analysis.

In the final chapter, we discuss a finite element-based simulation approach to predict the evolution of crystallinity in semicrystalline polymers during the additive manufacturing process. The degree of crystallinity significantly influences the mechanical properties of polymers, and thus it is vital to understand how the process parameters impact crystallization. We applied the Nakamura and Hoffman-Lauritzen theories to model the nonisothermal crystallization kinetics of PA12. A statistical melting model was introduced to account for the potential effects of the molten material on the crystallinity of previously printed layers. The crystallization and melting models were then incorporated into an uncoupled transient heat transfer analysis utilizing a user-subroutine to define the thermal constitutive relations in a finite element analysis. We have observed that the thermal history, particularly the cooling rate during the manufacturing process, significantly affects the degree of crystallinity. The work provided a tool for simulating the additive manufacturing process and highlighted the importance of temperature control to achieve the desired crystallinity in the final product. Our technique can be adopted to any semicrystalline material and used for large-scale manufacturing simulations as well as for different printing methods, which would provide insights into industry applications to achieve specific material properties.

Appendix A

Micro to Macroscale Material Constants

2D Plane Stress Case

We would like to carry the double integration to compute the elasticity tensor. For the plane stress conditions with thickness t in the e_3 direction, the horizon has volume $\Omega_{\boldsymbol{X}} = \pi R^2 t$. Consider the coordinate system depicted below:

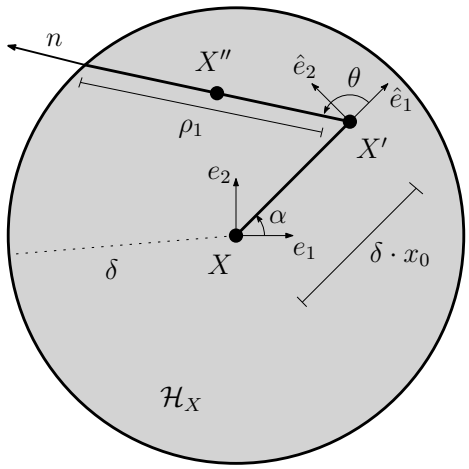

Figure A.1: Horizon in 2D

$$\boldsymbol{x} = \cos\alpha \boldsymbol{e_1} + \sin\alpha \boldsymbol{e_2} \tag{A.1}$$

$$\hat{\boldsymbol{e}}_{\boldsymbol{1}} = \cos\alpha \boldsymbol{e_1} + \sin\alpha \boldsymbol{e_2} \tag{A.2}$$
$$\hat{\boldsymbol{e}}_{\boldsymbol{2}} = -\sin\alpha \boldsymbol{e_1} + \cos\alpha \boldsymbol{e_2} \tag{A.3}$$

$$\hat{\boldsymbol{e}}_i = Q_{ij}\boldsymbol{e}_j \qquad \text{where} \qquad Q = \begin{bmatrix} \cos\alpha & \sin\alpha \\ -\sin\alpha & \cos\alpha \end{bmatrix} \tag{A.4}$$

$$\begin{aligned} \boldsymbol{n} &= \cos\theta \hat{\boldsymbol{e}}_1 + \sin\theta \hat{\boldsymbol{e}}_2 && \text{(A.5)} \\ &= \cos\theta Q_{1i}\boldsymbol{e}_i + \sin\theta Q_{2j}\boldsymbol{e}_j && \text{(A.6)} \\ &= n_1\boldsymbol{e}_1 + n_2\boldsymbol{e}_2 && \text{(A.7)} \end{aligned}$$

Let $\hat{n}_1 = \cos\theta$ and $\hat{n}_2 = \sin\theta$, thus we have $n_i = Q_{ij}\hat{n}_j$
The integral becomes

$$\begin{aligned} I_1 &= \int_{\mathcal{H}_{\boldsymbol{X}}}\int_{\mathcal{H}_{\boldsymbol{X}}} \frac{1}{|\boldsymbol{\xi}^3|}(\boldsymbol{\xi}\otimes\boldsymbol{\xi}\otimes\boldsymbol{\xi}\otimes\boldsymbol{\xi})dX'dX'' && \text{(A.8)} \\ &= t\int_{\mathcal{H}_{\boldsymbol{X}}}\int_0^{2\pi}\int_0^{\rho} n_i n_j n_k n_l r^2 dr d\theta dX' && \text{(A.9)} \\ &= t\int_{\mathcal{H}_{\boldsymbol{X}}}\int_0^{2\pi} n_i n_j n_k n_l \frac{1}{3}\rho_1^3 d\theta dX' && \text{(A.10)} \\ &= t\int_{\mathcal{H}_{\boldsymbol{X}}}\int_0^{2\pi} Q_{ip}\hat{n}_p Q_{jq}\hat{n}_q Q_{kr}\hat{n}_r Q_{ls}\hat{n}_s \frac{1}{3}\rho_1^3 d\theta dX' && \text{(A.11)} \\ &= t\int_{\mathcal{H}_{\boldsymbol{X}}} Q_{ip}Q_{jq}Q_{kr}Q_{ls}\int_0^{2\pi} \hat{n}_p\hat{n}_q\hat{n}_r\hat{n}_s \frac{1}{3}\rho_1^3 d\theta dX' && \text{(A.12)} \end{aligned}$$

where

$$\rho_1 = R\left(-x_0\hat{n}_1 + \sqrt{1 - x_0^2\hat{n}_2^2}\right) \ . \tag{A.13}$$

Grouping the terms for the integration in the unit circle, we define

$$\mathcal{L}(\hat{n}_i) := \hat{n}_p\hat{n}_q\hat{n}_r\hat{n}_s\frac{1}{3}\rho_1^3 = \hat{n}_p\hat{n}_q\hat{n}_r\hat{n}_s\frac{1}{3}R^3\left(-x_0\hat{n}_1 + \sqrt{1 - x_0^2\hat{n}_2^2}\right)^3 \ . \tag{A.14}$$

Considering the fact that

$$\int_{S_2} \mathcal{L}_{odd}(\hat{n}_i)d\theta = 0 \qquad \text{and} \qquad \int_{S_2} \mathcal{L}_{even}(\hat{n}_i)d\theta \neq 0 \ , \tag{A.15}$$

where

$$\mathcal{L}_{even}(\hat{n}_i) = \hat{n}_p\hat{n}_q\hat{n}_r\hat{n}_s\frac{1}{3}R^3\left[3x_0^2\hat{n}_1^2\sqrt{1-x_0^2\hat{n}_2^2} + (1-x_0^2\hat{n}_2^2)^{3/2}\right] \tag{A.16}$$

Finally, the integration evaluates to the following form,

$$I_1 = t^2\int_0^{2\pi} Q_{ip}Q_{jq}Q_{kr}Q_{ls}\int_0^1\int_0^{2\pi}\mathcal{L}_{even}(\hat{n}_i)d\theta R^2 dx_0 d\alpha \tag{A.17}$$

$$= t^2\frac{R^5\pi^2}{6}(\delta_{ij}\delta_{kl} + \delta_{ik}\delta_{jl} + \delta_{il}\delta_{jk}) \ . \tag{A.18}$$

Therefore,

$$\frac{1}{2\Omega_{\boldsymbol{X}}}\int_{\mathcal{H}_{\boldsymbol{X}}}\int_{\mathcal{H}_{\boldsymbol{X}}}\frac{1}{|\boldsymbol{\xi}^3|}(\boldsymbol{\xi}\otimes\boldsymbol{\xi}\otimes\boldsymbol{\xi}\otimes\boldsymbol{\xi})d\boldsymbol{X}'d\boldsymbol{X}'' = \frac{tR^3\pi}{12}(\delta_{ij}\delta_{kl} + \delta_{ik}\delta_{jl} + \delta_{il}\delta_{jk}) \ . \tag{A.19}$$

Three-dimensional Case and Plane Strain Case

Under the three-dimensional and plane strain conditions, we can choose a spherical horizon $\Omega_{\boldsymbol{X}} = 4/3\pi R^3$. Considering the coordinate system below:

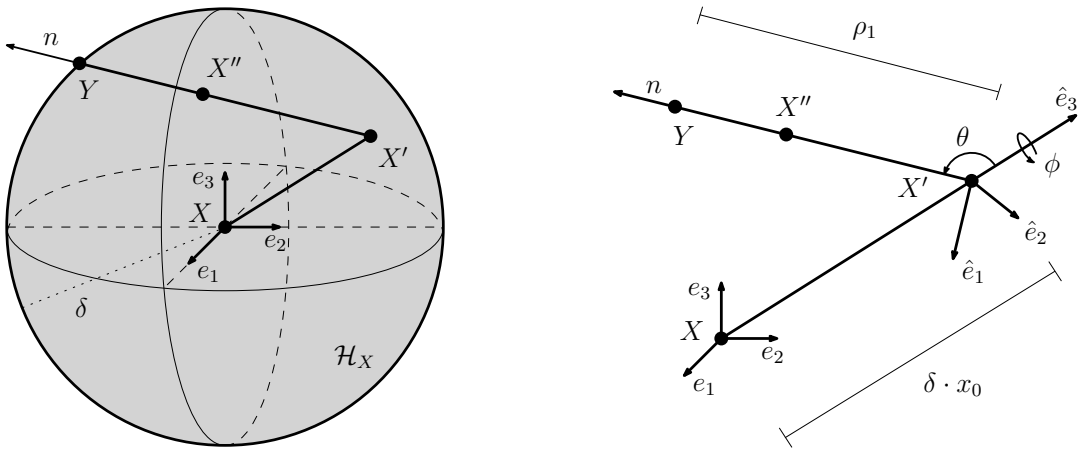

Figure A.2: Horizon in 3D

$$\boldsymbol{x} = \cos\beta \sin\alpha \boldsymbol{e_1} + \sin\beta \cos\alpha \boldsymbol{e_2} \cos\alpha \boldsymbol{e_3} \tag{A.20}$$

$$\hat{\boldsymbol{e}}_{\boldsymbol{1}} = \cos\alpha\cos\beta \boldsymbol{e_1} - \sin\beta \boldsymbol{e_2} + \cos\beta\sin\alpha \boldsymbol{e_3} \tag{A.21}$$

$$\hat{\boldsymbol{e}}_{\boldsymbol{2}} = \cos\alpha\cos\beta \boldsymbol{e_1} + \cos\beta \boldsymbol{e_2} + \sin\beta\sin\alpha \boldsymbol{e_3} \tag{A.22}$$

$$\hat{\boldsymbol{e}}_{\boldsymbol{3}} = -\sin\alpha \boldsymbol{e_1} + \cos\alpha \boldsymbol{e_3} \tag{A.23}$$

$$\hat{\boldsymbol{e}}_i = Q_{ji}\boldsymbol{e}_j \qquad where \qquad Q = \begin{bmatrix} \cos\alpha\cos\beta & -\sin\beta & \cos\beta\sin\alpha \\ \cos\alpha\cos\beta & \cos\beta & \sin\beta\sin\alpha \\ -\sin\alpha & 0 & \cos\alpha \end{bmatrix} \tag{A.24}$$

$$\boldsymbol{n} = \cos\phi\sin\theta\hat{\boldsymbol{e}}_1 + \sin\phi\sin\theta\hat{\boldsymbol{e}}_2 + \cos\theta\hat{\boldsymbol{e}}_3 \tag{A.25}$$

$$= \cos\phi\sin\theta Q_{1i}\boldsymbol{e_i} + \sin\phi\sin\theta Q_{2j}\boldsymbol{e_j} + \cos\theta Q_{3k}\boldsymbol{e_k} \tag{A.26}$$

$$= n_1\boldsymbol{e_1} + n_2\boldsymbol{e_2} + n_3\boldsymbol{e_3} \tag{A.27}$$

Let $\hat{n}_1 = \cos\phi\sin\theta$, $\hat{n}_2 = \sin\phi\sin\theta$ and $\hat{n}_3 = \cos\theta$, thus $n_i = Q_{ij}\hat{n}_j$. Therefore, the integral becomes

$$I_1 = \int_{\mathcal{H}_{\boldsymbol{X}}}\int_{\mathcal{H}_{\boldsymbol{X}}} \frac{1}{|\boldsymbol{\xi}^3|}(\boldsymbol{\xi}\otimes\boldsymbol{\xi}\otimes\boldsymbol{\xi}\otimes\boldsymbol{\xi})dX'dX'' \tag{A.28}$$

$$= \int_{\mathcal{H}_{\boldsymbol{X}}}\int_{S_2}\int_0^{\rho_1} n_i n_j n_k n_l r^4 dr d\omega_2 dX' \tag{A.29}$$

$$= \int_{\mathcal{H}_{\boldsymbol{X}}}\int_{S_2} n_i n_j n_k n_l \frac{1}{4}\rho_1^4 d\omega_2 dX' \tag{A.30}$$

$$= \int_{\mathcal{H}_{\boldsymbol{X}}}\int_{S_2} Q_{ip}\hat{n}_p Q_{jq}\hat{n}_q Q_{kr}\hat{n}_r Q_{ls}\hat{n}_s \frac{1}{4}\rho_1^4 d\omega_2 dX' \tag{A.31}$$

$$= \int_{\mathcal{H}_{\boldsymbol{X}}} Q_{ip}Q_{jq}Q_{kr}Q_{ls}\int_0^{2\pi}\hat{n}_p\hat{n}_q\hat{n}_r\hat{n}_s\frac{1}{4}\rho_1^4 d\omega_2 dX' \tag{A.32}$$

where

$$\rho_1 = R\left(-x_0\hat{n}_3 + \sqrt{1 - x_0^2(\hat{n}_1^2+\hat{n}_2^2)}\right) \ . \tag{A.33}$$

Grouping the terms for integration in S_2, we define

$$\mathcal{L}(\hat{n}_i) := \hat{n}_p\hat{n}_q\hat{n}_r\hat{n}_s\frac{1}{4}\rho_1^4 = \hat{n}_p\hat{n}_q\hat{n}_r\hat{n}_s\frac{1}{4}R^4\left(-x_0\hat{n}_1 + \sqrt{1 - x_0^2(\hat{n}_1^2+\hat{n}_2^2)}\right)^4 \ . \tag{A.34}$$

Considering the fact that

$$\int_{S_2}\mathcal{L}_{odd}(\hat{n}_i)d\omega_2 = 0 \qquad \text{and} \qquad \int_{S_2}\mathcal{L}_{even}(\hat{n}_i)d\omega_2 \neq 0 \ , \tag{A.35}$$

where

$$\mathcal{L}_{even}(\hat{n}_i) = \hat{n}_p\hat{n}_q\hat{n}_r\hat{n}_s\frac{1}{4}R^4\left[x_0^4 n_1^4 + 6x_0^2\hat{n}_1^2\left(1 - x_0^2(\hat{n}_1^2+\hat{n}_2^2)\right) + \left(1 - x_0^2(\hat{n}_1^2+\hat{n}_2^2)\right)^2\right] \tag{A.36}$$

one can readily carry out the integration, which yields the following close-form expression,

$$I_1 = \int_0^{2\pi} Q_{ip}Q_{jq}Q_{kr}Q_{ls}\int_0^1\int_{S_2}\mathcal{L}_{even}(\hat{n}_i)d\omega_2 R^3 x_0^2 dx_0 d\omega_1 \tag{A.37}$$

$$= \frac{8R^7\pi^2}{45}(\delta_{ij}\delta_{kl} + \delta_{ik}\delta_{jl} + \delta_{il}\delta_{jk}) \ . \tag{A.38}$$

Therefore, we finally obtain

$$\frac{1}{2\Omega_{\boldsymbol{X}}}\int_{\mathcal{H}_{\boldsymbol{X}}}\int_{\mathcal{H}_{\boldsymbol{X}}}\frac{1}{|\boldsymbol{\xi}^3|}(\boldsymbol{\xi}\otimes\boldsymbol{\xi}\otimes\boldsymbol{\xi}\otimes\boldsymbol{\xi})dX'dX'' = \frac{R^4\pi}{15}(\delta_{ij}\delta_{kl} + \delta_{ik}\delta_{jl} + \delta_{il}\delta_{jk}) \ . \tag{A.39}$$

Appendix B

UMATHT Subroutine

```
 SUBROUTINE SDVINI(STATEV,COORDS,NSTATV,NCRDS,NOEL,NPT,
1 LAYER,KSPT)

 INCLUDE 'ABA_PARAM.INC'

 DIMENSION STATEV(NSTATV),COORDS(NCRDS)

 STATEV(1) = 1E-3
 STATEV(2) = 0.D0

 RETURN
 END


 SUBROUTINE UMATHT(U,DUDT,DUDG,FLUX,DFDT,DFDG,
1 STATEV,TEMP,DTEMP,DTEMDX,TIME,DTIME,PREDEF,DPRED,
2 CMNAME,NTGRD,NSTATV,PROPS,NPROPS,COORDS,PNEWDT,
3 NOEL,NPT,LAYER,KSPT,KSTEP,KINC)

 INCLUDE 'ABA_PARAM.INC'

 CHARACTER*80 CMNAME
 REAL :: ALPHA
 REAL :: TEMPK
 REAL :: THALF
 REAL :: DALPHADT
 REAL :: MELT
 REAL :: ALPHANEWMELT
 REAL :: DXM
```

```
      REAL :: KT
      REAL :: TG = 324
      REAL :: K0 = 3.787E+4
      REAL :: KG = 136235
      REAL :: T0 = 466
      REAL :: TINF = 294
      REAL :: NAVRAMI = 2.678
      REAL :: ALPHAINIT = 1E-3
      REAL :: ALPHAMAX = 0.25
      REAL :: UACT = 6270
      REAL :: R = 8.314
      REAL :: KM = 0.965
      REAL :: D = 8.58
      REAL :: TC = 450
      REAL :: ALPHANEW


      DIMENSION DUDG(NTGRD),FLUX(NTGRD),DFDT(NTGRD),
     1 DFDG(NTGRD,NTGRD),STATEV(NSTATV),DTEMDX(NTGRD),
     2 TIME(2),PREDEF(1),DPRED(1),PROPS(NPROPS),COORDS(3)

C    PART1: UNCOUPLED HEAT TRANSFER

      COND = PROPS(1)
      SPECHT = PROPS(2)

      DUDT = SPECHT
      DU = DUDT*DTEMP
      U = U+DU

      DO I=1, NTGRD
         FLUX(I) = -COND*DTEMDX(I)
         DFDG(I,I) = -COND
      END DO

C        PART2: NON-ISOTHERMAL CRYSTALLINITY/MELTING OF PA12
C    (The Nakamura Model)
C    CRYSTALLIZATION

          TEMPK = TEMP+273.D0
        ALPHA = STATEV(1)
          ALPHANEW = ALPHA
```

```
      IF (DTEMP .GT. 0.D0) THEN
        THALF = K0*EXP(-UACT/(R*(TEMPK-TINF)))*EXP(-KG*(TEMPK+T0)/
        (2.D0*(T0-TEMPK)*(TEMPK**2.D0)))
            KT = ((LOG(2.D0))**(1.D0/NAVRAMI))*THALF
        DALPHADT = NAVRAMI*KT*(1.D0-ALPHA)*
        ((LOG(1.D0/(1.D0-ALPHA)))**((NAVRAMI-1.D0)/NAVRAMI))
            ALPHANEW = ALPHA+(DTIME*DALPHADT)
      END IF

C     STATISTICAL MELTING MODEL

      IF (DTEMP .LT. 0.D0) THEN

      IF (TEMPK .GT. 460.D0 ) THEN
            ALPHANEW = ALPHAINIT
      ELSE IF (TEMPK .GT. 420.D0) THEN
            MELT = KM*EXP(-KM*(TEMPK-TC))*(1.D0+(d-1.D0)
            *EXP(-KM*(TEMPK-TC)))**(D/(1.D0-D))
            DXM = MELT*ABS(DTEMP)
            ALPHANEWMELT = ALPHA-DXM*ALPHAMAX
            ALPHANEW = MAX(ALPHAINIT,ALPHANEWMELT)
      END IF

      END IF

            STATEV(1) = ALPHANEW
            STATEV(2) = ALPHANEW*ALPHAMAX

      RETURN
      END
```

Bibliography

[1] A Amado et al. "Characterization and modeling of non-isothermal crystallization of Polyamide 12 and co-Polypropylene during the SLS process". In: *5th International Polymers & Moulds Innovations Conference, Ghent*. 2012.

[2] M. Ambati, T. Gerasimov, and L. DeLorenzia. "A review on phase-field models of brittle fracture and a new fast hybrid formulation". In: *Computational Mechanics* 55 (2015), pp. 383–406.

[3] E.M. Arruda and M.C. Boyce. "A three-dimensional constitutive model for the large stretch behavior of rubber elastic materials". In: *Journal of the Mechanics and Physics of Solids* 41(2) (1993), pp. 389–412.

[4] Faisal As' ad, Philip Avery, and Charbel Farhat. "A mechanics-informed artificial neural network approach in data-driven constitutive modeling". In: *International Journal for Numerical Methods in Engineering* 123.12 (2022), pp. 2738–2759.

[5] Melvin Avrami. "Kinetics of phase change. I General theory". In: *The Journal of chemical physics* 7.12 (1939), pp. 1103–1112.

[6] Firas Awaja et al. "Cracks, microcracks and fracture in polymer structures: Formation, detection, autonomic repair". In: *Progress in Materials Science* 83 (2016), pp. 536–573.

[7] Deepak Behera, Pranesh Roy, and Erdogan Madenci. "Peridynamic correspondence model for finite elastic deformation and rupture in Neo-Hookean materials". In: *International Journal of Non-Linear Mechanics* 126 (2020), p. 103564.

[8] M. Behzadinasab and J.T. Foster. "A semi-Lagrangian constitutive correspondence framework for peridynamics". In: *Journal of the Mechanics and Physics of Solids* 137 (2020), p. 103862.

[9] Dana Bishara and Shaofan Li. "A machine-learning aided multiscale homogenization model for crystal plasticity: application for face-centered cubic single crystals". In: *Computational Mechanics* (2023), pp. 1–17.

[10] Dana Bishara and Shaofan Li. "A multiscale two-dimensional finite element incorporating the second-order Cauchy–Born rule for cohesive zone modeling: Simulation of fracture in polycrystalline materials". In: *Engineering Fracture Mechanics* 280 (2023), p. 109117.

[11] Bobet2000. "The initiation of secondary cracks in compression". In: *Engineering Fracture Mechanics* 66(2) (2000), pp. 187–219.

[12] M.C. Boyce and E.M. Arruda. "Constitutive models of rubber elasticity: a review". In: *Rubber chemistry and technology* 73(3) (2000), pp. 504–523.

[13] Mary C Boyce and Ellen M Arruda. "Constitutive models of rubber elasticity: a review". In: *Rubber chemistry and technology* 73.3 (2000), pp. 504–523.

[14] Nathaniel Brahms. *Fast interpolation*. [Online, MATLAB central file exchange; accessed January 15, 2023]. 2006.

[15] C.S. Brazel and S.L. Rosen. *Fundamental principles of polymeric materials*. John Wiley & Sons, 2012.

[16] Kimberly Chenoweth, Adri CT Van Duin, and William A Goddard. "ReaxFF reactive force field for molecular dynamics simulations of hydrocarbon oxidation". In: *The Journal of Physical Chemistry A* 112.5 (2008), pp. 1040–1053.

[17] François Chollet et al. *Keras*. ttps://keras.io. 2015.

[18] A Cohen. "A Padé approximant to the inverse Langevin function". In: *Rheologica acta* 30 (1991), pp. 270–273.

[19] Gianna Cojazzi et al. "The crystal structure of polylauryllactam (nylon 12)". In: *Die Makromolekulare Chemie: Macromolecular Chemistry and Physics* 168.1 (1973), pp. 289–301.

[20] Hüsnü Dal, Kemal Açıkgöz, and Yashar Badienia. "On the performance of isotropic hyperelastic constitutive models for rubber-like materials: A state of the art review". In: *Applied Mechanics Reviews* 73.2 (2021), p. 020802.

[21] Denis J Evans and Brad Lee Holian. "The nose–hoover thermostat". In: *The Journal of chemical physics* 83.8 (1985), pp. 4069–4074.

[22] Alan N Gent. "A new constitutive relation for rubber". In: *Rubber chemistry and technology* 69.1 (1996), pp. 59–61.

[23] A Greco and A Maffezzoli. "Polymer melting and polymer powder sintering by thermal analysis". In: *Journal of thermal analysis and calorimetry* 72.3 (2003), pp. 1167–1174.

[24] A Greco and A Maffezzoli. "Statistical and kinetic approaches for linear low-density polyethylene melting modeling". In: *Journal of applied polymer science* 89.2 (2003), pp. 289–295.

[25] A.L. Gurson. "Continuum theory of ductile rupture by void nucleation and growth: Part IYield criteria and flow rules for porous ductile media". In: *ASME, J. Eng. Materials and Technology* 99 (1977), pp. 2–15.

[26] Y.D. Ha and F. Bobaru. "Studies of dynamic crack propagation and crack branching with peridynamics". In: *International Journal of Fracture* 162(1-2) (2010), pp. 229–244.

[27] J. Han et al. "On nonlocal cohesive continuum mechanics and Cohesive Peridynamic Modeling (CPDM) of inelastic fracture". In: *Journal of the Mechanics and Physics of Solids* 164 (2022), p. 104894.

[28] R.J. Hardy. "Formulas for determining local properties in molecular-dynamics simulations: Shock waves". In: *The Journal of Chemical Physics* 76(1) (1982), pp. 622–628.

[29] Jana Herzberger et al. "Polymer design for 3D printing elastomers: recent advances in structure, properties, and printing". In: *Progress in Polymer Science* 97 (2019), p. 101144.

[30] N. A. Hocine, M. N. Abdelaziz, and A. Imad. "Fracture problems of rubbers: J-integral estimation based upon η factors and an investigation on the strain energy density distribution as a local criterion". In: *International Journal of Fracture* 117.1 (2002), pp. 1–23.

[31] John D Hoffman, G Thomas Davis, and John I Lauritzen. "The rate of crystallization of linear polymers with chain folding". In: *Treatise on solid state chemistry*. Springer, 1976, pp. 497–614.

[32] John D Hoffman and James J Weeks. "Melting process and the equilibrium melting temperature of polychlorotrifluoroethylene". In: *J. Res. Natl. Bur. Stand., Sect. A* 66.1 (1962), pp. 13–28.

[33] Cornelius O Horgan and Giuseppe Saccomandi. "Constitutive models for compressible nonlinearly elastic materials with limiting chain extensibility". In: *Journal of Elasticity* 77 (2004), pp. 123–138.

[34] Kurt Hornik. "Approximation capabilities of multilayer feedforward networks". In: *Neural networks* 4.2 (1991), pp. 251–257.

[35] Kurt Hornik, Maxwell Stinchcombe, and Halbert White. "Multilayer feedforward networks are universal approximators". In: *Neural networks* 2.5 (1989), pp. 359–366.

[36] Kazuo Inoue and Sadao Hoshino. "Crystal structure of nylon 12". In: *Journal of Polymer Science: Polymer Physics Edition* 11.6 (1973), pp. 1077–1089.

[37] J.H. Irving and J.G. Kirkwood. "The statistical mechanical theory of transport processes. IV. The equations of hydrodynamics". In: *The Journal of Chemical Physics* 18(6) (1950), pp. 817–829.

[38] M. Jamshidian et al. "Multiscale modelling of soft lattice metamaterials: Micromechanical nonlinear buckling analysis, experimental verification, and macroscale constitutive behaviour". In: *International Journal of Mechanical Sciences* 188 (2020), p. 105956.

[39] R. Jedynak. "A comprehensive study of the mathematical methods used to approximate the inverse Langevin function". In: *Mathematics and Mechanics of Solids* 24.7 (2019), pp. 1992–2016.

[40] G. S. Kedziora et al. “Ab initio molecular dynamics modeling of single polyethylene chains: Scission kinetics and influence of radical under mechanical strain”. In: *The Journal of Chemical Physics* 155.2 (2021), p. 024102.

[41] G. S. Kedziora et al. “Bond breaking in stretched molecules: multi-reference methods versus density functional theory”. In: *Theoretical Chemistry Accounts* 135.3 (2016), p. 79.

[42] Hossein Khorshidi et al. “Fresh, mechanical and microstructural properties of alkali-activated composites incorporating nanomaterials: A comprehensive review”. In: *Journal of Cleaner Production* (2022), p. 135390.

[43] J.K. Kim and R.E. Robertson. “Toughening of thermoset polymers by rigid crystalline particles”. In: *Journal of Materials Science* 27 (1992), pp. 161–174.

[44] Diederik P Kingma and Jimmy Ba. “Adam: A method for stochastic optimization”. In: *arXiv preprint arXiv:1412.6980* (2014).

[45] E. G. Kirsch. “Die Theorie der ElastizitÃ¤t und die BedÃ¼rfnisse der Festigkeitslehre”. In: *Zeitschrift des Vereines deutscher Ingenieure* 42 (1898), 797Â807.

[46] Malgorzata Kowalik et al. “Atomistic scale analysis of the carbonization process for C/H/O/N-based polymers with the ReaxFF reactive force field”. In: *The Journal of Physical Chemistry B* 123.25 (2019), pp. 5357–5367.

[47] Sanjay Krishna, I Sreedhar, and Chetan M Patel. “Molecular dynamics simulation of polyamide-based materials–A review”. In: *Computational Materials Science* 200 (2021), p. 110853.

[48] Xiao Kuang et al. “3D printing of highly stretchable, shape-memory, and self-healing elastomer toward novel 4D printing”. In: *ACS applied materials & interfaces* 10.8 (2018), pp. 7381–7388.

[49] W. Kuhn and F. Grün. “Statistical behavior of the single chain molecule and its relation to the statistical behavior of assemblies consisting of many chain molecules”. In: *Journal of polymer science* 1(3) (1946), pp. 183–199.

[50] Y. LeCun et al. “Efficient backprop”. In: *Neural networks: Tricks of the trade*. Springer, 2002, pp. 9–50.

[51] R.B. Lehoucq and A. Von Lilienfeld-Toal. “Translation of Walter Noll’s Derivation of the fundamental equations of continuum thermodynamics from statistical mechanicsÃ¢ÂÂ”. In: *Journal of Elasticity* 100(1-2) (2010), pp. 5–24.

[52] R.B. Lehoucq and S.A. Silling. “Force flux and the peridynamic stress tensor”. In: *Journal of the Mechanics and Physics of Solids* 56(4) (2008), pp. 1566–1577.

[53] Alexander LeNail. “NN-SVG: Publication-Ready Neural Network Architecture Schematics.” In: *J. Open Source Softw.* 4.33 (2019), p. 747.

[54] C.Y. Li, Z.Y. Xia, and H.J. Sue. "Simple shear plastic deformation behavior of polycarbonate plate II. Mechanical property characterization". In: *Polymer* 41(16) (2000), pp. 6285–6293.

[55] J. Li et al. "Peridynamic stress is the static first Piola-Kirchhoff Virial stress". In: *International Journal of Solids and Structures* 241 (2022), p. 111478.

[56] L. Li et al. "Hyperband: A novel bandit-based approach to hyperparameter optimization". In: *The Journal of Machine Learning Research* 18.1 (2017), pp. 6765–6816.

[57] D. López Barreiro et al. "Multiscale Modeling of Silk and Silk-Based Biomaterials A Review". In: *Macromolecular bioscience* 19(3) (2019), p. 1800253.

[58] E. Madenci and E. Oterkus. *Peridynamic theory and its applications*. New York: Springer, 2014.

[59] Y. Mao and L. Anand. "A theory for fracture of polymeric gels". In: *Journal of the Mechanics and Physics of Solids* 115 (2018), pp. 30–53.

[60] Y. Mao and L. Anand. "Fracture of elastomeric materials by crosslink failure". In: *Journal of Applied Mechanics* 85(8) (2018).

[61] Y. Mao, B. Talamini, and L. Anand. "Rupture of polymers by chain scission". In: *Extreme Mechanics Letters* 13 (2017), pp. 17–24.

[62] Martín Abadi et al. *TensorFlow: Large-Scale Machine Learning on Heterogeneous Systems*. Software available from tensorflow.org. 2015. URL: `https://www.tensorflow.org/`.

[63] Lon J Mathias and C Greg Johnson. "Solid-state NMR investigation of nylon 12". In: *Macromolecules* 24.23 (1991), pp. 6114–6122.

[64] Thomas R Mattsson et al. "First-principles and classical molecular dynamics simulation of shocked polymers". In: *Physical Review B* 81.5 (2010), p. 054103.

[65] G.H. Michler and W. Lebek. "Electron microscopy of polymers". In: *Polymer Morphology: Principles, Characterization, and Processing*. 2016, pp. 37–53.

[66] Melvin Mooney. "A theory of large elastic deformation". In: *Journal of applied physics* 11.9 (1940), pp. 582–592.

[67] A.I. Murdoch. "The motivation of continuum concepts and relations from discrete considerations". In: *The Quarterly Journal of Mechanics and Applied Mathematics* 36(2) (1983), pp. 163–187.

[68] A.I. Murdoch and D. Bedeaux. "Continuum equations of balance via weighted averages of microscopic quantities". In: *Proceedings of the Royal Society of London. Series A: Mathematical and Physical Sciences* 445(1923) (1994), pp. 157–179.

[69] K Nakamura, K Katayama, and T Amano. "Some aspects of nonisothermal crystallization of polymers. II. Consideration of the isokinetic condition". In: *Journal of Applied Polymer Science* 17.4 (1973), pp. 1031–1041.

[70] K Nakamura et al. "Some aspects of nonisothermal crystallization of polymers. I. Relationship between crystallization temperature, crystallinity, and cooling conditions". In: *Journal of Applied Polymer Science* 16.5 (1972), pp. 1077–1091.

[71] S. Narayan and L. Anand. "Fracture of amorphous polymers: A gradient-damage theory". In: *Journal of the Mechanics and Physics of Solids* 146 (2021), p. 104164.

[72] W. Noll. "Die Herleitung der Grundgleichungen der Thermomechanik der Kontinua aus der statistischen Mechanik". In: *Journal of Rational Mechanics and Analysis* 4 (1955), pp. 627–646.

[73] T. O'Malley et al. *KerasTuner*. 2019.

[74] Raymond William Ogden. "Large deformation isotropic elasticity–on the correlation of theory and experiment for incompressible rubberlike solids". In: *Proceedings of the Royal Society of London. A. Mathematical and Physical Sciences* 326.1567 (1972), pp. 565–584.

[75] T Ozawa. "Kinetics of non-isothermal crystallization". In: *Polymer* 12.3 (1971), pp. 150–158.

[76] Luís Antonio Pinheiro, Marcelo Aparecido Chinelatto, and Sebastião Vicente Canevarolo. "The role of chain scission and chain branching in high density polyethylene during thermo-mechanical degradation". In: *Polymer Degradation and Stability* 86.3 (2004), pp. 445–453.

[77] Ronald S Rivlin. "Large elastic deformations of isotropic materials IV. Further developments of the general theory". In: *Philosophical transactions of the royal society of London. Series A, Mathematical and physical sciences* 241.835 (1948), pp. 379–397.

[78] Pranesh Roy, Deepak Behera, and Erdogan Madenci. "Peridynamic simulation of finite elastic deformation and rupture in polymers". In: *Engineering Fracture Mechanics* 236 (2020), p. 107226.

[79] Wissam A Saidi. "Emergence of local scaling relations in adsorption energies on high-entropy alloys". In: *npj Computational Materials* 8.1 (2022), p. 86.

[80] Wissam A Saidi, Waseem Shadid, and Ivano E Castelli. "Machine-learning structural and electronic properties of metal halide perovskites using a hierarchical convolutional neural network". In: *npj Computational Materials* 6.1 (2020), p. 36.

[81] J.C. Salamone. *Polymeric materials encyclopedia*. CRC press, 2020.

[82] T.P. Senftle et al. "The ReaxFF reactive force-field: development, applications and future directions". In: *npj Computational Materials* 2.1 (2016), pp. 1–14.

[83] S. Sharafi et al. "A multiscale modeling approach of the Fused Filament Fabrication process to predict the mechanical response of 3D printed parts". In: *Additive Manufacturing* 51 (2022), p. 102597.

[84] S.A. Silling. "Reformulation of elasticity theory for discontinuities and long-range forces". In: *Journal of the Mechanics and Physics of Solids* 48 (2000), pp. 175–209.

[85] S.A. Silling and R.B. Lehoucq. "Peridynamic theory of solid mechanics". In: *Advances in Applied Mechanics* 44 (2010), pp. 73–168.

[86] S.A. Silling et al. "Peridynamic states and constitutive modeling". In: *Journal of Elasticity* 88 (2007), pp. 151–184.

[87] J. Sola and J. Sevilla. "Importance of input data normalization for the application of neural networks to complex industrial problems". In: *IEEE Transactions on nuclear science* 44.3 (1997), pp. 1464–1468.

[88] Arun K Subramaniyan and CT Sun. "Continuum interpretation of virial stress in molecular simulations". In: *International Journal of Solids and Structures* 45.14-15 (2008), pp. 4340–4346.

[89] B. Talamini, Y. Mao, and L. Anand. "Progressive damage and rupture in polymers". In: *Journal of the Mechanics and Physics of Solids* 111 (2018), pp. 434–457.

[90] Caglar Tamur and Shaofan Li. "A bond-based peridynamics modeling of polymeric material fracture under finite deformation". In: *Computer Methods in Applied Mechanics and Engineering* 414 (2023), p. 116132.

[91] Caglar Tamur, Shaofan Li, and Danielle Zeng. "Artificial Neural Networks for Predicting Mechanical Properties of Crystalline Polyamide12 via Molecular Dynamics Simulations". In: *Polymers* 15.21 (2023), p. 4254.

[92] Aidan P Thompson et al. "LAMMPS-a flexible simulation tool for particle-based materials modeling at the atomic, meso, and continuum scales". In: *Computer Physics Communications* 271 (2022), p. 108171.

[93] LR G Treloar. "The physics of rubber elasticity". In: (1975).

[94] LRG Treloar. "The elasticity of a network of long-chain molecules—II". In: *Transactions of the Faraday Society* 39 (1943), pp. 241–246.

[95] LRG Treloar. "The elasticity of a network of long-chain molecules.—III". In: *Transactions of the Faraday Society* 42 (1946), pp. 83–94.

[96] P. Underwood. "Dynamic relaxation". In: *Computational method for transient analysis* 1 (1986), pp. 245–263.

[97] S. Urata and S. Li. "Higher order Cauchy-Born rule based multiscale cohesive zone model and prediction of fracture toughness of Silicon thin films". In: *International Journal of Fracture* 203(1) (2017), pp. 159–181.

[98] Adri CT Van Duin et al. "ReaxFF: a reactive force field for hydrocarbons". In: *The Journal of Physical Chemistry A* 105.41 (2001), pp. 9396–9409.

[99] Jun Wang et al. "Evolution of crystallographic orientation, precipitation, phase transformation and mechanical properties realized by enhancing deposition current for dual-wire arc additive manufactured Ni-rich NiTi alloy". In: *Additive Manufacturing* 34 (2020), p. 101240.

[100] Ming Chen Wang and Eugene Guth. "Statistical theory of networks of non-Gaussian flexible chains". In: *The Journal of Chemical Physics* 20.7 (1952), pp. 1144–1157.

[101] Yi Wang et al. "Friction behavior of biodegradable electrospun polyester nanofibrous membranes". In: *Tribology International* 188 (2023), p. 108891.

[102] Yuanhang Xu et al. "Unraveling of advances in 3D-printed polymer-based bone scaffolds". In: *Polymers* 14.3 (2022), p. 566.

[103] J.Z. Yang, X. Wu, and X. Li. "A generalized IrvingKirkwood formula for the calculation of stress in molecular dynamics models". In: *The Journal of chemical physics* 137(13) (2012), p. 134104.

[104] Quanpeng Yang et al. "Molecular Dynamics Simulation of the Stress–Strain Behavior of Polyamide Crystals". In: *Macromolecules* 54.18 (2021), pp. 8289–8302.

[105] Dundar E Yilmaz and Adri CT van Duin. "Investigating structure property relations of poly (p-phenylene terephthalamide) fibers via reactive molecular dynamics simulations". In: *Polymer* 154 (2018), pp. 172–181.

[106] H. Yu and S. Li. "On energy release rates in Peridynamics". In: *Journal of the Mechanics and Physics of Solids* 142 (2020), p. 104024.

[107] Weiwei Zhang and Adri CT Van Duin. "Improvement of the ReaxFF description for functionalized hydrocarbon/water weak interactions in the condensed phase". In: *The Journal of Physical Chemistry B* 122.14 (2018), pp. 4083–4092.

[108] Meng Zhao, Katrin Wudy, and Dietmar Drummer. "Crystallization kinetics of polyamide 12 during selective laser sintering". In: *Polymers* 10.2 (2018), p. 168.

[109] Yuhong Zhao et al. "Dislocation motion in plastic deformation of nano polycrystalline metal materials: a phase field crystal method study". In: *Advanced Composites and Hybrid Materials* 5.3 (2022), pp. 2546–2556.

[110] J.A. Zimmerman et al. "Calculation of stress in atomistic simulation". In: *Modelling and Simulation in Materials Science and Engineering* 12(4) (2004), S319.